THE UNIVERSITY OF CHICAGO

DIRECTED ASSEMBLY OF FUNCTIONAL NANOMATERIALS USING CHEMICAL PATTERNS

A DISSERTATION SUBMITTED TO
THE FACULTY OF THE PRITZKER SCHOOL OF MOLECULAR ENGINEERING
IN CANDIDACY FOR THE DEGREE OF
DOCTOR OF PHILOSOPHY

BY
JIAJING LI

CHICAGO, ILLINOIS
DECEMBER 2019

CONTENTS

List of Tables

List of Figures

Acknowledgements

I have been blessed with so much more than I deserve during the past five years, and I wouldn't have made it without all the supports and encouragements from the best mentors, collaborators and friends.

I would like to express my sincere gratitude to my advisor, Professor Paul F. Nealey, for giving me the wonderful opportunity to join the Nealey group, where I could learn and grow with brilliant peers in a positive and encouraging environment. With Prof. Nealey's guidance and encouragements, I not only gained more confidence as a researcher, but also grew more mature and capable as an individual. During my graduate studies, not even a second have I doubted the choice I made five years ago.

I would also like to give special thanks to Dr. Xiaoying Liu and Dr. Paulina A. Rincon-Delgadillo for being amazing mentors at different stage of my studies. Xiaoying taught me how to think scientifically when I first joined the group, and Paulina offered me very interesting projects to work on when I visited imec. They are both excellent women working in science and will continue to be my role models. Also, many thanks to other members in the group for their great help: Chun Zhou, Dr. Hongbo Feng and Xuanxuan Chen helped me with the experiments; Dr. Hyo Seon Suh helped me with the training at imec as well as helpful discussions on the projects; Dr. James A. Dolan helped me with the writing and discussion; Dr. Xiao Li always brought me delicious cakes. I'm also very grateful to other group members for their personal help and friendship.

My collaborators give me the wonderful opportunities to work in interdisciplinary fields and to learn beyond my own field. Paolo Andrich from Prof. David Awschalom's group taught me about quantum sensing; Dr. Tian-song Deng from Prof. Norbert F. Scherer's group helped me

understand optics and photonics; Dr. Vikram Thapar and Prof. Su-mi Hur shared me their expertise in computational models. Their intelligence and diligence constantly inspired me during my graduate studies and were critical to the success of our projects.

I would like to extend my appreciation to all of my friends. Many thanks to my friends in Chicago and Belgium who shared time with me. Special thanks to Tianhui for always being there for me. The encounter with Satomi in Belgium was most unexpected but wonderful. I am grateful to everyone who has been part of my life during the past 5 years even though it would be impossible to name you all.

Finally, I am greatly indebted to my parents Shuqiang Li (李树强) and Zihua Qi (齐滋华). They strived to offer me a warm and loving home where I could grow up happy and free. As a child I had always taken it for granted, but only recently did I realize how difficult it was and how lucky I was. It'll be my turn to take care of you, and I wish I could do as well.

Abstract

Nanomaterials have generated intense interest due to their novel properties which open up numerous opportunities in fundamental and applied nanophotonics, nanoelectronics, and nanomagnetics. However, these materials are generally processed in the solution phase, and a reliable way to transfer them from solution to surface with full addressability remains elusive, thereby limiting the technological usefulness of such materials. To address this issue, we propose to control the assembly of nanomaterials on surface using chemical pattern, which is a lithographically defined pattern with chemical contract. The patterned areas and unpatterned areas are functionalized with different surface chemistry, creating the necessary chemical contrast to selectively immobilize the nanomaterials on specific areas. Depending on different types of materials, a wide range of functions and applications can be realized using this chemical pattern technique.

In this thesis, we demonstrate the possibility of combing chemical pattern with three different materials – block copolymer, gold nanoparticle and nanodiamond. The first chapter introduces basic concept of chemical pattern and its advantages, followed by Chapter 2 focusing on directed self-assembly (DSA) of block copolymers (BCPs) for lithography applications. We demonstrate line/space pattern with sub-10 nm half pitch with a polymeric additive added to the BCP. Chapter 3 and 4 investigate kinetics of defect annihilation in DSA in the hope of further reducing the defect density. Physical models have been developed to describe the annihilation kinetics through extensive statistical analysis and image processing. Chapter 5 demonstrates a hierarchical assembly approach of gold nanoparticle heterodimers combining chemical pattern and DNA directed assembly. The gap size of assembled heterodimers is in the sub-5 nm regime with sub-nm variance, making them excellent candidate for surface enhanced Raman scattering (SERS)

substrate. Finally, we briefly introduce a flexible platform of patterned nanodiamonds for microscale-resolution thermal mapping in Chapter 6. The temperature sensing capacity of this platform has been confirmed with simulation results. The chemical pattern technique is expected to hold a lot more potentials in many other material systems for further applications.

Chapter 1: Introduction

1.1 Nanomaterials and chemical pattern

Nanomaterials are materials with any external or internal structures on the nanoscale dimension, typically between 1 to 1000 nm.[1] The history of utilizing nanomaterials can be traced back to 4500 years ago, when humans employed natural asbestos nanofibers to reinforce ceramic matrixes.[2] However the understanding of nanomaterials has been very limited due to lack of characterization methods until electron microscopy was invented in the last century, enabling unprecedented speed in the development of nanotechnology. Researchers are able to precisely control the composites and structures of materials on the nanoscale to fully employ their unique properties. Common nanomaterials include carbon-based nanomaterials, inorganic-based nanomaterials, organic-based nanomaterials and composite based nanomaterials. In this thesis, we will mainly focus on inorganic-based and organic-based nanomaterials.

Nanomaterials have attracted intense interest from both academia and industry due to their unique properties, mainly attributed to quantum effects, large surface area and self-assembly.[3] These properties have enabled various applications of nanomaterials in electronics,[4,5] biomedical,[6–8] energy and environmental applications.[9–11] These materials, however, are usually synthesized in the solution phase, and it remains an outstanding challenge to transfer them from solution phase to substrate surface with precise spatial control, which can be crucial to certain applications like nanophotonics and nanoelectronics.

To address this issue, we propose to use chemical pattern to direct the assembly of functional nanomaterials on surface. Chemical pattern is a lithographically defined pattern with a chemical contrast—the patterned areas and unpatterned areas are functionalized with different

surface chemistry, creating the necessary contrast to selectively immobilize nanomaterials on the specific areas. Chemical pattern can be defined by various lithography methods such as photolithography,[12] electron-beam lithography,[13] extreme ultraviolet interference lithography[14] and nanoimprint.[15] In order to create the chemical contrast between patterned and unpatterned areas, either area can be treated with plasma[16], monolayer functionalization[17] or polymer brush grafting.[18] The nanomaterials interact with the chemical pattern to order into the desired structures and to reach thermodynamic equilibrium.

1.2 Block copolymer and directed self-assembly

Directed self-assembly (DSA) of block copolymers (BCPs) is one of the major examples of the usefulness of chemical patterns. Block copolymers are polymer chains composed of two or more blocks that are covalently bonded. Since interactions between same blocks are more favorable than interactions between different blocks, block copolymers can phase separate into different structures to reach thermodynamic equilibrium. Take diblock copolymer as an example, it can self-assemble into various structures such as sphere, cylinder, gyroid and lamella, which is governed by the relative size of the two blocks and Flory-Huggins parameter (χ) (Figure 1.1).[19] Flory-Huggins parameter describes the excess free energy when mixing the two blocks, and a higher χ indicates greater dissimilarities between the two blocks. After BCP self-assembly, one block of BCPs can be selectively removed, leaving the template useful for various applications such as fabrication of nanowires and photonic crystals.[20,21] However the performance of such devices can be impaired due to lack of long-range ordering of the templates.

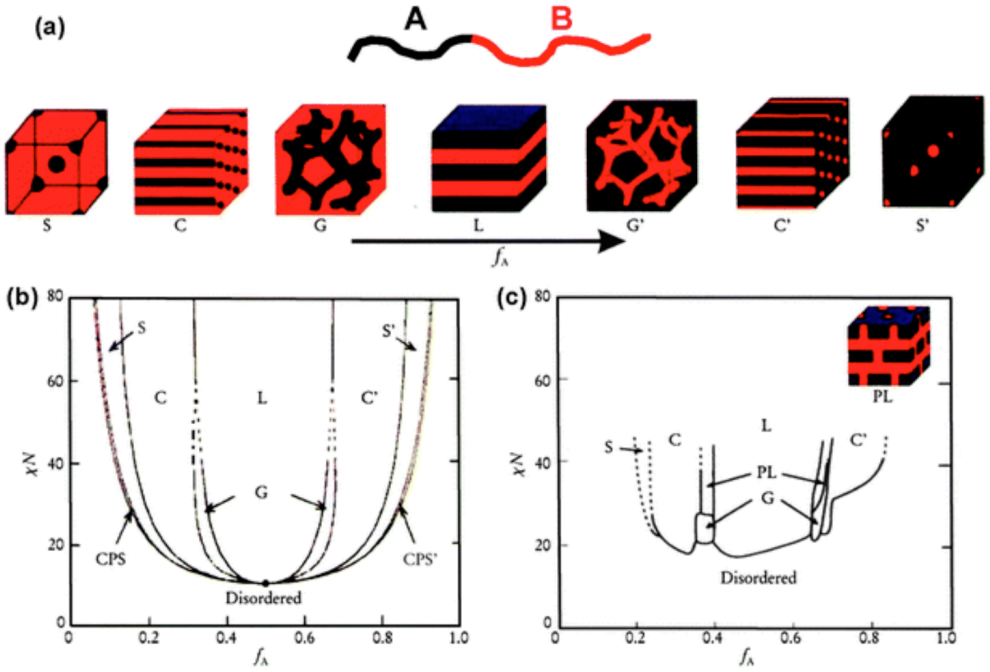

Figure 1.1 (a) Equilibrium morphologies of AB diblock copolymers in bulk: S and S′ = body-centered-cubic spheres, C and C′ = hexagonally packed cylinders, G and G′ = bicontinuous gyroids, and L = lamellae. (b) Theoretical phase diagram of AB diblocks predicted by the self-consistent mean-field theory, depending on volume fraction (*f*) of the blocks and the segregation parameter, χN, where χ is the Flory–Huggins segment–segment interaction energy and *N* is the degree of polymerization; CPS and CPS′ = closely packed spheres.6 (c) Experimental phase portrait of polyisoprene-*block*-polystyrene copolymers, in which f_A represents the volume fraction of polyisoprene, PL = perforated lamellae. Reprinted with permission from Mai, *et al.*[22] Copyright (2012) Royal Society of Chemistry.

In order to achieve perfect periodic domain ordering on a macroscopic scale, chemoepitaxy DSA has been developed to control the registration of BCP domains with respect to the substrate.[23] Chemoepitaxy DSA utilizes chemical patterns to order the self-assembling BCPs into periodic nanostructures such as line/space and contact holes, which resemble critical features in integrated circuits. It has been shown that DSA can readily multiply the lithographical features of the chemical pattern and increase the pattern resolution severalfold,[13] which gives it the unique advantage over many other multiple patterning techniques in terms of process simplicity and cost effectiveness. Figure 1.2 shows a typical scheme of chemo-epitaxy DSA with density

multiplication. After lithography, etching and brush grafting, chemical pattern composed of guiding stripes and interspatial neutral brush is ready to be used for DSA. Guiding stripes selectively wet one block of the BCP, whereas the neutral brush is almost non-preferential to both blocks, providing the boundary condition for BCP to align along the guiding stripes. Chemoepitaxy DSA holds the advantage of fabricating high-density periodic patterns with sub-lithographic feature size at very low cost,[13] and thus has attracted great interest from the lithography community.

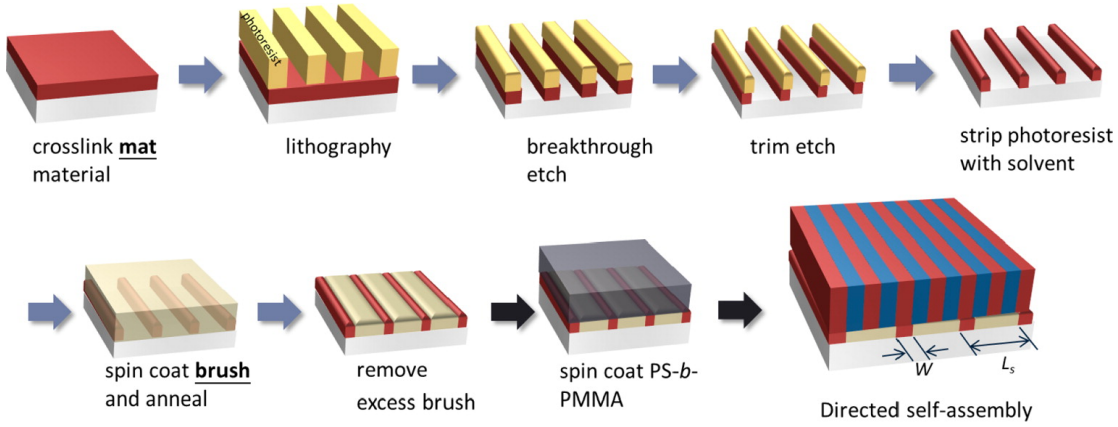

Figure 1.2 Schematic of the fabrication process of the chemically patterned substrates and the directed assembly of PS-b-PMMA with density multiplication. Reprinted with permission from Liu, *et al*.[14] Copyright (2013) American Chemical Society.

1.3 Defectivity in directed self-assembly

Despite the great interest DSA has attracted, it is not widely adopted in high volume manufacturing (HVM) primarily due to the defectivity issue. Common academic laboratories mainly use scanning electron microscope (SEM) and atomic force microscope (AFM) to characterize the quality of DSA, which can only inspect limited areas and are not sufficient for defectivity study. HVM typically requires less than 1 defect per 100 cm^2, which will take thousands of SEM images to find one single defect at such low density. As a result, experimental study of defectivity in DSA has been limited, and it only became possible a few years ago when DSA was implemented on the 300 mm wafer processing line at IMEC.[24]

Defectivity in DSA, for the first time, has been fully quantified using the state-of-the-art defect inspections tools in 300 mm wafer fab. Various processing parameters have been optimized to reduce the defect density such as pattern pitch, guiding stripe width, template topography, background chemistry and annealing conditions.[12,25,26] Any deviation from optimized conditions will cause slower annihilation kinetics and higher defect density. Through these extensive efforts, defect density has been reduced by several orders of magnitude, approaching that required by HVM.

However, it is still challenging to achieve prefect defect-free assembly, which is among one of the most pressing issues for DSA. Simulation studies have predicted that defects have much higher free energies than defect-free structures, and are highly energetically unfavorable,[27,28] which seems to create a paradox that defects can still be observed even after long annealing. In fact, this seeming conflict can be well explained by kinetics of defect annihilation, rather than thermodynamics. Hur, *et al.* has identified the minimum free energy paths between defective and ordered states, where multiple energy barriers have been observed along the free energy pathway.[29,30] Even though defects are energetically unfavorable, they can be kinetically trapped by these energy barriers and persist throughout the annealing. Consequently, kinetic study is required to understand the mechanism of defect formation and annihilation in DSA, which will be the focus in Chapter 3 and 4.

1.4 Directed assembly of nanoparticles

In addition to BCPs, chemical pattern can be incredibility useful for site specific placement of nanoparticle (NP) assemblies in combination with other techniques such as DNA directed assembly. The ability to exploit the properties of NP assemblies depends on both morphological control and spatial arrangement of NPs. Morphological control is usually mediated by

thermodynamic interactions between individual building blocks, and spatial arrangement relies largely on the interactions between NPs and surface. Conventional fabrication approaches depend on only one or the other of these two interactions. Single crystal NPs assembled in solution have tailored size, shape and composition, allowing for well controlled properties of these structures.[31,32] However it remains an outstanding challenge to transfer these solution-processed assemblies to the designated locations on surface, limiting their technological usefulness. On the other hand, lithographically-defined patterns have been used to assemble NPs in combination with topographical contrast, chemical contrast and DNA origami, enabling site specific placement of functional nanostructures.[34–36] But the control over uniformity and reproducibility is usually limited in these cases, which can impair their properties and applications. An assembly approach that can enable both morphological control and precise spatial arrangement will tackle this challenge and represent a considerate advance in nanofabrication. Chapter 5 demonstrates a hierarchical assembly approach employing both interparticle interaction and template-particle interaction, where the former offers tunable structural control and the latter provides precise addressability on surface.

Though the chemical pattern approach is applicable to a variety of substrates, the assembled structures can further be transferred to other platforms and enable even more applications. Chapter 6 shows that the nanodiamond assemblies on chemical pattern can be transferred to a flexible polymer matrix via transfer printing technique,[36] which can be used for microscale thermal mapping and temperature monitoring of various systems.

1.5 Outline

The goal of this work is to demonstrate the technological usefulness of chemical pattern in nanofabrication and to thoroughly investigate the associated properties in each system. The thesis

starts with DSA, one of the most well-known applications of chemical pattern, followed by site specific placement of gold nanoparticles and nanodiamonds for sensing applications.

Chapter 2 proposes to control the orientation of high-χ BCPs using a polymeric additive. By tuning the additive dose and annealing conditions, desired perpendicular orientation can be achieved with simple thermal annealing. DSA has been successfully demonstrated with a full pitch as small as 17 nm, and the pattern transfer ability has been investigated. Furthermore, a simple yet effective way has been proposed to predict the molecular weight of additive needed for a given BCP in order to achieve optimized orientation control.

Chapter 3 and 4 investigate the kinetics of defectivity in DSA. Chapter 3 discusses the overall kinetics of dislocations and bridges, and kinetic models have been developed for each defect type. The impacts of annealing temperature and film thickness have been discussed, providing potential paths to further defect reduction. The defect density has been reduced by 1 order of magnitude simply by optimizing annealing conditions and film thickness. Chapter 4 provides a comprehensive study of dislocations, and thoroughly investigates the distribution of dislocation spacings and configurations. Through extensive statistical analysis, the probability of observing a certain dislocation edge has been revealed, providing valuable information about the mechanism of dislocation formation and annihilation.

Chapter 5 demonstrates a hierarchical assembly approach of gold NPs combining chemical pattern and DNA directed assembly. Chemical pattern provides template-particle interaction, ensuring precise spatial arrangement of NPs on surface. DNA directed assembly provides interparticle interaction, enabling tunable and controllable interparticle spacing in the sub-5 nm regime. The sub-nm variance of the gap size has been confirmed by far-field light scattering and finite-difference time-domain (FDTD) simulations.

Chapter 6 develops a flexible platform of patterned quantum sensors for microscale thermal mapping. Arrays of quantum sensors have first been constructed on chemical patterns, followed by transferring to a polymer matrix via transfer printing. To demonstrate the thermal mapping potential of this platform, temperature profile of an operating coplanar waveguide has been experimentally reconstructed and compared with simulation result, confirming the accuracy of this platform.

1.6 References

(1) Jeevanandam, J.; Barhoum, A.; Chan, Y. S.; Dufresne, A.; Danquah, M. K. *Beilstein J. Nanotechnol.* **2018**, *9*, 1050–1074.

(2) Heiligtag, F. J.; Niederberger, M. *Mater. Today* **2013**, *16* (7–8), 262–271.

(3) Kumar, N.; Kumbhat, S. *Essentials in Nanoscience and Nanotechnology*; Wiley, **2016.**

(4) Choi, S.; Lee, H.; Ghaffari, R.; Hyeon, T.; Kim, D.-H. *Adv. Mater.* **2016**, *28* (22), 4203–4218.

(5) Wu, W. *Nanoscale* **2017**, *9* (22), 7342–7372.

(6) Jayakumar, R.; Menon, D.; Manzoor, K.; Nair, S. V.; Tamura, H. *Carbohydr. Polym.* **2010**, *82* (2), 227–232.

(7) West, J. L.; Halas, N. J. *Annu. Rev. Biomed. Eng.* **2003**, *5* (1), 285-292.

(8) Chen, A.; Chatterjee, S. *Chem. Soc. Rev.* **2013**, *42* (12), 5425.

(9) Li, Y.; Somorjai, G. A. *Nano Lett.* **2010**, *10* (7), 2289–2295.

(10) Xu, P.; Zeng, G. M.; Huang, D. L.; Feng, C. L.; Hu, S.; Zhao, M. H.; Lai, C.; Wei, Z.; Huang, C.; Xie, G. X.; Liu, Z. F. *Sci. Total Environ.* **2012**, *424*, 1–10.

(11) Zhang, Q.; Uchaker, E.; Candelaria, S. L.; Cao, G. *Chem. Soc. Rev.* **2013**, *42* (7), 3127.

(12) Williamson, L. D.; Seidel, R. N.; Chen, X.; Suh, H. S.; Rincon Delgadillo, P.; Gronheid, R.; Nealey, P. F. *ACS Appl. Mater. Interfaces* **2016**, *8* (4), 2704–2712.

(13) Ruiz, R.; Kang, H.; Detcheverry, F. A.; Dobisz, E.; Kercher, D. S.; Albrecht, T. R.; de Pablo, J. J.; Nealey, P. F. *Science* **2008**, *321* (5891), 936–939.

(14) Liu, C. C.; Ramírez-Hernández, A.; Han, E.; Craig, G. S. W.; Tada, Y.; Yoshida, H.; Kang,

H.; Ji, S.; Gopalan, P.; De Pablo, J. J.; Nealey, P. F. *Macromolecules* **2013**, *46* (4), 1415–1424.

(15) Maury, P.; Escalante, M.; Reinhoudt, D. N.; Huskens, J. *Adv. Mater.* **2005**, *17* (22), 2718–2723.

(16) Edwards, E. W.; Montague, M. F.; Solak, H. H.; Hawker, C. J.; Nealey, P. F. *Adv. Mater.* **2004**, *16* (15), 1315–1319.

(17) Hoeppener, S.; Maoz, R.; Cohen, S. R.; Chi, L. F.; Fuchs, H.; Sagiv, J. *Adv. Mater.* **2002**, *14* (15), 1036.

(18) Onses, M. S.; Thode, C. J.; Liu, C. C.; Ji, S.; Cook, P. L.; Himpsel, F. J.; Nealey, P. F. *Adv. Funct. Mater.* **2011**, *21* (16), 3074–3082.

(19) Bates, F. S.; Fredrickson, G. H. *Phys. Today* **1999**, *52* (2), 32–38.

(20) Thurn-Albrecht, T.; Schotter, J.; Kastle, G. A.; Emley, N.; Shibauchi, T.; Krusin-Elbaum, L.; Guarini, K.; Black, C. T.; Tuominen, M. T.; Russell, T. P. *Science* **2000**, *290* (5499), 2126–2129.

(21) Urbas, A.; Sharp, R.; Fink, Y.; Thomas, E. L.; Xenidou, M.; Fetters, L. J. *Adv. Mater.* **2000**, *12* (11), 812–814.

(22) Mai, Y.; Eisenberg, A. *Chem. Soc. Rev.* **2012**, *41* (18), 5969.

(23) Kim, S. O.; Solak, H. H.; Stoykovich, M. P.; Ferrier, N. J.; De Pablo, J. J.; Nealey, P. F. *Nature* **2003**, *424* (6947), 411–414.

(24) Delgadillo, P. A. R.; Gronheid, R.; Thode, C. J.; Wu, H.; Cao, Y.; Neisser, M.; Somervell, M.; Nafus, K.; Nealey, P. F. *J. Micro/Nanolithography, MEMS, MOEMS* **2012**, *11* (3), 031302.

(25) Garner, G. P.; Rincon Delgadillo, P.; Gronheid, R.; Nealey, P. F.; De Pablo, J. J. *Mol. Syst. Des. Eng.* **2017**, *2* (5), 567–580.

(26) Pathangi, H.; Chan, B. T.; Bayana, H.; Vandenbroeck, N.; Heuvel, D. Van Den; Look, L. Van; Rincon-Delgadillo, P.; Cao, Y.; Kim, J.; Lin, G.; Parnell, D.; Nafus, K.; Harukawa, R.; Chikashi, I.; Polli, M.; D'Urzo, L.; Gronheid, R.; Nealey, P. *J. Micro/Nanolithography, MEMS, MOEMS* **2015**, *14* (3), 031204.

(27) Nagpal, U.; Müller, M.; Nealey, P. F.; De Pablo, J. J.; Mu, M.; Nealey, P. F.; Pablo, J. J. De. *ACS Macro Lett.* **2012**, *1* (3), 418–422.

(28) Takahashi, H.; Laachi, N.; Delaney, K. T.; Hur, S.-M.; Weinheimer, C. J.; Shykind, D.; Fredrickson, G. H. *Macromolecules* **2012**, *45* (15), 6253–6265.

(29) Hur, S.-M.; Thapar, V.; Ramírez-Hernández, A.; Khaira, G.; Segal-Peretz, T.; Rincon-Delgadillo, P. A.; Li, W.; Müller, M.; Nealey, P. F.; de Pablo, J. J. *Proc. Natl. Acad. Sci.* **2015**, *112* (46), 14144–14149.

(30) Hur, S.-M.; Thapar, V.; Ramírez-Hernández, A.; Nealey, P. F.; de Pablo, J. J. *ACS Nano* **2018**, *12* (10), 9974–9981.

(31) Rogers, W. B.; Shih, W. M.; Manoharan, V. N. *Nat. Rev. Mater.* **2016**, *1* (3), 16008.

(32) Walther, A.; Müller, A. H. E. *Chem. Rev.* **2013**, *113* (7), 5194–5261.

(33) Liu, X.; Biswas, S.; Jarrett, J. W.; Poutrina, E.; Urbas, A.; Knappenberger, K. L.; Vaia, R. A.; Nealey, P. F. *Adv. Mater.* **2015**, *27* (45), 7314–7319.

(34) Flauraud, V.; Mastrangeli, M.; Bernasconi, G. D.; Butet, J.; Alexander, D. T. L. L.; Shahrabi, E.; Martin, O. J. F. F.; Brugger, J. *Nat. Nanotechnol.* **2017**, *12* (1), 73–80.

(35) Hung, A. M.; Micheel, C. M.; Bozano, L. D.; Osterbur, L. W.; Wallraff, G. M.; Cha, J. N. *Nat. Nanotechnol.* **2010**, *5* (2), 121–126.

(36) Andrich, P.; de las Casas, C. F.; Liu, X.; Bretscher, H. L.; Berman, J. R.; Heremans, F. J.; Nealey, P. F.; Awschalom, D. D. *npj Quantum Inf.* **2017**, *3* (1), 28.

Chapter 2: Orientation Control of High-χ Triblock Copolymer for Sub-10 nm Patterning Using Fluorine-Containing Polymeric Additives

* This chapter has been published in Journal of Micro/Nanolithography, MEMS, and MOEMS ("Orientation Control of High-χ Triblock Copolymer for Sub-10 nm Patterning Using Fluorine-Containing Polymeric Additives", Li, J.; Zhou, C.; Chen, X.; Rincon Delgadillo, P. A.; Nealey, P. F. *J. Micro/Nanolithography, MEMS, MOEMS* **2019**, *18* (03), 035501) and Proceedings of SPIE ("Directed Self-Assembly of Triblock Copolymers for Sub-10 nm Nanofabrication Using Polymeric Additives", Li, J.; Zhou, C.; Chen, X.; Rincon-Delgadillo, P. A.; Nealey, P. F. *Proc. SPIE* **2018**, *10586*, 105860V).[1,2]

2.1 Abstract

Directed self-assembly (DSA) of block copolymers (BCPs) is one of the most promising techniques to tackle the ever-increasing demand for sub-lithographic features in semiconductor industries. BCPs with high Flory Huggins parameter (χ) are of particular interest due to their ability to self-assemble at the length scale of sub-10 nm. However, such high-χ BCPs typically have imbalanced surface energies between respective blocks, making it a challenge to achieve desired perpendicular orientation. To address this challenge, we mixed a fluorine-containing polymeric additive with poly(2-vinylpyridine)-block-polystyrene-block-poly(2-vinylpyridine) (P2VP-b-PS-b-P2VP) and successfully controlled the orientation of the high-χ triblock copolymer. The additive selectively mixes with P2VP block through hydrogen bonding and can reduce the dissimilarity of surface energies between PS and P2VP blocks. After optimizing additive dose and annealing conditions, desired perpendicular orientation formed upon simple thermal annealing. We further

demonstrated DSA of this material system with 5 times density multiplication and a half pitch as small as 8.5 nm. This material system is also amenable to sequential infiltration synthesis treatment to selectively grow metal oxide in P2VP domains, which can facilitate the subsequent pattern transfer. We believe that this integration-friendly DSA platform using simple thermal annealing holds the great potential for sub-10 nm nanopatterning applications.

2.2 Introduction

The linear dimensions of transistors have been reduced by half every three years during the past five decades, which was mainly accomplished by reducing the wavelength of light used in lithography. Current state-of-the-art immersion photolithography tools using deep ultraviolet light with wavelength of 193 nm can reach 40 nm resolution limit with a single exposure. However, when the wavelength further goes down to the extreme ultraviolet at 13.5 nm, considerable challenges are faced such as the tool cost, uptime and stochastic variations. As an alternative technique for ultra-high resolution patterning, directed self-assembly (DSA) has attracted great academic and industrial interest since it was first introduced over a decade ago.[3]

DSA is a patterning technique that orders the self-assembling block copolymers (BCPs) using a chemical or topological template. The assembly of BCPs is well guided by the template, and the resulted structures resemble critical features in integrated circuits such as line/space and contact holes. DSA is especially attractive due to its ability to multiply the density of lithographical features on the template, denoted as density multiplication, which can extend optical lithography far beyond its current limits.[4] Polystyrene-*b*-poly(methyl methacrylate) (PS-*b*-PMMA) is the most widely studied BCP for DSA applications because of the similar surface energies of PS and PMMA blocks, which enables desired perpendicular orientation by thermal annealing with a free surface. DSA of PS-*b*-PMMA with 14 nm half pitch line/space pattern has been implemented on 300 mm

wafer processing line at IMEC with relatively low defect density, approaching that required for high volume manufacturing.[5] However, PS-*b*-PMMA has a resolution limit of 11 nm due to its low Flory−Huggins interaction parameter (χ), which prevents microphase separation and pattern transfer at smaller pitch. As a result, it is imperative to explore more BCPs with higher χ in order to achieve the desired sub-10 nm feature size.

One promising high-χ BCP is poly(2-vinyl-pyridine)-*block*-polystyrene-*block*-poly(2-vinyl-pyridine) (P2VP-*b*-PS-*b*-P2VP) with χ equal to 0.10 at 200°C compared with 0.037 for that of PS-*b*-PMMA.[6] Though higher χ enables P2VP-*b*-PS-*b*-P2VP (VSV) to microphase separate into lamellar structures at sub-10 nm feature size, forming perpendicularly oriented BCP domains remains a challenge due to imbalanced surface energies of PS and P2VP blocks.[7] The surface tension of PS is 40.7 mN/m and that of P2VP is 49.4 mN/m,[8] resulting in undesired parallel orientation upon annealing. Several approaches have been developed to circumvent the problem of dissimilar surface energies, including solvent vapor annealing,[9] vapor-phase deposited top coat and embedded neutral layer.[10,11] Despite the successful orientation control these approaches have achieved, challenges still remain to meet all the requirements for large scale manufacturing. For example, there is no solvent annealing tool currently available for manufacturing, and top coat approaches require additional processing steps, which lead to increased complexity and costs. The segregated neutral layer topcoat also brings challenges for pattern transfer by dry etching.

Our strategy to control the orientation of VSV is to use a fluorine-containing polymeric additive poly(hexafluoroalcohol styrene) (PHFAS), which enables perpendicular orientation of VSV by simple thermal annealing. The same polymeric additive has been shown to effectively tune the surface energies of other block copolymers.[12] PHFAS has lower surface energy than both PS and P2VP blocks, and it can selectively interact with P2VP via hydrogen bonding to lower the

apparent surface energy of P2VP block. By carefully adjusting the amount of PHFAS in the system, the surface energies of PS and P2VP blocks can be balanced and desired perpendicular orientation can form upon thermal annealing. After optimizing PHFAS dose and annealing conditions, we further demonstrate DSA of VSV/PHFAS with density multiplication on chemical patterns. We also investigate the pattern transfer potential of this material system assisted by sequential infiltration synthesis (SIS). Finally, we discuss the impact of molecular weight of PHFAS on orientation control and offer a simple yet effective way to predict the molecular weight of PHFAS needed for a given VSV.

2.3 Experimental

2.3.1 Materials

VSV with three different molecular weights (M_n=26 kg·mol^{-1}, 33 kg·mol^{-1} and 47 kg·mol^{-1}) were purchased from Polymer Source, Inc. PHFAS additives with two molecular weights (M_n=4.4 kg·mol^{-1}, M_w=5.9 kg·mol^{-1}; M_n=6.7 kg·mol^{-1}, M_w=9.5 kg·mol^{-1}) were synthesized via free radical polymerization as described elsewhere[12]. Hydroxyl-terminated polystyrene-*random*-poly(2-vinyl-pyridine) (PS-*r*-P2VP-OH) was synthesized in our group as previously reported[13]. Silicon <100> wafers were purchased from WRS Materials, LLC. All solvents were purchased from Aldrich and used as received.

2.3.2 Self-assembly of VSV with PHFAS additive

A solution of 1.5 wt% PS-*r*-P2VP-OH in dimethylformamide (DMF) was spin coated on clean silicon wafers followed by annealing at 200°C for 10 min under a nitrogen atmosphere. The brush was grafted on surface via reaction between hydroxyl group at the chain end and the silicon oxide surface. Ungrafted polymer brush was removed by sonication in DMF and the substrates were dried with nitrogen. The thickness of grafted brush was approximately 8 nm. Brush modified

wafers were then coated with 1 wt% VSV/PHFAS solution in DMF and annealed under a nitrogen atmosphere. The thickness of VSV/PHFAS film after annealing was approximately 20 nm.

2.3.3 Directed self-assembly of VSV with PHFAS additive

The DSA process was adapted from previously reported process.[14] Briefly, silicon wafers were spin coated with cross-linkable polystyrene solution and annealed at 250°C for 5 min under a nitrogen atmosphere to drive the crosslinking reaction. Chemical patterns were prepared using electron-beam lithography followed by exposure to oxygen plasma, which trimmed the crosslinked polystyrene (xPS) guiding stipes to the desired width. After oxygen plasma, the excess resist was removed by repeated sonication in N-methyl-2-pyrrolidone and chlorobenzene. Alternatively, silicon wafers with xPS guiding stripes were also received from IMEC prepared by a previously reported approach.[15] PS-*r*-P2VP-OH brush was then grafted onto the wafers and VSV film with optimized PHFAS dose was annealed under a nitrogen atmosphere.

2.4 Results and discussion

2.4.1 Orientation control of VSV with PHFAS additive

In order to achieve desired perpendicular orientation, both interfacial energies between substrate and BCP as well as surface energies between BCP and nitrogen atmosphere need to be balanced. Interfacial energies can be readily tuned by employing random copolymer brush with optimized PS content, which is non-preferential to respective blocks.[13] For VSV, however, surface energies are not balanced since surface energy of PS is lower than that of P2VP. To reduce this dissimilarity, we introduce PHFAS as a surface energy balancer to lower the apparent surface energy of P2VP block.

We first investigate two possible factors that might affect to the orientation control of VSV: PHFAS dose and annealing temperatures. We start with a relatively large VSV (47 $kg \cdot mol^{-1}$) to

optimize these factors following the schematic in Figure 2.1a. The substrate is modified with PS-*r*-P2VP-OH brush containing 48% PS, which has been identified non-preferential to VSV.[13] VSV solutions with various doses of PHFAS (M_w=9.5 kg·mol^{-1}) are spin-coated on brush modified substrates and annealed under nitrogen atmosphere at different temperatures.

When PHFAS dose is low (below 6 wt%), parallel lamellae are the predominant structures due to imbalanced surface energies (Figure 2.1b). PS block is more favored by the top surface than P2VP block due to its lower surface energy. As PHFAS dose increases, perpendicular orientation begins to form as a result of more balanced surface energies. When PHFAS dose reaches 12 wt% (with respect to VSV), full perpendicular orientation can be observed at 200℃. PHFAS is expected to stay in the P2VP block via the hydrogen bonding, and is likely to aggregate on top of the P2VP block during annealing because of its lower surface energy. Periodicity (L_0) of the self-assembled pattern is 23.0 nm as measured by Fast Fourier Transform (FFT) analysis of the top-down SEM images. It is worth noting that L_0 increases by approximately 7.5% compared with that from solvent annealing,[16] which can be attributed to two possible reasons. It is likely that the effective χ of VSV increases with the presence of PHFAS,[17] which can potentially lead to larger L_0 and lower line edge roughness. In this case, PHFAS is most likely only distributed in the P2VP block as we hypothesized. If PHFAS is equally distributed in both blocks, χ should decrease rather than increase. Alternatively, it is also possible that the presence of PHFAS can affect the chain conformations of P2VP block and thus increase L_0.

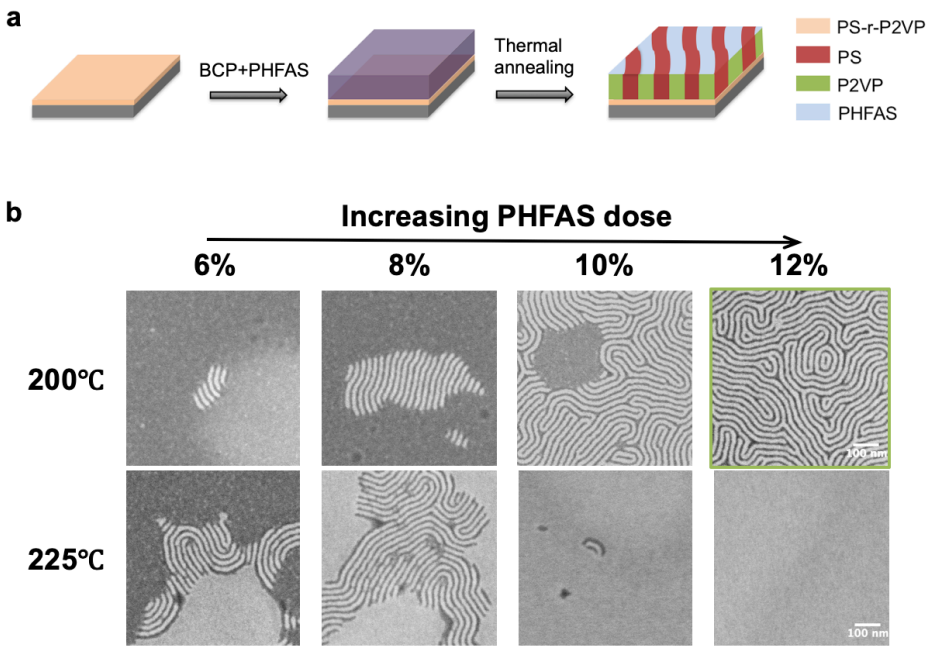

Figure 2.1 (a) Process flow for self-assembly of VSV with PHFAS additive. (b) SEM images of VSV with various doses of PHFAS upon thermal annealing on neutral substrates. Brighter domain is P2VP and darker domain is PS. Full perpendicular orientation forms with 12% PHFAS at 200 ℃. L_0 is 23.0 nm as measured from FFT analysis.

2.4.2 Directed self-assembly of VSV with PHFAS additive

The self-assembly of lamellae-forming BCPs can be directed using chemically contrast patterns comprising of guiding stripes of cross-linked homopolymer mat and interspatial random copolymer brush,[18] which is usually denoted as chemo-epitaxy DSA. The key to chemo-epitaxy DSA is the ability of BCPs to recognize the chemical patterns and align along the guiding stripes based on the wetting preference. It is crucial that VSV still preserves this ability when mixed with PHFAS.

The chemo-epitaxy DSA of VSV/PHFAS with 3 times density multiplication is demonstrated following the schematic shown in Figure 2.2a. The substrate is coated with xPS followed by E-beam lithography. After removing xPS in the exposed areas and trim etching the xPS guiding stripes underneath E-beam resist lines with oxygen plasma, the E-beam resist is

stripped and the exposed areas between xPS guiding lines are subsequently backfilled with the same neutral PS-*r*-P2VP-OH brush used in Figure 2.1. VSV (47k) with 12% PHFAS (9.5k) is spin-coated on chemical patterns and annealed at 200℃. Successful DSA with 23 nm full pitch (Figure 2.2c) is demonstrated on a template with the initial pitch L_s=69 nm (Figure 2.2b). This confirms that the presence of PHFAS does not impair the ability of VSV to recognize the chemical contrast of the chemical patterns and thus the standard chemo-epitaxy DSA scheme is still valid.

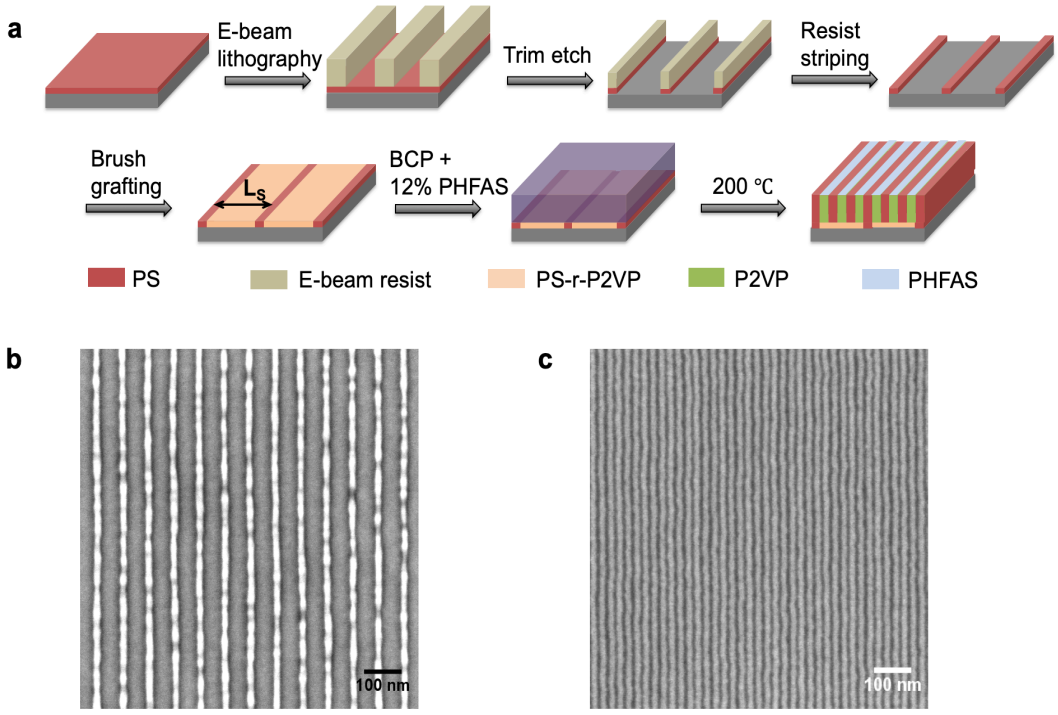

Figure 2.2 (a) Process flow for chemo-epitaxy DSA of VSV with PHFAS additive. (b) SEM image of the template after trim etch and (c) DSA pattern with 23.0 nm full pitch after assembly.

2.4.3 Mask conversion of BCP pattern with SIS

In order to implement the DSA line/space patterns for advanced patterning applications, the patterns need to be transferred from the BCP films to the underlying substrates, which desires high etching contrast between different blocks of the BCP. One effective way to increase the etching contrast of VSV is SIS, where metal oxide such as alumina selectively infiltrates the P2VP

block while PS block is relatively unaffected. VSV is then removed by oxygen plasma, leaving the alumina lines mimicking the original patterns of P2VP blocks which afterwards could be used as effective etching masks.[19] The alumina mask is more resistant to a variety of etching chemistries compared with the original soft matter films and thus could facilitate the direct pattern transfer to the underlying substrates without the need of an additional hard mask layer[9,10]. Our group has previously demonstrated pattern transfer of VSV to silicon substrates with 8 nm half pitch using this technique[9].

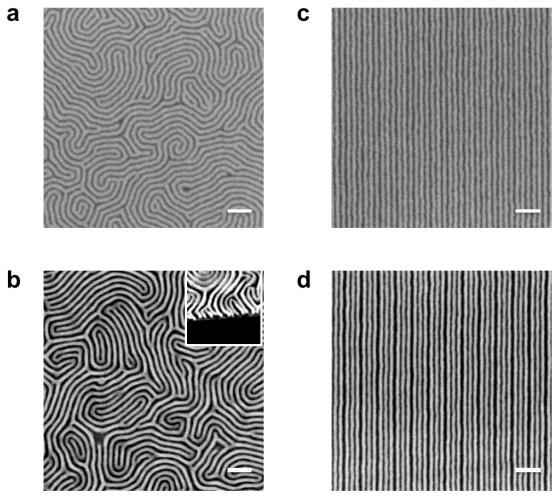

Figure 2.3 SEM images of assembled VSV (a, b) after SIS and (c, d) after oxygen plasma on neutral substrates and on chemical patterns. Scale bars represent 100 nm.

As PHFAS is also expected to form hydrogen bonding with the precursors of SIS, it is critical that the presence of PHFAS does not interfere with the SIS process. Figure 2.3 shows self-assembly pattern and DSA pattern of VSV/PHFAS after three cycles of SIS (Figure 2.3a, 2.3c) and after polymer removal by oxygen plasma (Figure 2.3b, 2.3d). The clear trenches after polymer removal indicate that no alumina has formed in PS domains, and no wetting layer has formed on top or at bottom of the film. This confirms that the presence of PHFAS does not affect SIS or bring extra complexities to the pattern transfer process compared with pure VSV. Though pitch walking

has been observed after polymer removal of the DSA pattern, it mainly comes from the DSA and pattern transfer process rather than the PHFAS, which can be improved by further optimizing the process such as using short PS brush[9] or adjusting the depth of alumina infiltration.

2.4.4 Effect of molecular weight of PHFAS on orientation control

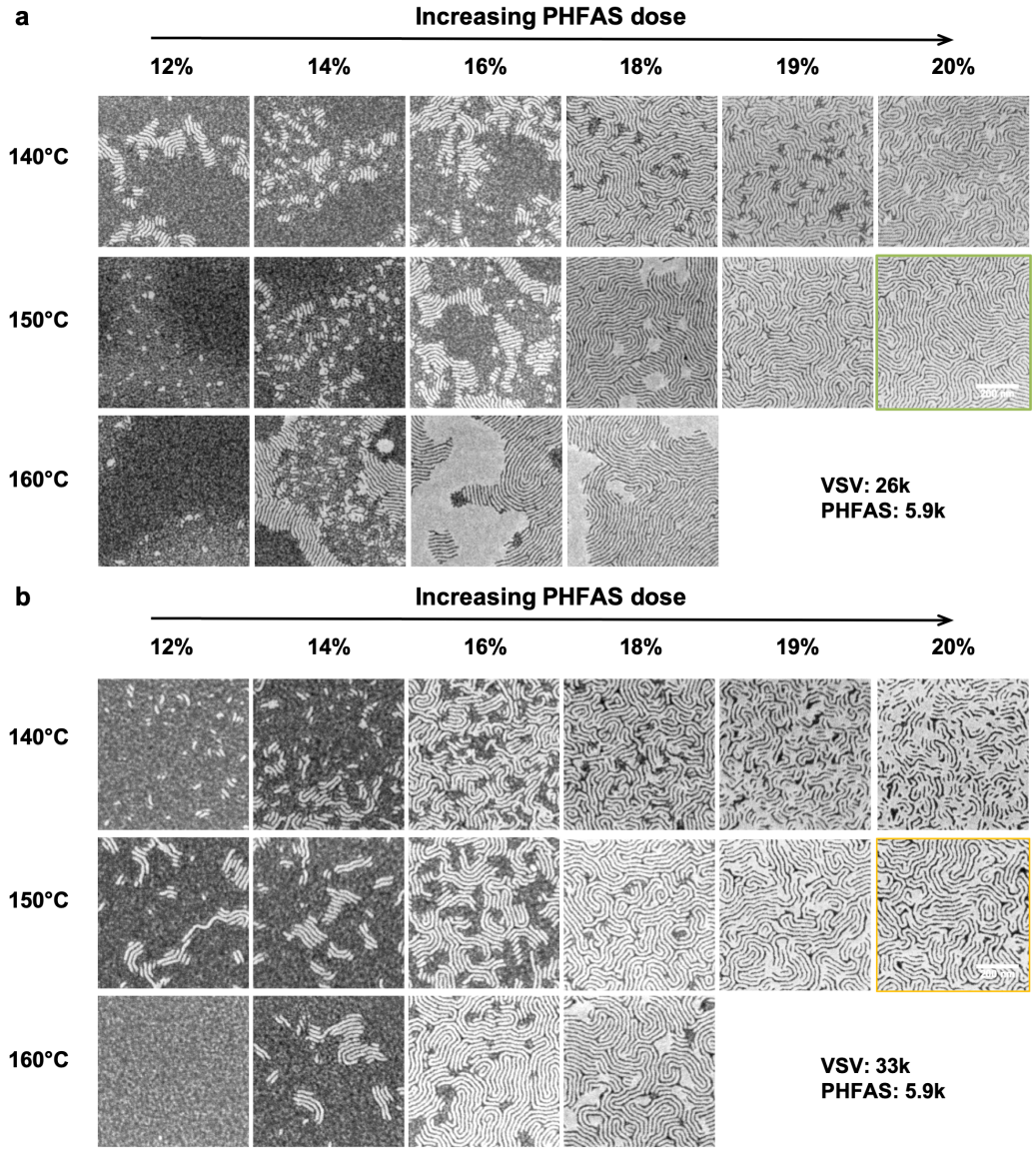

Figure 2.4 SEM images of 26k VSV and 33k VSV with various doses of 5.9k PHFAS upon thermal annealing on neutral substrates. (a) For 26k VSV, full perpendicular orientation forms with 20% PHFAS at 150°C. (b) For 33k VSV, no full perpendicular orientation can be observed. Scale bars represent 200 nm.

We have shown that PHFAS can effectively control the orientation of VSV (47k) and achieved DSA line/space pattern with 23 nm full pitch. In order to apply the same strategy to smaller VSV for sub-10 nm patterning, we investigate the effect of molecular weight of PHFAS on orientation control. We use VSV with three molecular weights (26k, 33k and 47k) and PHFAS with two molecular weights (5.9k and 9.5k).

The PHFAS dose and annealing conditions were optimized for each VSV. For 26k and 33k VSV, no meaningful results could be observed when mixed with 9.5k PHFAS. This is presumably because the size of PHFAS needs to be similar as or smaller than the P2VP block in order for it to interact effectively with the P2VP block, which is further supported by the results when the VSV was mixed with smaller PHFAS. When 26k VSV was mixed with 5.9k PHFAS (Figure 2.4a), similar results were observed as that of 47k VSV mixed with 9.5k PHFAS. Perpendicular orientation began to form as PHFAS dose increased, and full perpendicular lamellae have been achieved with 20% PHFAS at 150°C. For 33k VSV, however, the self-assembled pattern contained many defects after optimization, which could be potentially attributed to the aggregation of PHFAS on top, since PHFAS is also amenable to SIS. Alternatively, the defects could also possibly come from the parallel orientation of VSV with P2VP on top. A more detailed study, such as transmission electron microscopy energy-dispersive X-ray spectroscopy (TEM-EDX) would be required to determine the origin of the defects, which could be investigated in the future work. Nevertheless, we have shown that these defects could be eliminated by optimizing molecular weight of PHFAS.

Table 2.1 Effect of molecular weight of PHFAS on orientation control.

M_{VSV} (g/mol)	M_{PHFAS} (g/mol)	M_{PHFAS}/M_{VSV}	Result
33k	5.9k	**0.18**	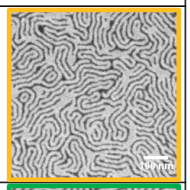
47k	9.5k	**0.20**	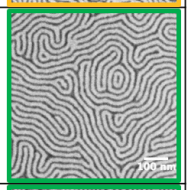
26k	5.9k	**0.23**	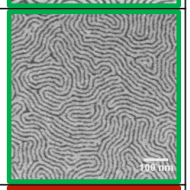
33k	9.5k	**0.29**	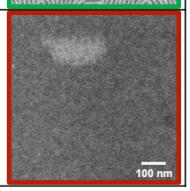

For a more quantitative analysis, we further calculate the ratio of molecular weight of PHFAS (M_{PHFAS}) to the molecular weight of VSV (M_{VSV}), and compare it with the optimized orientation control results as summarized in Table 2.1. When the ratio is 0.18, after optimizing PHFAS dose and annealing conditions, perpendicular orientation can be observed, however the optimized result still shows defective areas. As the M_{PHFAS}/M_{VSV} ratio increases, orientation control also improves and fully perpendicular lamellae can be achieved. When the ratio is too high, however, no perpendicular orientation can be observed. Consequently, the orientation is best controlled when the ratio is between 0.20 and 0.23, which can provide us a preliminary prediction of the PHFAS size needed for a given VSV.

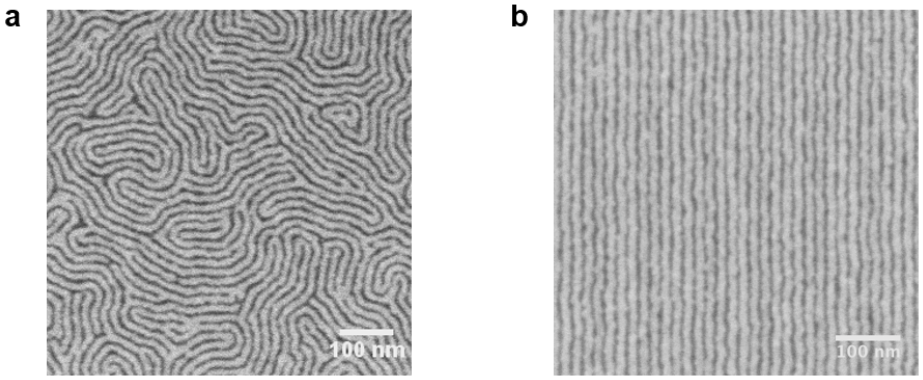

Figure 2.5 SEM images of (a) self-assembled VSV on neutral substrate and (b) DSA pattern with 5× density multiplication. L_0 is 17.0 nm as measured by FFT analysis.

Among all the combinations, the VSV/PHFAS pair we chose for sub-10 nm patterning is 26k VSV mixed with 20% 5.9k PHFAS (Figure 2.5a). L_0 is 17.0 nm as measured from FFT analysis. Following the same chemo-epitaxy DSA flow, we achieved 5 times density multiplication on chemical patterns comprising of xPS guiding stripes and neutral brush (Figure 2.5b). This confirms that our strategy applies to VSV with various molecular weights and periodicities, and therefore can be an effective solution to sub-10 nm patterning.

2.5 Conclusions

In this study, we have demonstrated that PHFAS can effectively balance the surface energies of PS and P2VP blocks, and enable perpendicular orientation of VSV upon simple thermal annealing. After optimizing PHFAS dose and annealing temperatures, we were able to achieve full perpendicular orientation of VSV with L_0 as small as 17 nm. Successful chemo-epitaxy DSA with density multiplication was demonstrated, and pattern transfer potential of this material system has been revealed. We also investigated the relationship between molecular weight of PHFAS and that of VSV, and provided a preliminary prediction of the PHFAS size needed for a given VSV for optimal orientation control. This approach offers an effective solution for sub-10 nm patterning with simple thermal annealing, and can be potentially generalized to other high-χ BCPs as well.

2.6 References

(1) Li, J.; Zhou, C.; Chen, X.; Rincon Delgadillo, P. A.; Nealey, P. F. *J. Micro/Nanolithography, MEMS, MOEMS* **2019**, *18* (03), 035501.

(2) Li, J.; Zhou, C.; Chen, X.; Rincon-Delgadillo, P. A.; Nealey, P. F. *Proc. SPIE* **2018**, *10586*, 105860V.

(3) Kim, S. O.; Solak, H. H.; Stoykovich, M. P.; Ferrier, N. J.; De Pablo, J. J.; Nealey, P. F. *Nature* **2003**, *424* (6947), 411–414.

(4) Ruiz, R.; Kang, H.; Detcheverry, F. A.; Dobisz, E.; Kercher, D. S.; Albrecht, T. R.; de Pablo, J. J.; Nealey, P. F. *Science* **2008**, *321* (5891), 936–939.

(5) Gronheid, R.; Rincon Delgadillo, P.; Pathangi, H.; Van den Heuvel, D.; Parnell, D.; Chan, B. T.; Lee, Y.-T.; Van Look, L.; Cao, Y.; Her, Y.; Lin, G.; Harukawa, R.; Nagaswami, V.; D'Urzo, L.; Somervell, M.; Nealey, P. *Proc. SPIE* **2014**, *9049*, 904905.

(6) Gu, X.; Gunkel, I.; Russell, T. P. *Philos. Trans. R. Soc. A Math. Phys. Eng. Sci.* **2013**, *371* (2000), 20120306–20120306.

(7) Sauer, B. B.; Dee, G. T. *Macromolecules* **2002**, *35* (18), 7024–7030.

(8) Mark, J. E. *Physical Properties of Polymers Handbook, Second Edition*; Springer, **2007**.

(9) Xiong, S.; Wan, L.; Ishida, Y.; Chapuis, Y. A.; Craig, G. S. W.; Ruiz, R.; Nealey, P. F. *ACS Nano* **2016**, *10* (8), 7855–7865.

(10) Suh, H. S.; Kim, D. H.; Moni, P.; Xiong, S.; Ocola, L. E.; Zaluzec, N. J.; Gleason, K. K.; Nealey, P. F. *Nat. Nanotechnol.* **2017**, *12* (6), 575–581.

(11) Zhang, J.; Clark, M. B.; Wu, C.; Li, M.; Trefonas, P.; Hustad, P. D. *Nano Lett.* **2016**, *16* (1), 728–735.

(12) Vora, A.; Schmidt, K.; Alva, G.; Arellano, N.; Magbitang, T.; Chunder, A.; Thompson, L. E.; Lofano, E.; Pitera, J. W.; Cheng, J. Y.; Sanders, D. P. *ACS Appl. Mater. Interfaces* **2016**, *8* (43), 29808–29817.

(13) Ji, S.; Liu, C.-C.; Son, J. G.; Gotrik, K.; Craig, G. S. W.; Gopalan, P.; Himpsel, F. J.; Char, K.; Nealey, P. F. *Macromolecules* **2008**, *41* (23), 9098–9103.

(14) Liu, C.-C.; Han, E.; Onses, M. S.; Thode, C. J.; Ji, S.; Gopalan, P.; Nealey, P. F. *Macromolecules* **2011**, *44* (7), 1876–1885.

(15) Delgadillo, P. A. R.; Gronheid, R.; Thode, C. J.; Wu, H.; Cao, Y.; Neisser, M.; Somervell, M.; Nafus, K.; Nealey, P. F. *J. Micro/Nanolithography, MEMS, MOEMS* **2012**, *11* (3), 031302.

(16) Sun, Z.; Chen, Z.; Zhang, W.; Choi, J.; Huang, C.; Jeong, G.; Coughlin, E. B.; Hsu, Y.; Yang, X.; Lee, K. Y.; Kuo, D. S.; Xiao, S.; Russell, T. P. *Adv. Mater.* **2015**, *27* (29), 4364–4370.

(17) Matsushita, Y.; Mori, K.; Saguchi, R.; Nakao, Y.; Noda, I.; Nagasawa, M. *Macromolecules* **1990**, *23* (19), 4313–4316.

(18) Liu, C. C.; Ramírez-Hernández, A.; Han, E.; Craig, G. S. W.; Tada, Y.; Yoshida, H.; Kang, H.; Ji, S.; Gopalan, P.; De Pablo, J. J.; Nealey, P. F. *Macromolecules* **2013**, *46* (4), 1415–1424.

(19) Tseng, Y. C.; Peng, Q.; Ocola, L. E.; Elam, J. W.; Darling, S. B. *J. Phys. Chem. C* **2011**, *115* (36), 17725–17729.

Chapter 3: A Kinetic Approach to Defect Reduction in Directed Self-Assembly

* This chapter has been published in Journal of Micro/Nanolithography, MEMS, and MOEMS ("Kinetic Approach to Defect Reduction in Directed Self-Assembly", Li, J.; Rincon-Delgadillo, P. A.; Suh, H. S.; Mannaert, G.; Nealey, P. F. *J. Micro/Nanolithography, MEMS, MOEMS* **2019**, *18* (04), 043502) and Proceedings of SPIE ("Kinetics of Defect Annihilation in Chemo-Epitaxy Directed Self-Assembly", Li, J.; Rincon-Delgadillo, P. A.; Suh, H. S.; Mannaert, G.; Nealey, P. F. *Proc. SPIE* **2019**, *10960*, 109600V).[1,2]

3.1 Abstract

As a potential solution to next-generation nanolithography, directed self-assembly (DSA) of block copolymers (BCPs) is still restrained in high volume manufacturing primarily due to its defectivity issue. Though defects possess greater free energies than aligned morphologies and are highly energetically unfavorable, they can be kinetically trapped by the energy barriers and persist for a long time during annealing. Therefore, understanding the kinetics of defect annihilation is crucial to revealing the mechanism of defect formation and to further reducing defectivity in DSA. In this work, we focus on two types of predominant defects in DSA——dislocation and bridge. Kinetic model of each defect type is developed through statistical analysis of experimental data, providing insight into possible approaches of further defect reduction. We also investigate the impact of annealing temperature and film thickness on annihilation kinetics, and discuss the reasons behind the observed results. By simply optimizing annealing conditions and film thickness, we have successfully reduced the total defect density by one order of magnitude. Though these findings are based on polystyrene-*b*-poly(methyl methacrylate) (PS-*b*-PMMA), we anticipate they could be readily applied to other BCP platforms as well.

3.2 Introduction

Directed self-assembly (DSA) of block copolymers (BCPs) has attracted considerate interest from both academia and industries since it was first introduced over one decade ago[3]. DSA utilizes lithographically defined template, with chemical or topographic contrast, to order the self-assembling BCPs into periodic nanostructures which resemble critical features in integrated circuits such as line/space and contact holes. Since DSA can readily multiply the lithographical features of the template and increase the pattern resolution severalfold[4], it holds the advantage over many other multiple patterning techniques in terms of process simplicity and cost effectiveness. However, despite the great progress DSA has achieved, its application is still restricted in high volume manufacturing due to the remaining challenge in defectivity, which typically requires a defect density lower than 1 cm^{-2} for memories and 0.01 cm^{-2} for logic applications.

In order to thoroughly investigate the defectivity of DSA and evaluate its readiness for manufacturing, a chemo-epitaxy DSA process, known as Liu-Nealey (LiNe) flow, has been implemented on the 300 mm wafer processing line at IMEC a few years ago[5]. Extensive analysis and optimization have been made to determine the critical factors affecting the defectivity in DSA. Factors from each processing step and material have been identified[6], and various parameters have been optimized such as pattern pitch, guiding stripe width, template topography, background chemistry and annealing conditions[7–9]. Though these extensive efforts have led to significant progress in defect reduction in DSA, they mainly examine the assembled structures close to thermodynamic equilibrium, and provide little information about the kinetics of defect annihilation during the annealing.

Recent simulation study has revealed that kinetics of DSA, in addition to thermodynamics, also plays an important role in defect formation and annihilation[10,11]. Though defects possess

greater free energies than defect-free structures and are highly energetically unfavorable, they can be kinetically trapped and persist for a long time before being annihilated. This indicates that defects are actually metastable structures with kinetic barriers rather than equilibrium structures. Consequently, it is critical to understand the kinetics of defect annihilation in order to develop an insight into the mechanism of defect formation and to further reduce defectivity in DSA.

In this kinetic study, we mainly focus on dislocation and bridge defects, since they are the primary contributors to the total defect density in DSA. Dislocation is a DSA-specific defect and is of particular concern, because it is difficult to eliminate dislocations by subsequent steps such as etching. We would like to investigate whether there is any theoretical constraint of dislocation annihilation, in other words, whether it is possible to fully eliminate the dislocations by the annealing step. In addition to dislocation, bridge constitutes the largest proportion of the defect density, and is also of great interest for defect reduction. By collecting defectivity data at different annealing time and annealing conditions, we develop kinetic models for both dislocation and bridge, and have investigated the impact of annealing temperature and film thickness on defect density, which provides valuable guidance for further defect reduction in DSA.

3.3 Experimental

3.3.1 Materials

Cross-linkable polystyrene (xPS, NLD128) and hydroxyl-terminated polystyrene-*random*-poly(methyl methacrylate) (PS-*r*-PMMA-OH, NLD127) were synthesized by Merck Performance Materials. Periodicity of PS-*b*-PMMA is approximately 28 nm. ArF immersion photoresist AIM5484 was provided by JSR Micro. Organic solvent RER600 was purchased from Fujifilm and Orgasolv STR 301 was purchased from BASF.

3.3.2 Process

The DSA process was based on previously reported LiNe flow at IMEC[5,6,12]. Briefly, 300 mm silicon wafers were deposited with 13 nm SiN as anti-refractive layers, followed by spin-coating and annealing of 8 nm xPS. Exposure was performed on ASML NXT 1970Ci (NA= 1.35, σ_o=0.87, σ_i=0.72), and line width of xPS was trimmed on Lam E5. For 3× density multiplication of 28 nm PS-*b*-PMMA, the pitch of template was 84 nm and the optimized line width of xPS guiding stripe was approximately 21 nm. Line width of guiding stripe was measured on Hitachi CD-SEM CG5000 before removing the remaining photoresist by Orgasolv STR 301. PS-*r*-PMMA-OH brush was spin-coated and annealed at 250℃ for 5 min in N_2 atmosphere, and extra brush was rinsed with RER600. PS-*b*-PMMA was then coated on the chemical pattern and annealed in N_2 atmosphere. Coating of xPS, PS-*r*-PMMA-OH brush and PS-*b*-PMMA was performed on TEL CLEAN TRACK™ LITHIUS Pro™ Zi, and all other coating and annealing were done on TEL CLEAN TRACK™ ACT™12.

3.3.3 Defect inspection

After pattern transfer to the underlying substrates, defect inspection was done on KLA-Tencor 2825 and eDR-7110. A schematic of defect inspection is shown in Figure 3.1. DSA pattern was transferred to the underlying silicon wafer coated with 13 nm SiN, which provided effective reflectivity for optical inspection. Optical inspection was conducted on 300 mm full wafer with a total inspection area of 46 cm^2 to obtain sufficient statistics and to minimize random errors. Optical inspection provided location of defects as well as a rough classification of defect types, which could be corrected by SEM review to obtain a more accurate classification. After optical inspection and SEM review, density of each defect type could be readily calculated. To ensure that all defects

could be captured, we employed extremely high sensitivity for optical inspection and were able to detect very small defects such as baby bridges.

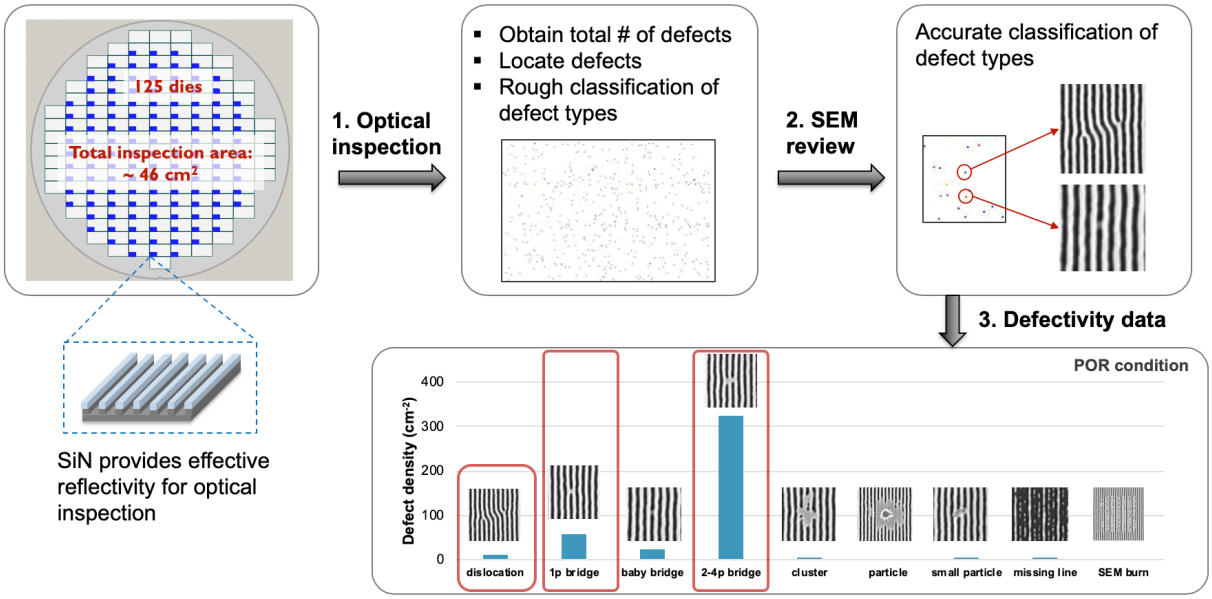

Figure 3.1 Schematic of defect inspection. DSA pattern is transferred to the underlying substrate, followed by optical inspection and SEM review. Density of each defect type can be calculated.

3.4 Results and discussion

3.4.1 Kinetics of defect annihilation

To study the kinetics of defect annihilation, we collect defectivity data at different annealing time and investigate how defectivity evolves with time. In this work, we focus on two primary defect types in DSA——dislocation and bridge, since other defects only show limited contribution to the total defect density. Bridges are further divided into 1 period (1p) bridges and 2~4 periods (2-4p) bridges. Dislocation density and bridge density are plotted as a function of annealing time as shown in Figure 3.2. Dislocation density and 2-4p bridge density both decrease with annealing time, whereas no apparent trend is observed for 1p bridge.

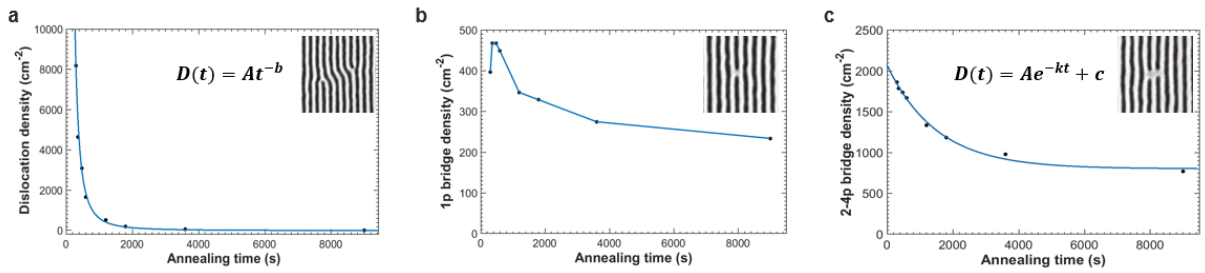

Figure 3.2 Kinetics of defect annihilation. (a) Dislocation annihilation follows power law. (b) 1p bridge density shows weak time dependence. (c) 2-4p bridge density decreases exponentially with time, and reaches a plateau at long annealing time.

We fit the data with various models such as power law, single exponential, double exponential and stretched exponential to determine the best model for each defect type. It turns out that dislocation annihilation can be well modeled by power law, indicating that dislocation annihilation is a complex process with a distribution of multiple energy barriers[13]. This is in good agreement with simulation studies, where multiple energy barriers have been found to be associated with different kinetic processes[10,11,14]. 1p bridge shows relatively weak time dependence, and no appropriate model could be found to fit the data. We anticipate the main source of 1p bridge to be impurities of materials or particles from processing, which are independent of time. For 2-4p bridge, there are two components contributing to the total density. The kinetic component (Ae^{-kt}) decreases exponentially with annealing time, indicating that this is a simple kinetic process governed by a single energy barrier. The other component (c), however, is constant throughout time and shown as the plateau in Figure 3.2c, which could be inherent to the materials or processing.

3.4.2 Impact of annealing temperature and film thickness on dislocation annihilation

It has been shown that annealing temperature and film thickness could have a significant impact on kinetics of alignment in DSA[15]. In order to investigate their impact on defectivity, which

happens after alignment, we compare kinetics of dislocation annihilation at different annealing temperatures (T) and film thickness (FT).

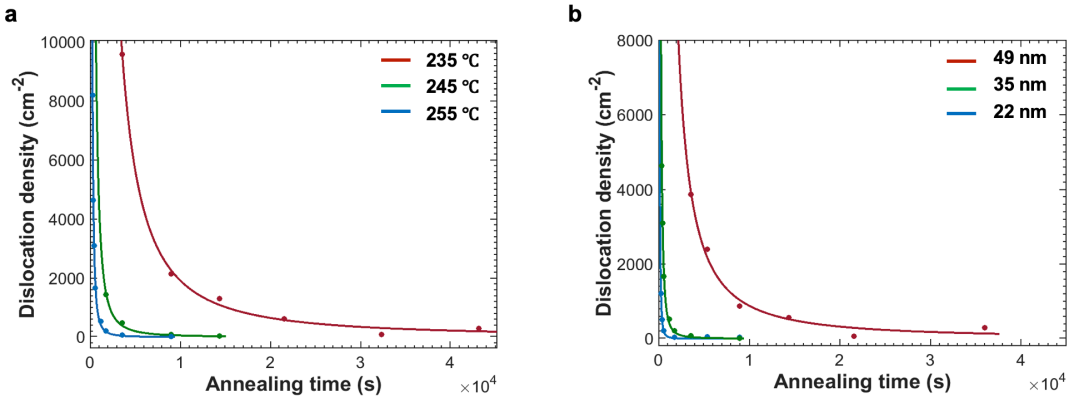

Figure 3.3 Dislocation annihilation at different annealing temperatures and film thickness. (a) Kinetics increases with annealing temperature, and (b) decreases with film thickness.

Dislocation annihilation can be well fitted with power law model at different annealing temperatures and film thickness, further validating the model we have developed. It is not surprising that higher annealing temperature results in faster kinetics, since mobility of polymers increases with temperature. To make a more direct comparison, we calculate the time required to reach 10 dislocations/cm^2 and 1 dislocation/cm^2 based on the fitted models at different temperatures, and the results are summarized in Table 3.1.

Table 3.1 Time to reach 10 dislocations/cm^2 and 1 dislocation/cm^2 at different annealing temperatures (FT=35 nm)

Annealing temperature (°C)	**235**	**245**	**255**
Time required to reach 10 dislocations/cm^2 (h)	79.3	6.4	1.9
Time required to reach 1 dislocation/cm^2 (h)	343.5	20.8	5.6

As expected, it takes significantly longer time to reach the same level of dislocation density at lower temperature. Only 10 °C decrease in annealing temperature can result in several fold or

even one order of magnitude longer time. As a result, higher temperature should be favored as long as it does not cause degradation of polymers or interfere with DSA, since temperature also affects Flory-Huggins parameters and interfacial energies[16,17], which are crucial to the assembly process.

We further examine the impact of film thickness on kinetics of dislocation annihilation, and the results are shown in Table 3.2. Thicker film (FT=49 nm) shows significantly slower kinetics than thinner film (FT=22 nm and 35 nm), and requires two orders of magnitude longer annealing time to reach same level of dislocation density. We anticipate this disparity to come from the ordering mechanism of DSA. It has been previously reported that there is a distinct kinetic regime for film thickness greater than 1.64 L_0[15], corresponding to 46 nm for BCP with 28 nm L_0, which exhibits much slower kinetics.

Table 3.2 Time to reach 10 dislocations/cm^2 and 1 dislocation/cm^2 at different film thickness (T=255°C)

Film thickness (nm)	**22**	**35**	**49**
Time required to reach 10 dislocation/cm^2 (h)	0.5	1.9	60.2
Time required to reach 1 dislocation/cm^2 (h)	1.3	5.6	291.7

It is worth noticing that the kinetics derived here describes the overall performance of the whole DSA process involving multiple materials and processing steps, rather than the annealing step itself. Previous study has shown that each step in the DSA process, such as pinholes in xPS mat and particles from brush grafting, can all contribute to the defectivity[6]. Some of these defects can be eliminated by BCP annealing, whereas others persist through the whole process and contribute to the final defectivity. As a result, each step of the DSA process needs to be optimized to improve the overall kinetics of defect annihilation.

3.4.3 Impact of annealing temperature and film thickness on bridge annihilation

In addition to dislocation, we also investigate the impact of annealing temperature and film thickness on bridge annihilation. Bridge annihilation at different annealing temperatures also follows the model we developed earlier. For 1p bridge, no apparent time dependence is observed. For 2-4p bridge, the dependence of bridge density on annealing time can be well fitted with first order exponential decay ($Ae^{-kt} + c$), where k increases with annealing temperature.

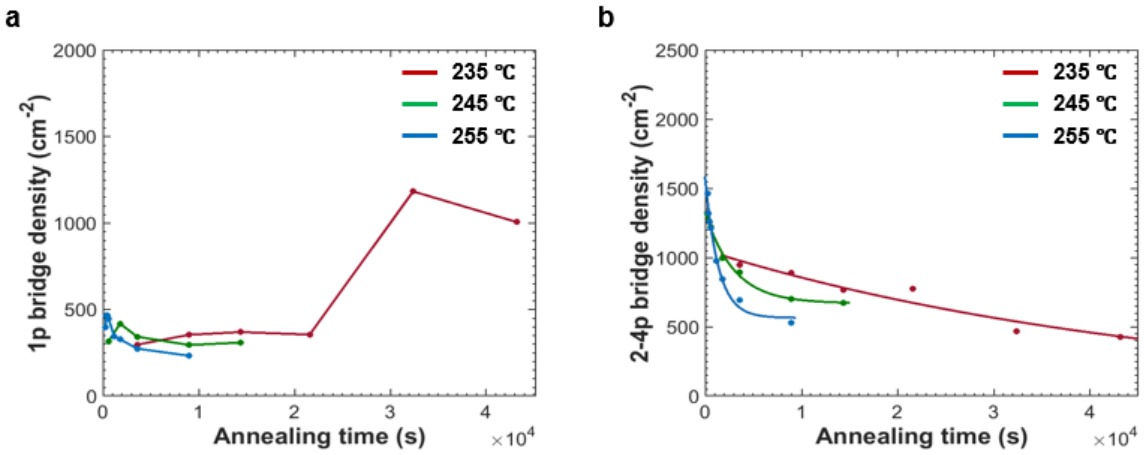

Figure 3.4 Impact of annealing temperature on bridge annihilation. (a) For 1p bridge, no apparent trend is observed, and for (b) 2-4p bridge, evolution of bridge density follows first order exponential decay.

Unlike dislocations, which can ideally be fully eliminated by increasing annealing time, bridges can persist through the whole annealing process. To reduce the bridge density, we further study the impact of film thickness as shown in Figure 3.5.

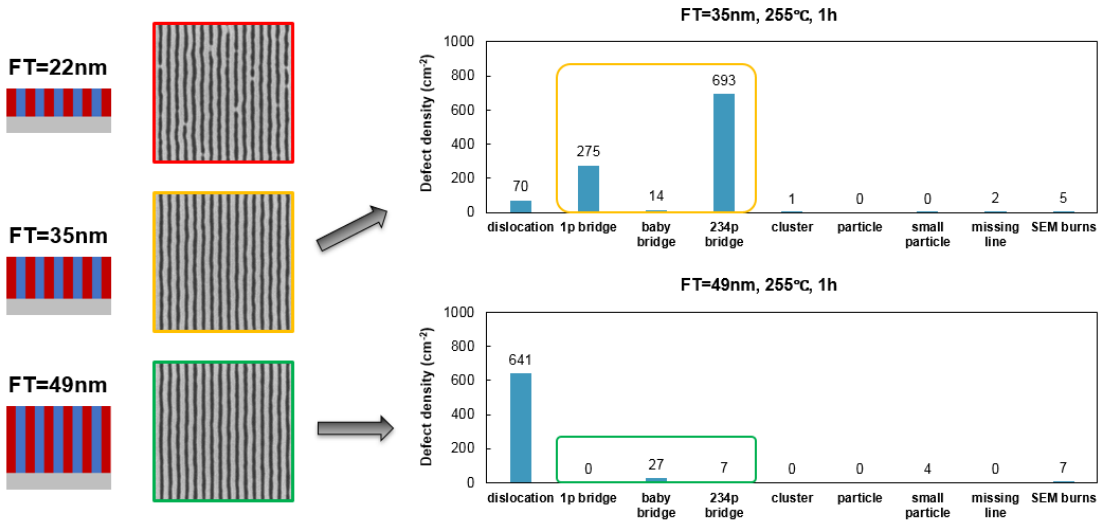

Figure 3.5 Impact of film thickness on bridge density. Bridge density decreases significantly as film thickness increases.

We compare bridge density at three different film thickness under the same annealing conditions. For thin film of 22 nm, bridge density is extremely high after pattern transfer, and multiple bridges can be observed in a typical SEM image. When film thickness increases to 35 nm, bridge density is reduced significantly, and a typical SEM image does not show any bridge. As film thickness increases to 49 nm, bridge density is further reduced by more than one order of magnitude, though the dislocation density is higher due to slower kinetics.

There are two possible explanations of why thicker film exhibits lower bridge density: (1) bridges are removed during annealing, or (2) bridges are removed during the pattern transfer. We are more in favor of the second hypothesis, because previous tomography study has revealed that bridges are generally not throughout the whole film[18]. Bridges can occur at the bottom of the BCP film even when defect-free alignment is observed at the top of the film. We anticipate that PS bridges buried under the PMMA domains can be removed during pattern transfer. The pattern transfer contains two main steps— BCP etching and Si etching, where BCP etching selectively removes the PMMA domain before Si etching transfers the pattern into the substrate. For thicker

film, it is likely that the PS bridges at the bottom can be etched after PMMA is fully removed, since the time of BCP etching is longer for thicker film. As a result, PS bridges are not transferred to the underlying substrates, and the eventual bridge density is reduced.

3.4.4 Impact of wet etching on bridge reduction

To further verify our hypothesis that bridges mainly occur at the bottom of film and can be removed during pattern transfer, we introduce a wet etching step before pattern transfer for thin film of 22 nm. Wet etching can selectively remove the PMMA domain with extremely high selectivity by degrading PMMA with ultraviolet (UV) exposure, whereas the PS domain is relatively unaffected. If our hypothesis is correct, the buried PS bridges will become exposed after PMMA is removed by wet etching, leading to significantly lower bridge density after pattern transfer.

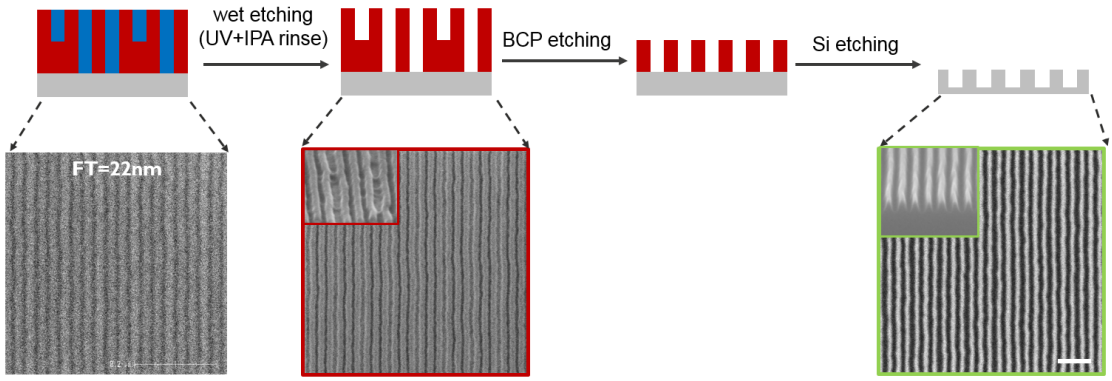

Figure 3.6 Pattern transfer of 22 nm BCP film with wet etching included. Wet etching selectively removes the PMMA domain and reveals the buried PS bridges, which are clearly visible in the cross-section SEM image. Exposed bridges can be removed during BCP etching, leading to significantly reduced bridge density. Scale bar represents 100 nm.

As shown in Figure 3.6, PS bridges are clearly revealed after the PMMA domain is removed by wet etching. Bridges mainly form over the backfill brush rather than guiding stripe sidewalls, agreeing well with the previous study[8]. After pattern transfer, no bridge can be observed in a typical SEM image, and the clean trenches are confirmed by cross-section SEM imaging,

which confirms our hypothesis that PS bridges are indeed buried under PMMA domains. Moreover, it is also strong evidence that bridges can be removed by optimizing etching conditions.

3.5 Conclusions

We have investigated the kinetics of defect annihilation in chemo-epitaxy DSA using state-of-the-art defect inspection tools. Two primary defect types in DSA have been studied—dislocation and bridge. Dislocation annihilation is best fitted with power law, and can ideally be eliminated by thermal annealing. Higher annealing temperature and thinner film should be favored to eliminate the dislocations faster. On the other hand, 2-4p bridge reaches a plateau at long annealing time and cannot be further reduced, which could be attributed to impurities in materials, volume fraction mismatch of BCP, or particles accumulated from processing[19]. Thinner film shows higher density of bridges, which can be removed by optimizing etching conditions such as including a wet etching step or increasing etching selectivity of the two blocks. Consequently, in order to reduce defectivity in DSA, one can employ thin film and reduce bridge defects by optimizing etching conditions. Alternatively, thick film can be chosen in favor of bridge reduction, but higher annealing temperature and longer annealing time would be required to eliminate the dislocation. By simply co-optimizing film thickness and annealing conditions, as shown in Figure 3.7, the total defect density can be reduced by one order of magnitude compared with previously optimized condition. Though these results were obtained from PS-*b*-PMMA, which is the only available platform for such a fundamental study, we anticipate they could be readily applied to other BCP platforms as well. Based on the understanding of defect kinetics, in combination with further optimization of the chemistry and geometry of the DSA process, we believe it is possible to ultimately reach the required defectivity level for high volume manufacturing.

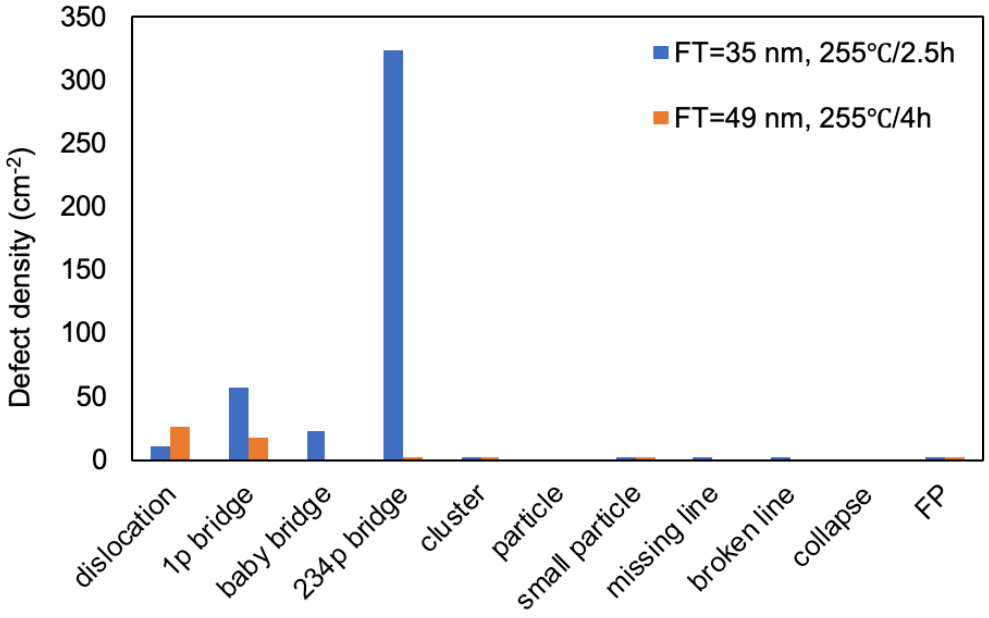

Figure 3.7 Total defect density is reduced by one order of magnitude by using thicker film and longer annealing time.

3.6 References

(1) Li, J.; Rincon-Delgadillo, P. A.; Suh, H. S.; Mannaert, G.; Nealey, P. F. *Proc. SPIE* **2019**, *10960*, 109600V.

(2) Li, J.; Rincon-Delgadillo, P. A.; Suh, H. S.; Mannaert, G.; Nealey, P. F. *J. Micro/Nanolithography, MEMS, MOEMS* **2019**, *18* (04), 043502.

(3) Kim, S. O.; Solak, H. H.; Stoykovich, M. P.; Ferrier, N. J.; De Pablo, J. J.; Nealey, P. F. *Nature* **2003**, *424* (6947), 411–414.

(4) Ruiz, R.; Kang, H.; Detcheverry, F. A.; Dobisz, E.; Kercher, D. S.; Albrecht, T. R.; de Pablo, J. J.; Nealey, P. F. *Science* **2008**, *321* (5891), 936–939.

(5) Delgadillo, P. A. R.; Gronheid, R.; Thode, C. J.; Wu, H.; Cao, Y.; Neisser, M.; Somervell, M.; Nafus, K.; Nealey, P. F. *J. Micro/Nanolithography, MEMS, MOEMS* **2012**, *11* (3), 031302.

(6) Delgadillo, P. R.; Suri, M.; Durant, S.; Cross, A.; Nagaswami, V. R.; Heuvel, D. Van Den; Gronheid, R.; Nealey, P. *J. Micro/Nanolithography, MEMS, MOEMS* **2013**, *12* (3), 031112.

(7) Garner, G. P.; Rincon Delgadillo, P.; Gronheid, R.; Nealey, P. F.; De Pablo, J. J. *Mol. Syst. Des. Eng.* **2017**, *2* (5), 567–580.

(8) Williamson, L. D.; Seidel, R. N.; Chen, X.; Suh, H. S.; Rincon Delgadillo, P.; Gronheid, R.; Nealey, P. F. *ACS Appl. Mater. Interfaces* **2016**, *8* (4), 2704–2712.

(9) Pathangi, H.; Chan, B. T.; Bayana, H.; Vandenbroeck, N.; Heuvel, D. Van Den; Look, L. Van; Rincon-Delgadillo, P.; Cao, Y.; Kim, J.; Lin, G.; Parnell, D.; Nafus, K.; Harukawa, R.; Chikashi, I.; Polli, M.; D'Urzo, L.; Gronheid, R.; Nealey, P. *J. Micro/Nanolithography, MEMS, MOEMS* **2015**, *14* (3), 031204.

(10) Hur, S.-M.; Thapar, V.; Ramírez-Hernández, A.; Khaira, G.; Segal-Peretz, T.; Rincon-Delgadillo, P. A.; Li, W.; Müller, M.; Nealey, P. F.; de Pablo, J. J. *Proc. Natl. Acad. Sci.* **2015**, *112* (46), 14144–14149.

(11) Hur, S.-M.; Thapar, V.; Ramírez-Hernández, A.; Nealey, P. F.; de Pablo, J. J. *ACS Nano* **2018**, *12* (10), 9974–9981.

(12) Gronheid, R.; Rincon Delgadillo, P.; Pathangi, H.; Van den Heuvel, D.; Parnell, D.; Chan, B. T.; Lee, Y.-T.; Van Look, L.; Cao, Y.; Her, Y.; Lin, G.; Harukawa, R.; Nagaswami, V.; D'Urzo, L.; Somervell, M.; Nealey, P. F. *Proc. SPIE* **2014**, *9049*, 904905.

(13) McNeil, I. J.; Ashford, D. L.; Luo, H.; Fecko, C. J. *J. Phys. Chem. C* **2012**, *116* (30), 15888–15899.

(14) Li, W.; Müller, M. *Macromolecules* **2016**, *49* (16), 6126–6138.

(15) Ren, J.; Zhou, C.; Chen, X.; Dolejsi, M.; Craig, G. S. W. W.; Rincon Delgadillo, P. A.; Segal-Peretz, T.; Nealey, P. F. *ACS Appl. Mater. Interfaces* **2018**, *10* (27), 23414–23423.

(16) Russell, T. P.; Hjelm, R. P.; Seeger, P. A. *Macromolecules* **1990**, *23* (3), 890–893.

(17) Wu, S. *J. Phys. Chem.* **1970**, *74* (3), 632–638.

(18) Segal-Peretz, T.; Zhou, C.; Ren, J.; Dazai, T.; Ocola, L. E.; Divan, R. N. S.; Nealey, P. F. *J. Photopolym. Sci. Technol.* **2016**, *29* (5), 653–657.

(19) Pathangi, H.; Vaid, V.; Chan, B. T.; Vandenbroeck, N.; Li, J.; Hong, S. E.; Cao, Y.; Durairaj, B.; Lin, G.; Somervell, M.; Kitano, T.; Harukawa, R.; Sah, K.; Cross, A.; Bayana, H.; D'Urzo, L.; Gronheid, R. *Proc. SPIE* **2016**, *9777*, 97770G.

Chapter 4: Understanding the Formation and Annihilation of Dislocations in Chemo-Epitaxy Directed Self-Assembly

4.1 Abstract

Directed self-assembly (DSA) of block copolymers (BCP) can achieve semiconductor relevant structures at very low cost, and thus has attracted considerate interest from the industry. However, the self-assembling structures can become kinetically trapped into defective states, which greatly impacts the implementation of DSA. Understanding the kinetics of defect formation and annihilation is crucial to further optimizing the alignment process and reducing defect density. Such kinetic experiments, however, are not commonly available in academic laboratories, limiting the understanding of kinetic process at the late stage of the DSA process. To address this challenge, we perform kinetic study of chemo-epitaxy DSA in the 300 mm wafer fab, where the complete defectivity information on a full wafer can be readily captured. Through extensive statistical analysis of the defect information collected at different time, we reveal the physical model of defect annihilation for the first time. The annihilation kinetics can be well described by a power law model, indicating that all defects can be removed by sufficiently long annealing time. We further develop image analysis algorithms to analyze the distribution of size and configuration of the defects, and discover that the distribution stays relatively constant over time. The configuration distribution is determined by the role of guiding stripe, which is found to stabilize the defects. Though these findings are based on polystyrene-*b*-poly(methyl methacrylate) (PS-*b*-PMMA), which is the only available material platform for such a fundamental investigation, we anticipate that these results can be readily applied to other BCP platforms as well.

4.2 Introduction

Directed self-assembly (DSA) of block copolymers (BCPs) has attracted considerate interest from both academia and industry due to its potential to fabricate relevant structures for semiconductor applications at relatively low cost.[1–3] DSA utilizes lithographically defined template, with chemical or topographical contrast, to direct BCPs to self-assemble into semiconductor relevant features such as line/space or contact holes.[4] A major advantage of DSA is that it can multiply the lithographical features of the template without any additional lithography or etching steps, which significantly decreases the process cost.[5] DSA-based fin field-effect transistor (FinFET) devices down to 7 nm node have been demonstrated with low cost and low process complexity, and showed comparable device performance with self-aligned multiple patterning, which remains the prevalent approach in high volume manufacturing (HVM).[6,7] With all the benefits of DSA, however, it is still restricted in HVM due to its higher defectivity than industrial target, which typically requires less than 1 defect per 100 cm^2.

Despite the great progress of DSA, fundamental understanding of the defectivity remains limited since the necessary inspection tools are not commonly available in academic laboratories. Statistical analysis of defectivity only became possible a few years ago when DSA was implemented on the 300 mm wafer processing line at imec.[8] For the first time, defectivity in DSA could be quantified and various parameters have been extensively optimized, such as pattern pitch, guiding stripe width, template topography, background chemistry and annealing conditions.[9–12] These efforts have led to significant reduction in defectivity, approaching that required by HVM.

These studies, however, were mainly based on structures at long annealing time close to thermodynamic equilibrium, whereas recent simulation studies have revealed that defects are kinetically trapped metastable structures rather than equilibrium structures.[13,14] Though defects

possess much higher free energies than defect-free structures, they can be kinetically trapped by the energy barriers along the annihilation pathway and persist for a long time during annealing. As a result, to understand kinetics of DSA, in addition to thermodynamics, is also critical to revealing the mechanism of defect formation and further reducing defectivity in DSA.

Previous kinetic studies have used ex situ imaging of arrested structures, in situ grazing-incidence small-angle X- ray scattering (GISAXS) and in situ atomic force microscopy (AFM) to investigate evolution of BCP structures during annealing. Ex situ imaging reveals local events of BCP alignment with either two-dimensional or three-dimensional visualization, and has been extensively used to optimize process conditions.[15,16] In situ GISAXS reflects the global morphological change of thin film, and can be extremely useful for understanding the phase behavior of BCPs during annealing.[17,18] In situ AFM is able to track pattern evolution in real time and enables direct visualization of defect annihilation at early stage of DSA.[19] Though these techniques provide valuable insight into the mechanism of defect formation and annihilation, they typically focus on early stage of DSA, when the defect density is high enough to be captured in a typical image. However, a reliable way to understand kinetics at late stage of DSA remains elusive, even though this stage is the most relevant to technological applications.

To address this challenge, we investigate kinetics of defect annihilation at late stage of DSA using state-of-the-art optical inspections tools coupled with scanning electron microscopy (SEM) imaging. Optical inspection tool is able to scan the whole 300 mm wafer and identify the defects based on their distinct optical response compared with aligned structures. The coordinate of each defect can be automatically stored and communicated to SEM, so that SEM images of selected defects can be captured. Optical inspection tracks the global change of defect density with annealing time, whereas the coupled SEM imaging enables analysis of individual defect structures.

We find that the evolution of defect density can be well fitted with power law model, indicating that it is possible to remove all defects with sufficiently long annealing time. Image processing algorithms have been developed to further analyze the distribution of spacing and configurations of defects. After analyzing thousands of SEM images, we find the distribution of spacing and configurations follows a certain pattern. We then perform a probability analysis of the configuration distribution, and obtain the probability of observing a certain dislocation edge based on its relative position with respect to the chemical pattern, which is critical to understanding the mechanism of defect formation and annihilation.

4.3 Experimental

4.3.1 Materials

Cross-linkable polystyrene (xPS, NLD-128) and hydroxyl-terminated polystyrene-random-poly(methyl methacrylate) (PS-*r*-PMMA-OH, NLD-127) were provided by EMD Performance Materials. ArF immersion photoresist AIM5484 was provided by JSR Micro. Organic solvent RER600 was purchased from Fujifilm and Orgasolv STR 301 was purchased from BASF.

4.3.2 Process

The DSA process is based on previously reported chemo-epitaxy DSA flow on 300 mm wafer process line at IMEC.[8,9,20] Briefly, a 13 nm SiN anti-refractive layer was deposited on the 300 mm silicon wafer, followed by spin-coating and annealing of 8 nm xPS at 315°C for 5 min in a nitrogen atmosphere. The wafers were then coated with photo resist and exposed on ASML NXT 1970Ci (NA= 1.35, σ_o=0.87, σ_i=0.72) to form line space pattern with 84 nm full pitch, which was subsequently etched into the xPS layer. The line width of xPS was trimmed to 21 nm on Lam E5 using oxygen-containing plasma. Line width of xPS guiding stripes was confirmed on Hitachi CD-

SEM CG5000 before removing the remaining photoresist by Orgasolv STR 301. PS-*r*-PMMA-OH brush was spin-coated and annealed at 250℃ for 5 min in a nitrogen atmosphere. Extra brush was rinsed with RER600, leaving a 6 nm thick brush layer between the xPS guiding stripes. PS-*b*-PMMA was then coated on the chemical pattern and annealed in nitrogen atmosphere. Coating of xPS, PS-*r*-PMMA brush and PS-*b*-PMMA was performed on TEL CLEAN TRACK™ LITHIUS Pro™ Zi, and all other coating and annealing were performed on TEL CLEAN TRACK™ ACT™12.

4.3.3 Defect inspection

The DSA pattern was transferred to the underlying substrates using plasma etching, followed by defect inspection on KLA-Tencor 2825 and eDR-7110. The 13 nm SiN layer provided effective reflectivity for optical inspection, which provided location of defects as well as a rough classification of defect types. Optical inspection was conducted on 300 mm full wafer with a total inspection area of 46 cm^2 to obtain sufficient statistics and to minimize random errors. The rough classification from optical inspection was then corrected by SEM review to obtain a more accurate classification. After optical inspection and SEM review, density of each defect type could be readily calculated. High sensitivity was employed for optical inspection to ensure that all of the relevant defects could be captured.

4.4 Results and Discussion

The chemo-epitaxy DSA process, known as Liu-Nealey (LiNe) flow, has been implemented on 300 mm wafer processing line at imec and the scheme is shown in Figure 4.1. The substrate is first coated with crosslinked polystyrene (xPS) mat and photoresist, followed by immersion lithography to create the line space patterns. The pattern is then transferred to the underlying xPS and xPS guiding stipes are trimmed to the desired width using plasma etching.

After the resist is stripped, PS-*r*-PMMA brush is grafted on the substrate between the xPS guiding stripes to create the chemical patterns. PS-*b*-PMMA is then coated on the chemical patterns and thermally annealed to self-assemble into the DSA pattern. The optimized conditions serve as the basis of this kinetic study. The period of the chemical pattern (L_S = 84 nm) is three times of the period of BCP (L_0 = 28 nm), and the width of guiding stripe is 0.75 L_0, which were found favorable for fast alignment and low defectivity.[10] In order to capture the kinetic behavior of defect annihilation, the BCP film is annealed for different time and defectivity data is collected for each time. To collect the defectivity data, the assembled DSA pattern is transferred to the underlying SiN layer, which provides effective reflectivity for optical defect inspection and ensures that all relevant defects could be detected. After optical inspection and SEM review, density of each defect type could be calculated.

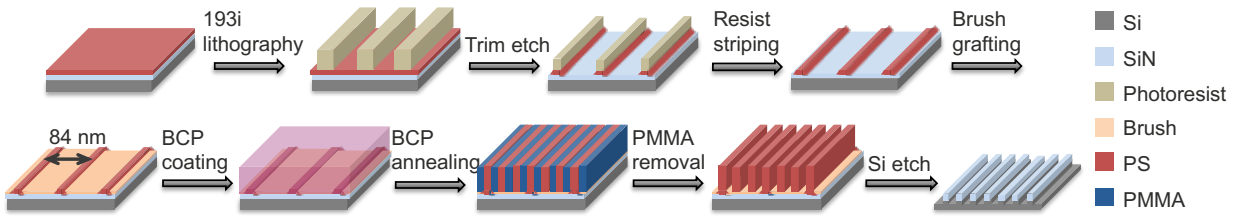

Figure 4.1 Schematic of chemo-epitaxy DSA process (LiNe flow). Crosslinked polystyrene mat was patterned and trimmed, followed by grafting of random polymer brush to form chemical pattern. Block copolymer was coated on the chemical pattern and annealed to form DSA pattern, which was transferred to the underlying substrates via etching.

In this study, we mainly focus on dislocation, which is a DSA specific defect and can only be annihilated by annealing (Figure 4.2b). Dislocation can have different spacing and configurations. Spacing is defined as the number of periods (L_0) between the two dislocation edges, and configuration is defined as the relative position of dislocation with respect to the chemical pattern. There are three major questions we would like to answer in this study: (1) how dislocation density changes with annealing time, (2) how dislocations distribute over different spacing, and

(3) how dislocations distribute over different configurations. Since optical inspection and SEM review can only provide answer to the first question, we have developed image processing algorithms in Matlab to distinguish different spacing and configurations to answer the last two questions. These fundamental understandings are expected to provide insight on the mechanism of dislocation formation and annihilation, as well as valuable guidance on further defect reduction in DSA.

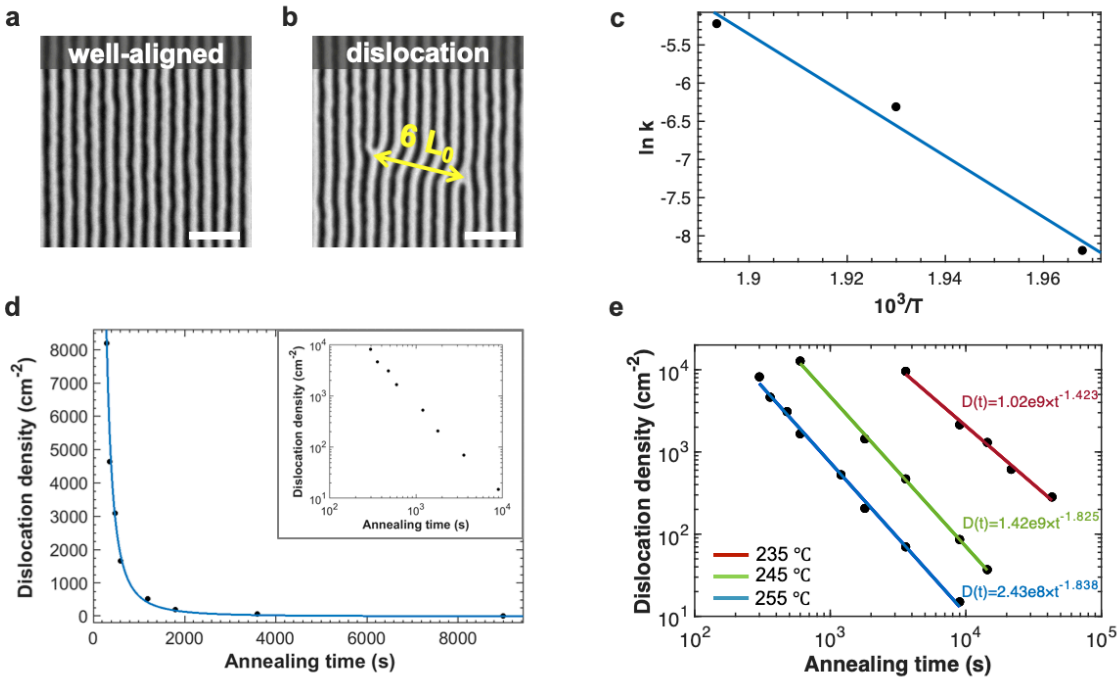

Figure 4.2 (a) Dislocations with various spacing can occur during DSA, and the energy barrier of dislocation annihilation can be estimated using an (b) Arrhenius plot. The estimated apparent energy barrier is approximately 77 k_BT. (c) Kinetics of dislocation annihilation can be fitted with power law model. (e) The exponent of the power law model decreases significantly below a certain temperature, which could result from change in L_0 and the associated pattern incommensurability.

To answer the first question – how dislocations change with annealing time, we collect dislocation density at different annealing time and calculate the energy barrier from the collected data. Simulation studies have shown that dislocation annihilation could have a major energy barrier depending on χN,[21] which is expected to result in single exponential decay $D(t) = D_0 e^{-kt}$, where

$D(t)$ is dislocation density at time t and D_0 is initial dislocation density. k is rate constant determined by the energy barrier ΔF_b: $k = Ae^{-\Delta F_b/k_BT}$. Arrhenius equation allows us to read the energy barrier from the slope by plotting $\ln k$ versus $1/T$ (Figure 4.2c). The estimated energy barrier from this curve is 77 k_BT and, as far as we know, it is the first experimentally calculated energy barrier of dislocation annihilation. It is also on the same order of magnitude as the simulation prediction for dislocations separated by multiple periods, providing valuable information for further simulation studies.[22] This value, however, reflected only the average effective energy barrier of the annihilation process, and does not suggest a single energy barrier.

In fact, multiple energy barriers have been found to be associate with defect annihilation in DSA,[13,14,22] which could account for the power law kinetics we observed in Figure 4.2d. Power law model is an empirical model to describe kinetic process involving a distribution of multiple energy barriers, [23] and has been found to be a better fit of the our data than single exponential decay. Nevertheless, single exponential decay is still a valid way to estimate the average effective energy barrier, which can be challenging to obtain from power law model. Interestingly, it has been shown that grain coarsening of lamellae-forming and cylinder-forming BCPs also follows power-law dynamics, and the exponent is independent of temperature. [24–28] We expect the grain coarsening dynamics also play a role in defect annihilation in DSA and, to better understand the mechanism of annihilation, we compare the exponent (b) of the power law kinetics at different temperatures (Figure 4.2e). It turns out that the exponents are very similar at 245℃ and 255℃, but become much lower at 235℃. The similar exponents at 245℃ and 255℃ could be analogized to grain coarsening dynamics, where the influence of temperature is embedded in the prefactor of the power law model.[26] The smaller exponent at 235℃ could be potentially attributed to the incommensurability of the template pitch (L_S) and natural period of block copolymer (L_0). Previous

study revealed that minimal energy barrier occurs at L_S that is slightly smaller than the commensurate width of L_0, and increasing incommensurability would increase energy barrier.[21] In our study, L_S has been optimized at 255°C and remains constant, whereas L_0 could change with temperature due to change in Flory-Huggins parameter,[29] which could cause incommensurability when temperature sufficiently deviates from 255°C. Experimental measurements revealed a 0.28 nm increase in L_0 from 255°C to 235℃, corresponding to 0.84 nm difference in L_S for 3× DSA, which could cause considerate increase in energy barrier and thus slower kinetics (smaller exponent).

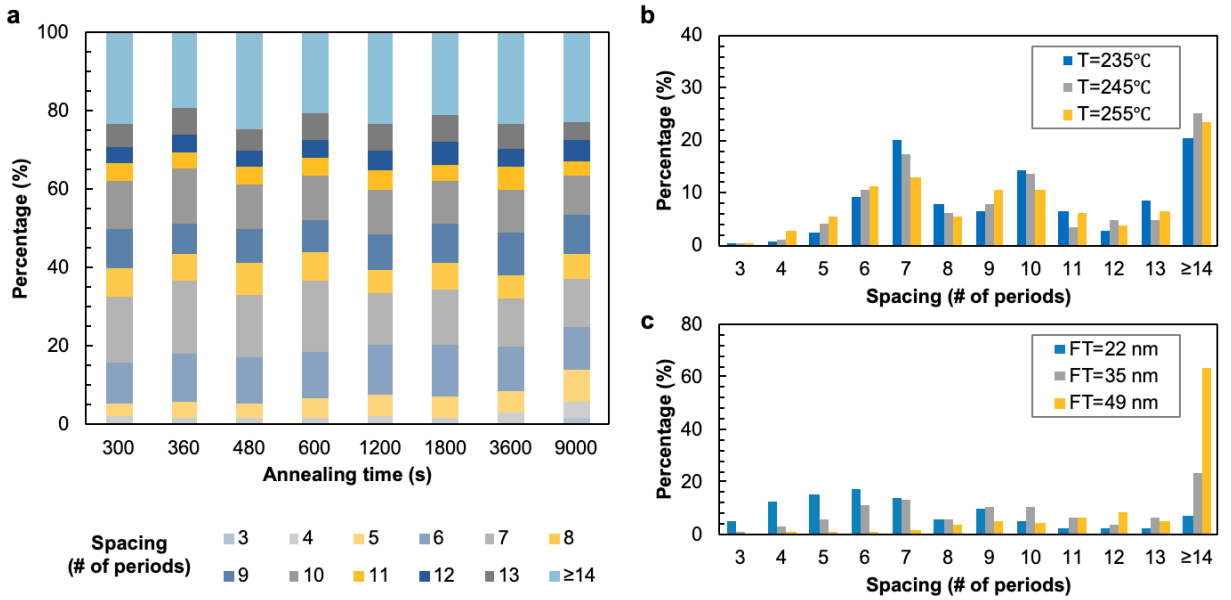

Figure 4.3 (a) Distribution of dislocation spacing stays relatively constant over time, indicating that dislocations with different spacings annihilate at a similar rate. (b) The distribution of spacing is barely affected by annealing temperature, (c) but greatly depends on film thickness. Dislocations tend to have larger spacing at thicker film.

In addition to the overall kinetics, it is also important to understand how dislocations are distributed over different spacing and how the distribution evolves with annealing time. Spacing is defined as the number of disconnected PS lines between the two dislocation edges, and can range

from a few periods to a few dozen periods. Figure 4.2b shows an example of dislocation with a spacing of 6 periods.

If certain spacings annihilate much slower than others, it could have a devastating impact on the implementation of DSA, because such dislocations might never be annihilated. To understand if this is the case, we develop image processing algorithm in Matlab to extract the spacing from thousands of SEM images and obtain the distribution in Fig 3a. The distribution of spacing remains relatively constant over time, indicating that different spacing annihilates at a similar rate. There are two possible explanations of this observation. It is possible that dislocations only need to overcome initial energy barriers to start the annihilation, and the annihilation would happen very fast once started. As a result, the annihilation rate would be hardly dependent on the spacing. Alternatively, it is also possible that the dislocations annihilate gradually and the spacing gradually decreases to smaller spacing before finally diminishes. For a certain spacing, two aspects contribute to its density change with time— decrease in density due to its own annihilation, and increase in density due to annihilation of dislocations with larger spacing. Though the total density decreases with time, the apparent percentage of each spacing could remain relatively constant. Nevertheless, the stable distribution indicates that dislocation annihilation follows the same mechanism despite of the spacing, and it is possible to eliminate all dislocations with sufficiently long annealing time.

We further examine the effect of annealing temperature and film thickness on the distribution of spacing. The annealing temperature has only weak impact on the distribution, and the distribution hardly changes with temperature (Figure 4.3b). This is not surprising since temperature is mainly expected to affect the polymer mobility and overall kinetics, whereas the distribution of energy barriers or ordering mechanism is hardly dependent on the temperature. Film

thickness, on the other hand, has a significant impact on the spacing distribution. The distribution clearly shifts toward larger spacing as the film thickness increases (Figure 4.3c), which could result from the ordering mechanism of DSA. In thin film, the assembly is cooperative throughout the film and mainly driven by the chemical pattern. In thicker film, however, both top free surface and interface at chemical pattern can play a role in the assembly. Previous study revealed that the nucleation of grains is independent at the free surface of the film and near the chemically patterned surface.[30] At the free surface, grains tend to adopt random orientation due to lack of guiding, whereas the assembly near the chemical pattern is well aligned with the guiding stripe. The random orientation at top grow downward, and the ordered grains at bottom propagate upward. After the grains of both interfaces meet in the middle of the film, the random grains at the surface begin to align with the underlying chemical pattern driven by thermodynamic force. In consideration of our observation that dislocation has larger spacing for thicker film, it could come from the fact that random nucleation at free surface plays an increasingly important role in the ordering as the film thickness increases. Indeed, we observe more random grains at thicker film from the defect inspection, which could evolve into dislocations with relatively larger spacing.

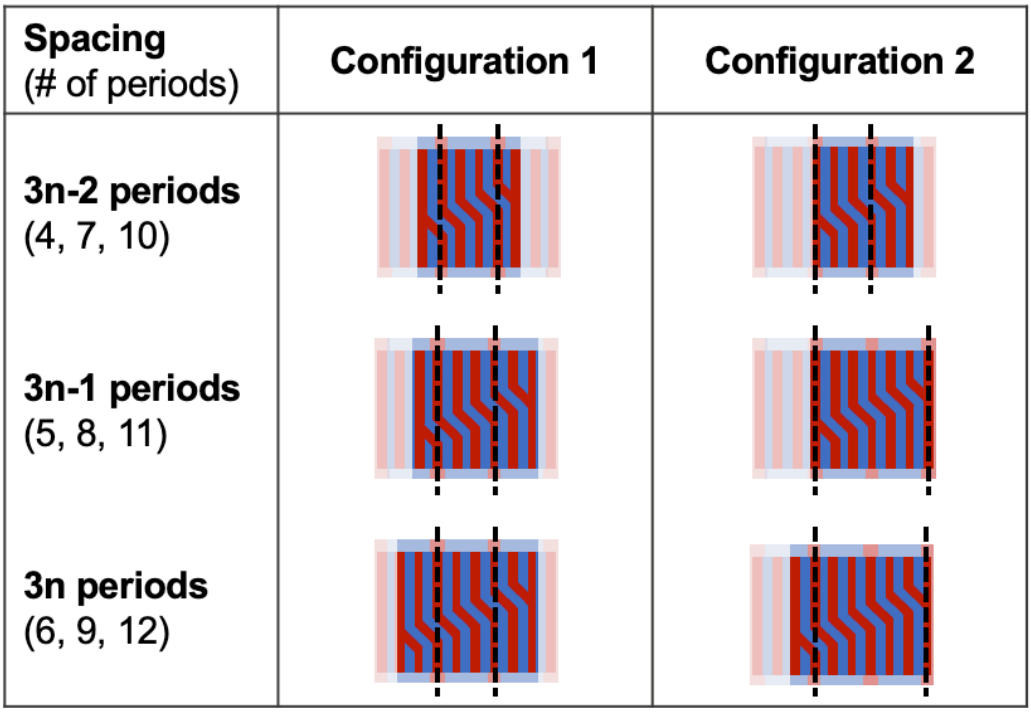

Figure 4.4 Dislocations are divided into 3 groups based on the spacings— 3n-2, 3n-1 and 3n periods—and each group has two possible configurations. Areas without defects are shaded to highlight the dislocation areas, and underlying guiding stripes are marked by black dashed lines. If both dislocation edges are on the brush region, the configuration is defined as Configuration 1. Otherwise it is called Configuration 2.

It is also worth noting that the distribution is not equal for all spacings but follows a clear pattern—dislocations with spacing of 7 or 10 periods seem to outnumber others. Since the factor of density multiplication is 3, which is also the difference between 10 and 7, this distribution pattern cannot be a coincidence. We expect this pattern to be a result of dislocation configuration, which is defined as the relative position of dislocation edge with respect to the chemical pattern. Since the configuration is repeated every 3 periods, we divide all dislocations into 3 groups based on their spacings—3n-2 periods, 3n-1 periods and 3n periods ($n \geqslant 2$). We focus on spacings between 4 and 12 periods, which account for ~ 80% of all dislocations, and each group contains 3 different spacings. For example, the group of 3n-2 periods includes 4, 7 and 10 periods. For each

group, there are two possible configurations: if both dislocation edges are on the brush region, it is defined as "configuration 1", otherwise it is called "configuration 2". Note that this is an artificial definition of configurations for the purpose of a quantitative analysis, and other definitions are also possible. Nevertheless, the conclusion, shown later in this paper, should be valid in spite of different ways to define.

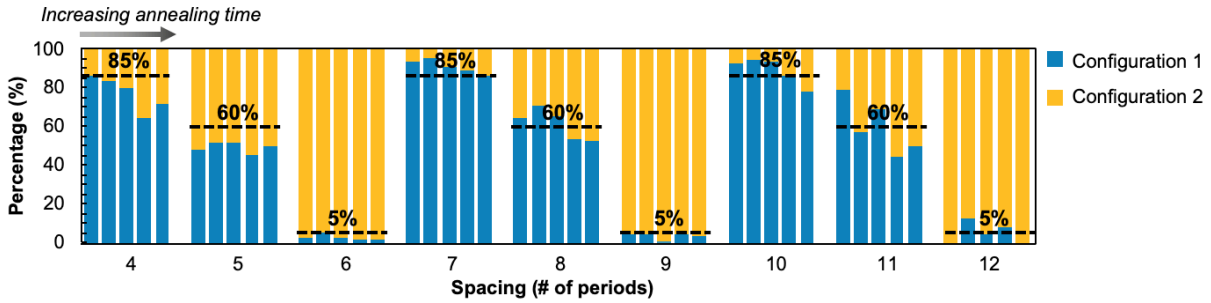

Figure 4.5 Summary of configuration distribution for each spacing. Distribution is stable over time and repeated every 3 periods.

After analyzing over 1000 randomly selected dislocations in Matlab, the distribution of configurations is summarized in Figure 4.5. It is obvious that the distribution is repeated every 3 periods—configuration 1 makes up approximately 85% of the total dislocations for spacings of 3n-2 periods, 60% for 3n-1 periods, and only 5% for 3n periods. We expect this distribution to be determined by the relative position of the dislocation edge with respect to the guiding stripe, which may cause difference in free energies among different configurations and thus different probability of observation.

a

	on guiding stripe	1 period from guiding stripe	2 periods from guiding stripe
Probability of observing a certain dislocation edge	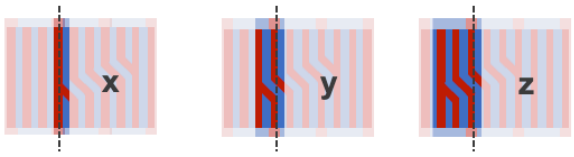		

b

Spacing (# of periods)	**Configuration 1**	**Configuration 2**
3n-2 periods (4, 7, 10)	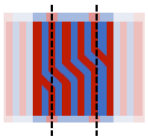 y^2	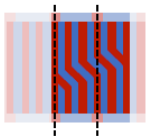 2xz
3n-1 periods (5, 8, 11)	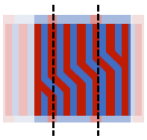 2yz	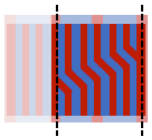 x^2
3n periods (6, 9, 12)	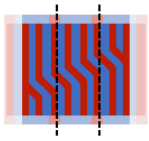 z^2	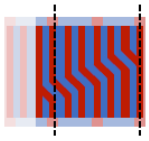 2xy

Figure 4.6 (a) Probability of observing a certain dislocation edge based on its relative position with respect to the guiding stripe. (b) Dislocations can be divided into 3 groups based on spacings, and each group has 2 possible configurations. The probability of each configuration can be represented by a combination of x, y and z.

To further understand the probability of configuration, we calculate the probability of observing a certain dislocation edge depending on its relative distance from the guiding stripe. For a certain dislocation edge, it has three possible positions: (1) when it lies on the guiding stripe, the probability of observing it is defined as *x*, (2) when it is 1 period away from the guiding stripe, the probability is defined as y, (2) when it is 2 periods away from the guiding stripe, the probability is *z* (Figure 4.6a). We can further use x, y and z to represent the probability of observing a certain dislocation configuration. Take configuration 1 of 3n-2 periods as an example, both dislocation

edges are 1 period away from the guiding stripe, and thus the probability of observing each edge is y. The probability of observing configuration 1 is the product of the probabilities to observe the two edges, and equals to y^2. For configuration 2, one dislocation edge is on guiding stripe (x) and the other is 2 periods away from guiding (z), giving a probability of xz. This probability also needs to be doubled because this configuration is not symmetric, and thus the probability of observing configuration 2 is 2xz. We can readily write down the probabilities of all other configurations following the same rule and the results are summarize in Figure 4.6b. Note that we assume the probabilities of two dislocations edges are independent of each other, which is supported by previous simulation study showing that the interactions between two dislocation edges become negligible when spacing is beyond 3 periods.[22]

We can further calculate the value of x, y and z by plugging in the percentage of configurations (Figure 4.5) and get the following equation set: $x + y + z = 1$, $\frac{y^2}{y^2+2xz} = 0.85$, $\frac{2yz}{2yz+x^2} = 0.6$, $\frac{z^2}{z^2+2xy} = 0.05$. By solving this equation set, we can determine the value of x, y and z to be 0.3, 0.6 and 0.1 respectively. In other words, it is most likely to observe a dislocation edge 1 period away from the guiding stripe, and least likely to observe it when it is 2 periods away from the guiding stripe.

To verify our probability analysis, we calculate the percentage of each spacing group using the value of x, y and z, and compare with the experimental data. The percentage of each spacing group is simply the sum of the probabilities of configuration 1 and 2—the percentage of 3n-2 periods is $y^2 + 2xz = 0.42$, that of 3n-1 periods is $2yz + x^2 = 0.21$, and the probability to observe 3n periods is $z^2 + 2xy = 0.37$. We further collect the percentage of each spacing group at different annealing time, and compare them with these calculated values (Figure 4.7). They are

in surprisingly good agreement, further validating our probability analysis. Note that the configuration distribution and spacing distribution are two independent data sets collected from experiments, and they can both be well represented by the calculated probabilities, which is very strong support of our analysis.

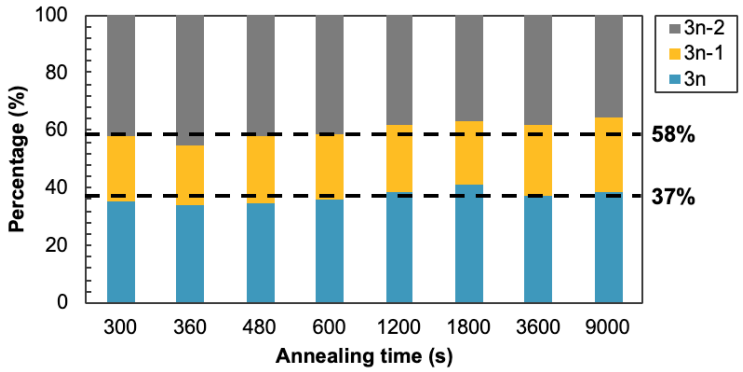

Figure 4.7 Experimentally measured distribution of spacing agrees well with calculated probabilities (black dashed lines).

Based on the probability analysis above, surprisingly, guiding stripe seems to stabilize the dislocations. The annihilation is expected to start from the first disconnected domain next to the dislocation edge, which is most likely to occur on top of the guiding stripe. It is contrary to our intuitive expectation that guiding stripe would facilitate annihilation and disfavor disconnected domain. This observation could be potentially attributed to the chemistry and topography of the chemical pattern. For example, it is possible that the disconnected domain could help to form a flat film since guiding stripe is slightly higher than the brush region. A deeper understanding of this phenomena, however, would require simulation studies and is currently ongoing.

4.5 Conclusions

In summary, we conducted detailed statistical analysis of the dislocation annihilation kinetics in chemo-epitaxy DSA. The time evolution of dislocation density could be well described by a power law model, and the apparent energy barrier could be estimated using exponential

approximation. Experimentally calculated energy barrier provided valuable guidance for the simulation study, and facilitated the understanding of the mechanism of defect formation and annihilation. We also found that the distribution of spacing and configuration stayed relatively constant over time, and their percentage was determined by the role of guiding stripe. Contrary to what one would intuitively expect, guiding stripes actually stabilizes the dislocations. With these new findings of the DSA kinetics, it is possible to further optimize the process and ultimately eliminate the defects in DSA.

4.6 References

(1) Darling, S. B. *Prog. Polym. Sci.* **2007**, *32* (10), 1152–1204.

(2) Jeong, S.-J.; Kim, J. Y.; Kim, B. H.; Moon, H.-S.; Kim, S. O. *Mater. Today* **2013**, *16* (12), 468–476.

(3) Ji, S.; Wan, L.; Liu, C.-C.; Nealey, P. F. *Prog. Polym. Sci.* **2016**, *54–55*, 76–127.

(4) Kim, S. O.; Solak, H. H.; Stoykovich, M. P.; Ferrier, N. J.; De Pablo, J. J.; Nealey, P. F. *Nature* **2003**, *424* (6947), 411–414.

(5) Ruiz, R.; Kang, H.; Detcheverry, F. A.; Dobisz, E.; Kercher, D. S.; Albrecht, T. R.; de Pablo, J. J.; Nealey, P. F. *Science* **2008**, *321* (5891), 936–939.

(6) Tsai, H.; Pitera, J. W.; Miyazoe, H.; Bangsaruntip, S.; Engelmann, S. U.; Liu, C.-C.; Cheng, J. Y.; Bucchignano, J. J.; Klaus, D. P.; Joseph, E. A.; Sanders, D. P.; Colburn, M. E.; Guillorn, M. A. *ACS Nano* **2014**, *8* (5), 5227–5232.

(7) Liu, C.; Franke, E.; Mignot, Y.; Xie, R.; Yeung, C. W.; Zhang, J.; Chi, C.; Zhang, C.; Farrell, R.; Lai, K.; Tsai, H.; Felix, N.; Corliss, D. *Nat. Electron.* **2018**, *1* (10), 562–569.

(8) Delgadillo, P. A. R.; Gronheid, R.; Thode, C. J.; Wu, H.; Cao, Y.; Neisser, M.; Somervell, M.; Nafus, K.; Nealey, P. F. *J. Micro/Nanolithography, MEMS, MOEMS* **2012**, *11* (3), 031302.

(9) Delgadillo, P. R.; Suri, M.; Durant, S.; Cross, A.; Nagaswami, V. R.; Heuvel, D. Van Den; Gronheid, R.; Nealey, P. *J. Micro/Nanolithography, MEMS, MOEMS* **2013**, *12* (3), 031112.

(10) Garner, G. P.; Rincon Delgadillo, P.; Gronheid, R.; Nealey, P. F.; De Pablo, J. J. *Mol. Syst. Des. Eng.* **2017**, *2* (5), 567–580.

(11) Williamson, L. D.; Seidel, R. N.; Chen, X.; Suh, H. S.; Rincon Delgadillo, P.; Gronheid, R.; Nealey, P. F. *ACS Appl. Mater. Interfaces* **2016**, *8* (4), 2704–2712.

(12) Pathangi, H.; Chan, B. T.; Bayana, H.; Vandenbroeck, N.; Heuvel, D. Van Den; Look, L. Van; Rincon-Delgadillo, P.; Cao, Y.; Kim, J.; Lin, G.; Parnell, D.; Nafus, K.; Harukawa, R.; Chikashi, I.; Polli, M.; D'Urzo, L.; Gronheid, R.; Nealey, P. *J. Micro/Nanolithography, MEMS, MOEMS* **2015**, *14* (3), 031204.

(13) Li, W.; Müller, M. *Macromolecules* **2016**, *49* (16), 6126–6138.

(14) Hur, S.-M.; Thapar, V.; Ramírez-Hernández, A.; Khaira, G.; Segal-Peretz, T.; Rincon-Delgadillo, P. A.; Li, W.; Müller, M.; Nealey, P. F.; de Pablo, J. J. *Proc. Natl. Acad. Sci.* **2015**, *112* (46), 14144–14149.

(15) Ren, J.; Zhou, C.; Chen, X.; Dolejsi, M.; Craig, G. S. W. W.; Rincon Delgadillo, P. A.; Segal-Peretz, T.; Nealey, P. F. *ACS Appl. Mater. Interfaces* **2018**, *10* (27), 23414–23423.

(16) Welander, A. M.; Kang, H.; Stuen, K. O.; Solak, H. H.; Müller, M.; De Pablo, J. J.; Nealey, P. F. *Macromolecules* **2008**, *41* (8), 2759–2761.

(17) Gu, X.; Gunkel, I.; Hexemer, A.; Gu, W.; Russell, T. P. *Adv. Mater.* **2014**, *26* (2), 273–281.

(18) Paik, M. Y.; Bosworth, J. K.; Smilges, D.-M.; Schwartz, E. L.; Andre, X.; Ober, C. K. *Macromolecules* **2010**, *43* (9), 4253–4260.

(19) Raybin, J.; Ren, J.; Chen, X.; Gronheid, R.; Nealey, P. F.; Sibener, S. J. *Nano Lett.* **2017**, *17* (12), 7717–7723.

(20) Gronheid, R.; Rincon Delgadillo, P.; Pathangi, H.; Van den Heuvel, D.; Parnell, D.; Chan, B. T.; Lee, Y.-T.; Van Look, L.; Cao, Y.; Her, Y.; Lin, G.; Harukawa, R.; Nagaswami, V.; D'Urzo, L.; Somervell, M.; Nealey, P. *Proc. SPIE* **2014**, *9049*, 904905.

(21) Takahashi, H.; Laachi, N.; Delaney, K. T.; Hur, S.-M.; Weinheimer, C. J.; Shykind, D.; Fredrickson, G. H. *Macromolecules* **2012**, *45* (15), 6253–6265.

(22) Hur, S.-M.; Thapar, V.; Ramírez-Hernández, A.; Nealey, P. F.; de Pablo, J. J. *ACS Nano* **2018**, *12* (10), 9974–9981.

(23) McNeil, I. J.; Ashford, D. L.; Luo, H.; Fecko, C. J. *J. Phys. Chem. C* **2012**, *116* (30), 15888–15899.

(24) Harrison, C.; Adamson, D. H.; Cheng, Z.; Sebastian, J. M.; Sethuraman, S.; Huse, D. A.; Register, R. A.; Chaikin, P. M. *Science* **2000**, *290* (5496), 1558–1560.

(25) Ji, S.; Liu, C.-C.; Liao, W.; Fenske, A. L.; Craig, G. S. W.; Nealey, P. F. *Macromolecules* **2011**, *44* (11), 4291–4300.

(26) Black, C. T.; Forrey, C.; Yager, K. G. *Soft Matter* **2017**, *13* (18), 3275–3283.

(27) Harrison, C.; Cheng, Z.; Sethuraman, S.; Huse, D. A.; Chaikin, P. M.; Vega, D. A.;

Sebastian, J. M.; Register, R. A.; Adamson, D. H. *Phys. Rev. E - Stat. Physics, Plasmas, Fluids, Relat. Interdiscip. Top.* **2002**, *66* (1), 1–27.

(28) Li, W.; Müller, M. *Annu. Rev. Chem. Biomol. Eng.* **2015**, *6* (1), 187–216.

(29) Russell, T. P.; Hjelm, R. P.; Seeger, P. A. *Macromolecules* **1990**, *23* (3), 890–893.

(30) Welander, A. M.; Craig, G. S. W.; Tada, Y.; Yoshida, H.; Nealey, P. F. *Macromolecules* **2013**, *46* (10), 3915–3921.

Chapter 5: Hierarchical Assembly of Plasmonic Nanoparticle Heterodimer Arrays with Tunable Sub-5 nm Nanogaps

5.1 Abstract

Nanoparticle assemblies have generated intense interest due to their novel optical, electronic, and magnetic properties which open up numerous opportunities in fundamental and applied nanophotonics, -electronics, and -magnetics. However, despite the great scientific and technological potential of these structures, it remains an outstanding challenge to reliably fabricate such assemblies with both nanometer-level structural control and precise spatial arrangements on a macroscopic scale. It is the combination of these two features which is key to realizing nanoparticle assemblies' potential, particular for device applications. To address this issue, we propose a hierarchical assembly approach consisting of both template-particle and particle-particle interactions, whereby the former ensures precise addressability of assemblies on a surface and the latter provides nanometer-level structural control. Template-particle interactions are harnessed *via* chemical pattern directed assembly, and the particle-particle interactions are controlled using DNA directed self-assembly. To demonstrate the potential of this hierarchical assembly approach, we demonstrate the fabrication of a particularly fascinating assembly: the nanoparticle heterodimer, which possesses a surprisingly rich set of plasmonic properties and is a promising candidate to

enable a variety of imaging and sensing applications. Each heterodimer is placed on the surface at pre-determined locations, and the precise control of the nanogaps is confirmed by far-field scattering measurements of individual dimers. We further demonstrate that the gap size can be effectively tuned by varying the DNA length. By correlating measured spectra with finite-difference time-domain (FDTD) simulations, we determine the gap sizes to be 4.2 nm and 5.0 nm—with sub-nm deviation—for the two DNA lengths investigated, one of the best gap uniformities ever demonstrated for surface-bound nanoparticle assemblies. The estimated surface-enhanced Raman scattering (SERS) enhancement factor of these heterodimers is on the order of 10^5-10^6 with high reproducibility and predictable polarization-dependence. This hierarchical fabrication technique—employing both template-particle and particle-particle interactions—constitutes a novel platform for the realization of functional nanoparticle assemblies on surfaces, and thereby creates new opportunities to implement these structures in various applications.

5.2 Introduction

Designing and fabricating functional nanostructures from individual nanoparticle (NP) building blocks is both a foundational activity, and an enduring challenge, for the nanoscience and -technology communities. The ability to successfully and reliably exploit the properties of these structures depends sensitively on the control we can exert upon their morphology and spatial arrangement. Morphological control depends largely upon mediating the thermodynamic interactions between individual building blocks (i.e. particle-particle interactions), whereas modulating the interactions between NPs and surfaces (i.e. template-particle interactions) is crucial to achieving a controlled and pre-determined spatial arrangement of assemblies. Common fabrication approaches rely on only one or the other of these two types of interactions. Nanostructures assembled in solution utilize interactions between low-cost single-crystal colloidal

NPs with tailored composition, size, and shape,[2,3] which allows for well controlled properties of these assemblies. The interparticle spacing of dimers in solution, for example, can easily reach sub-5 nm which, coupled with the tremendous field enhancement in the gap, enables single-molecule level detection.[4–6] However, a reliable way to transfer the assembled structures from solution to surface with full addressability and minimal structural alterations remains elusive, thereby limiting the technological usefulness of such solution-processed structures. On the other hand, a few approaches have been developed to assemble functional nanostructures on lithographically-defined patterns combined with chemical contrast, topographical contrast, and DNA origami,[7–12] enabling the controlled spatial arrangement and addressability of assemblies on a macroscopic length scale. However, in these cases, control over the uniformity and reproducibility of the structures, e.g. the interparticle spacing, is usually insufficient due to the lack of control over interparticle interactions. Consequently, an assembly approach which harnesses both template-particle and particle-particle interactions would represent a considerable advance in nanofabrication and enable access to structures that are otherwise near-inaccessible.

To answer this challenge, we demonstrate a hierarchical assembly approach consisting of chemical pattern directed assembly and DNA directed self-assembly, whereby the former provides control over template-particle interactions and the latter provides control over particle-particle interactions. To demonstrate this robust assembly approach, we fabricate a particularly interesting nanostructure, the nanoparticle heterodimer—two metallic nanoparticles differing in size in close proximity to one another. The surface plasmon resonances of the two nanoparticles can mix and hybridize analogously to molecular orbitals in diatomic molecules.[13,14] This results in a surprisingly rich set of plasmonic properties for such a simple structure, such as electromagnetic field enhancement,[15–17] Fano resonances,[18–20] and the "optical nanodiode" effect,[21,22] enabling a

wide range of potential applications. Despite the great potential of such heterostructures, they are still restricted in applications due to the lack of facile and robust assembly approaches.

Our hierarchical approach comprises two main steps: (1) the fabrication of single-nanoparticle arrays as "seeds" *via* chemical pattern directed assembly, and (2) the "growth" of heterodimers from these seeds *via* DNA-directed self-assembly. The first step provides addressability for each nanostructure, and the second step offers tunable control of the interparticle spacing. The precise placement of each heterodimer enables straightforward optical characterization of individual structures and, therefore, statistical analysis of multiple structures, which in turn enables the determination of the distribution of gap size in combination with FDTD simulations. By comparing heterodimers formed with and without DNA, as well as heterodimers with different DNA lengths, we confirm the essential role of DNA in controlling the gap size. Far-field scattering and surface-enhanced Raman scattering (SERS) measurements of individual heterodimers further reveal their strong plasmonic coupling and potential as robust SERS-active nanostructures. This versatile assembly process, with precise addressability of individual nanostructures on a macroscopic scale and well-controlled structural properties, provides a valuable platform for high-throughput nanomaterials for both fundamental exploration and device implementation.

5.3 Experimental

5.3.1 Fabrication of single AuNP arrays

Silicon ⟨100⟩ wafers were purchased from WRS Materials, LLC. Cross-linkable polystyrene (PS) containing 4% glycidyl methacrylate as a crosslinking agent was synthesized as described previously.[23] Hydroxyl-terminated poly(ethylene glycol) methyl ethers (PEG–OH, Mn = 32000 g/mol) was purchased from Polymer Source, Inc. Poly(methyl methacrylate) (PMMA)

photoresist (950 kg/mol, 4 wt% in chlorobenzene) was purchased from MicroChem, Inc. AuNPs with citrate ligands were purchased from Ted Pella, Inc. 2-propanol (IPA), 4-methyl-2-pentanone (MIBK), chlorobenzene and 1-methyl-2-pyrrolidinone (NMP) were purchased from Aldrich and used as received.

Substrates were spin-coated from a 0.5 wt% solution of cross-linkable PS in toluene, followed by annealing at 190°C under vacuum for 24 hours to form the crosslinked PS (xPS) mat. Diluted PMMA photoresist (1.5 wt% in chlorobenzene) was then spin-coated on top, and electron beam lithography was performed to create desired dot arrays. After resist development with a mixture of MIBK and IPA (1:3 by volume), the patterned substrates were exposed to oxygen plasma (20 W, 30 s) to remove xPS in the patterned areas. The exposed areas were then functionalized with PEG-OH by spin coating from a 1.5 wt% solution in chlorobenzene and annealing at 200°C for 5 min in a nitrogen atmosphere. The remaining photoresist and excess PEG-OH were removed by sonication in NMP (3 min, 2 cycles) and chlorobenzene (3 min, 1 cycle). For adsorption of AuNPs onto patterned areas, 100 μL AuNP suspension was deposited on the substrate and left still for 40 min in a humid environment. The substrates were then rinsed thoroughly with water and dried with nitrogen.

5.3.2 Synthesis of AuNP-DNA conjugates

NAP-5 columns were purchased from GE Healthcare, Inc. 1,4-dithiothreitol (DTT), sodium chloride (NaCl), sodium dodecyl sulfate (SDS), sodium phosphate monobasic and sodium phosphate dibasic were purchased from Aldrich and used as received. All oligonucleotides were purchased from Integrated DNA Technologies, Inc and are sequenced as follows:

ssDNA1: TAA CAA TAA TCC CTC TTT TTT TTT T-SH

(Cy5-TAA CAA TAA TCC CTC TTT TTT TTT T-SH for Raman scattering measurement)

ssDNA2: GAG GGA TTA TTG TTA TTT TTT TTT T-SH

ssDNA3: SH-T TTT TTT TTT TAC TTT TCA AGT ACT CTG TGA

linker DNA: GAG GGA TTA TTG TTA TCA CAG AGT ACT TGA AAA GTA

AuNP-DNA conjugates were synthesized following a thiol-assisted attachment process as reported previously.[24,25] Briefly, ssDNA2 (or ssDNA3) was treated with 0.1 M DTT solution (pH = 8) for 1 hour and desalted using NAP-5 columns. The purified oligonucleotides were mixed with AuNPs solution (approximately 3000 oligonucleotides/AuNP) and mixed for 1 h on a mixer to form an initial loose loading. The surfactant SDS was then added to the mixture to bring the final concentration of SDS to 0.1%, followed by the addition of 500 mM citrate buffer (pH = 3). After bringing the concentration of citrate buffer to 10 mM, the mixture was placed on a mixer for 2 h for further DNA loading. For a "salt aging" process, 2M NaCl solution was slowly added to the mixture over the next 1 h to bring the final concentration of NaCl to 0.3 M and the solution was allowed to mix for another 2 h. The excess oligonucleotides were removed by three rounds of centrifugation (7000 rpm, 15 min each) and the AuNP-DNA conjugates were resuspended in hybridization buffer (0.3 M NaCl, 0.1% SDS, 0.01 M phosphate buffer, pH = 7).

5.3.3 Fabrication of heterodimer arrays

Arrays of single AuNPs were functionalized with ssDNA1 following a similar procedure as used to synthesize AuNP-DNA conjugates. After treatment with DTT and desalting, purified ssDNA1 was dissolved in a solution of 1 M NaCl, 0.1% SDS and 0.01 M phosphate buffer (pH = 7). The final concentration of oligonucleotides was 2 μM. Substrates were functionalized with single AuNP arrays by soaking in the ssDNA1 solution and being placed on a mixer overnight to complete the DNA loading. After loading is complete, substrates were rinsed by 0.3 M NaCl, 0.1% SDS and distilled water, respectively, and dried with nitrogen. For "15 bps" dimers, the substrates

were soaked in solution of AuNP-ssDNA2 conjugates in hybridization buffer (0.3M NaCl, 0.1% SDS, 0.01M phosphate buffer, pH = 7) and placed on a mixer overnight. Following hybridization, the substrates were rinsed with 0.3 M NaCl, 0.1% SDS and distilled water, followed by drying with nitrogen. For "36 bps" dimers, the substrates were first soaked in solution of 2 μM linker DNA in hybridization buffer and mixed for 7 hours to complete hybridization. After rinsing with 0.3 M NaCl, 0.1% SDS and distilled water, the substrates hybridized with AuNP-ssDNA3 conjugates. The assembled structures were imaged by a high-resolution Field-Emission Scanning Electron Microscope (Carl Zeiss Merlin).

5.3.4 Scattering Spectroscopy

Samples were prepared on indium tin oxide (ITO)-coated glass substrates (Structure Probe, Inc) and scattering spectra were measured using a home-built set-up. Prior to scattering measurements, samples were imaged with SEM to determine the direction of the dimer axis. The SEM images were taken at relatively low magnification (15,000×) and short dwell time (6 μs) in a single frame to minimize any potential effect of SEM imaging on the sample. The scattering setup is equipped with a linear polarizer, and the samples were rotated to align the measured dimer axis with the polarization axis of the incident light. A broadband white light source (Fianium, White Lase SC400, 400-2700 nm) was coupled to an inverted optical microscope equipped with an oil immersion objective with numerical aperture NA = 1.4 (Olympus, IX-81; SAPO 100×). The back-scattered images of the sample plane were recorded by a sCMOS array detector (Andor Neo) connected to the eye-piece of the trinocular microscope, and spectra were acquired by an EM-CCD (Andor Newton) connected to an imaging spectrometer (Andor Shamrock 193i) coupled to the side port of the microscope. To minimize the scattering from the coverslip and sample interface, a drop of immersion oil was put on the coverslip, and the inverted sample was placed on top of the

immersion oil. Then the coverslip was put on the microscope for measurement. Background correction and normalization were performed for all measurements.

5.3.5 Raman Scattering

Raman spectra were collected on a Horiba LabRAM HR Evolution Raman spectrometer (Horiba, Ltd.) with 633 nm HeNe laser (77.5 μW) and 100× objective. The Raman spectra were recorded in the range of 800–1800 cm−1 with 1 s acquisition, 2 accumulations. All data were baseline-corrected by subtracting the background spectra.

5.3.6 Numerical Simulations

FDTD calculations were conducted using FDTD Solutions (Lumerical Solutions, Inc.) software. The simulation set-up replicated the experimental set-up of far-field scattering. The environmental refractive index was set as 1.5, corresponding to that of the immersion oil. Gold was simulated using a complex refractive index from Palik et al.[26] and a previously reported model[27] was employed to describe the optical properties of ITO. XPS, PEG brush, and glass were simulated as dielectric materials with real dielectric constants. The spectra were recorded by a frequency-domain field monitor. For simulation of SERS, 633 nm incident light was used instead of broadband white light and the environmental refractive index was set to 1.0 corresponding to that of air.

5.4 Results and discussion

The fabrication scheme for gold nanoparticle (AuNP) heterodimer arrays is shown in Figure 5.1a. Fabrication begins with the positioning of single AuNPs on lithographically-patterned substrates *via* chemical pattern directed assembly. The substrate is first coated with crosslinked polystyrene (xPS) and poly(methyl methacrylate) (PMMA) resist, followed by electron beam lithography and oxygen plasma etching to create the desired patterns. The exposed substrate within

the patterned areas is functionalized with hydroxyl-terminated poly(ethylene glycol) methyl ethers (PEG), and the unpatterned areas are protected by both the PMMA resist and xPS mat. After removing PMMA and excess PEG brush, AuNPs are selectively immobilized within the patterned areas and form single-AuNP arrays with essentially 100% yield (Figure 5.1b), since the citrate ligands of AuNPs can form hydrogen bonds with the PEG whereas the xPS mat provides only minimal adhesion.

To form heterodimer arrays, single-AuNP arrays are functionalized with thiolated single strand DNA1 (ssDNA1) through a thiol attachment process modified from previously reported methods.[24,25] The ssDNA1 can hybridize with the single strand DNA2 (ssDNA2)-functionalized AuNP conjugate and bring it adjacent to the immobilized single AuNP. The ssDNA1 and ssDNA2 are complementary; their sequence can be found in the experimental section. In this experiment, the hybridized double strand DNA (dsDNA) has 15 base pairs (bps), and the assembled dimer is referred to as the "15 bps" dimer. Alternatively, linker ssDNA can be added to increase the length of the hybridized dsDNA to 36 bps, and the dimer assembled with linker is correspondingly referred to as the "36 bps" dimer.

This flexible hierarchical assembly strategy can be readily applied to fabricate heterodimers of various sizes, as shown in Figure 5.1c-e. Indeed, AuNPs with diameters of 40, 60, and 80 nm are all observed to form heterodimers with 50 nm AuNP-DNA conjugates. This fabrication strategy therefore possesses clear advantages over other dimer fabrication methods, many of which require major modifications to the procedure when altering constituent particle size or shape. For example, dimers assembled on DNA origami templates would require different DNA structures to assemble particles of different sizes and shapes, which would be time-consuming and costly to implement. Clearly, the hierarchical assembly strategy demonstrated here requires no

such modifications, and heterodimers of different sizes and shapes can be readily fabricated with little if any alteration to the established procedure.

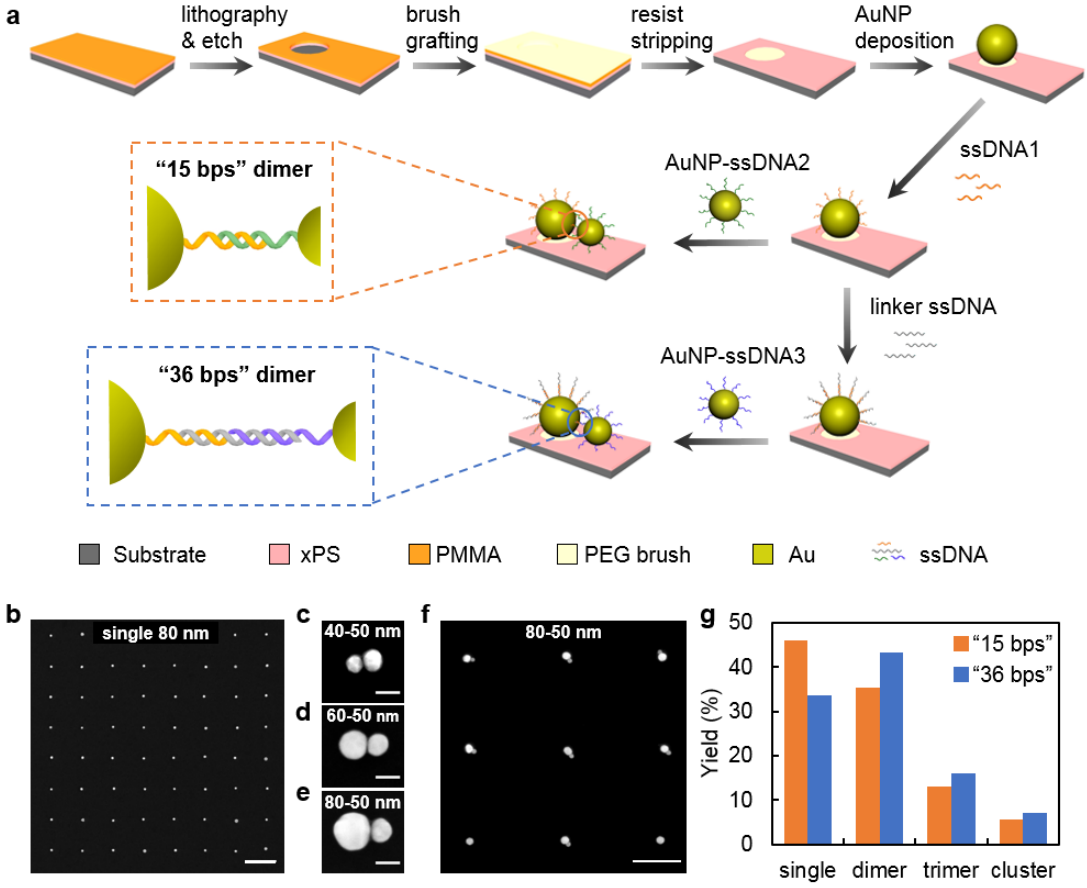

Figure 5.1 Fabrication of AuNP heterodimer arrays. (a) Schematic of the hierarchical assembly of AuNP heterodimers. Following electron beam lithography and oxygen plasma etching, PEG brush is selectively grafted to the substrate within the lithographically-patterned areas; the unpatterned areas are protected by xPS. Single AuNPs are selectively immobilized on the patterned areas due to hydrogen bonding between the citrate-capped AuNPs and the PEG brush. (b) The yield of single-AuNP arrays is essentially 100%. Single-AuNP arrays are then functionalized with ssDNA1. To construct heterodimers, AuNP conjugates functionalized with complementary ssDNA2 then hybridize with the ssDNA1-functionalized AuNPs, bringing the ssDNA2-functionalized AuNPs to an adjacent position. Alternatively, linker ssDNA can be added between the two particles to further alter the length of the hybridized DNA. The hybridized DNA is 15 bps and 36 bps long for heterodimers assembled with and without linker ssDNA, respectively. Larger interparticle spacing is expected for "36 bps" dimers as a result of the longer DNA length. (c)-(e) Heterodimers of 40-50, 60-50, and 80-50 nm sizes can be readily assembled following the hierarchical approach. (g) Dominant structures after assembly are heterodimers and single AuNPs. Scale bars: (b), (f) 500 nm; (c), (d), (e) 50 nm.

We choose 80-50 nm dimers for further characterization (Figure 5.1f), as larger particles present fewer metrology challenges whilst still exhibiting similar plasmonic behavior to smaller particle heterodimers. After primary optimization of the DNA hybridization conditions (e.g. salt concentration and hybridization time), the yield of "15 bps" dimers is estimated to be 35% (based on the analysis of approximately two hundred assemblies), compared with 43% for "36 bps" dimers (Figure 5.1g). We anticipate the higher yield of "36 bps" dimers results from the reduced steric hindrance between the two constituent particles during hybridization. Since dsDNA is much more rigid than ssDNA,[28] after ssDNA1 hybridizes with linker DNA, the hybridized dsDNA is less likely to adhere to the particle surface and increases the distance between the particle surface and the dangling end used for hybridization. As a result, the steric hindrance between the two particles is reduced, which facilitates subsequent hybridization with AuNP-ssDNA2 conjugates. Single nanoparticles are the predominant nanostructures besides dimers. However, they can be readily distinguished from dimers and excluded from subsequent analysis due to their distinctive optical response. We characterize the fabricated heterodimers by collecting their far-field light scattering and SERS spectra, which are very sensitive to the gap size.[29,30]

In order to characterize the gap sizes of nanoparticle heterodimers, we measure the longitudinal plasmon resonance of individual nanostructures. When incident light is polarized along the dimer axis, coupling of the two single-AuNP plasmonic resonances results in a strong red-shift of the resulting dimer longitudinal plasmon resonance. This red-shifted scattering peak is very sensitive to the heterodimer gap size. As a result, a narrow distribution of longitudinal plasmon resonance peak positions is anticipated for a population of heterodimers with well-controlled gap sizes. The dependence of the longitudinal plasmon resonance on gap size can be interpreted using a simple dipole-dipole interaction model.[31] For a single nanoparticle, polarized

incident light induces a distribution of electrons within the particle which, in turn, exerts a repulsive force on the incident field. However, when another particle is nearby (i.e. the case of a heterodimer) and the light is polarized along the dimer axis, the repulsive force associated with each particle is weakened due to the coupling of the two particles, leading to a lower resonance frequency (red shift). As the gap size decreases and the coupling effect becomes stronger, the longitudinal plasmon resonance peak will become further red-shifted.[32] Under perpendicular polarization, on the other hand, the repulsive forces would be enhanced by the coupling, resulting in a slight blue-shifted peak, the transverse plasmon resonance peak. This peak is relatively insensitive to the gap size, and thus is not the focus of our analysis. The far-field scattering spectra of AuNP nanostructures are measured using a custom-built set-up with spatially coherent white laser.

We first measure the scattering spectra of 80 nm diameter single AuNPs functionalized with ssDNA1. Three representative spectra are shown in Figure 5.2b (green solid lines), which agree well with the corresponding simulated spectrum (green dashed line). All spectra are normalized with respect to their maximum intensity for better comparison. The peak position is identified for each measured spectrum and their distribution is shown in Figure 5.2c. The distribution of peak positions is approximately normal with a mean of 561 nm. We also measured the spectra before ssDNA functionalization in order to examine the impact of ssDNA on the optical properties of AuNPs. In this case, the distribution of peak positions is again approximately normally distributed with a mean of 562 nm. The 1 nm difference between the means of the two distributions is clearly within the standard error of the mean—$\mathrm{SD}/\sqrt{N}$, where SD is the standard deviation of peak positions and N is the number of structures measured. This small difference is therefore more likely to result from statistical noise rather than any underlying difference between

the two distributions. This result confirms that ssDNA functionalization only has a minimal, if any, impact on the optical properties of the AuNPs. This is not surprising since ssDNA has a refractive index (n = 1.5-1.6) close to that of the immersion oil (n = 1.515 at 546 nm) used in these measurements.[33]

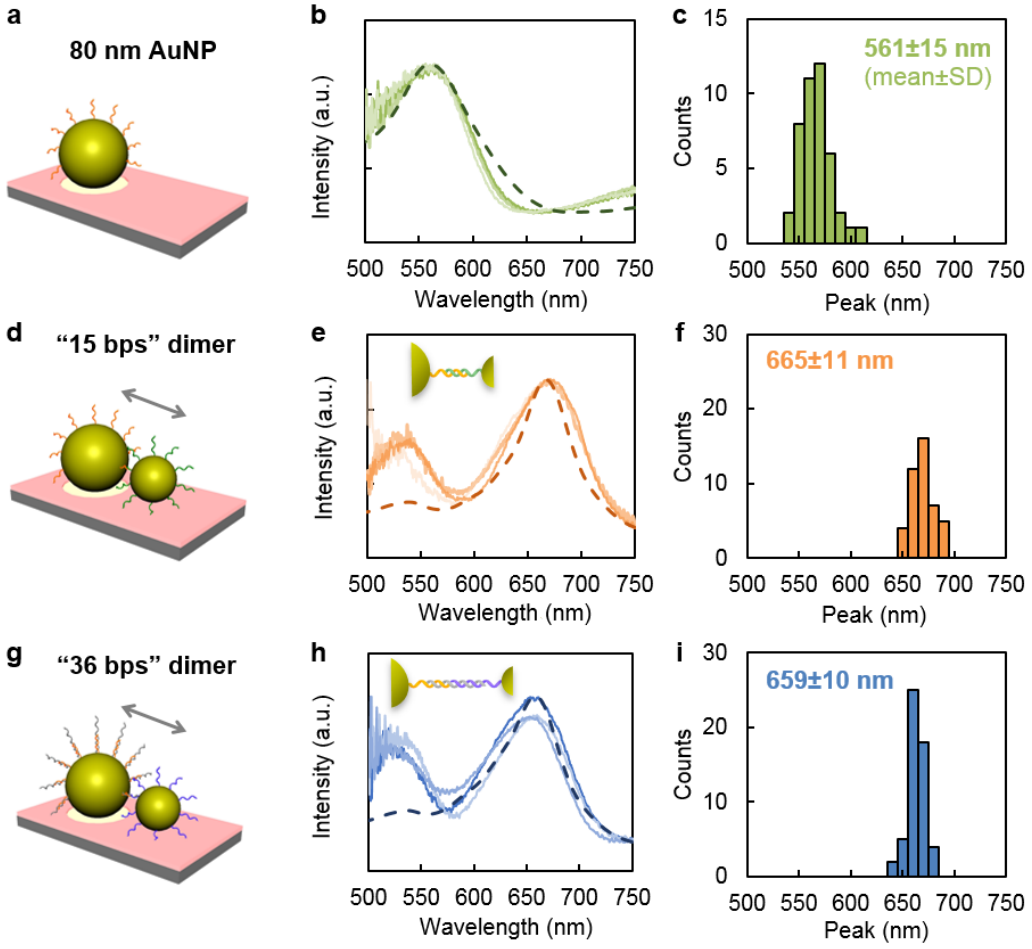

Figure 5.2 Scattering spectra of 80 nm single AuNPs and 80-50 nm heterodimers. (a) Schematic of 80 nm AuNP on the PEG functionalized substrate. (b) Experimentally measured scattering spectra (green solid lines) of 80 nm AuNPs are in good agreement with the simulated spectrum (green dashed line). (c) Experimental distribution of peak positions has a mean of 561 nm and a standard deviation of 15 nm. Scattering spectra of (d) "15 bps" dimers and (g) "36 bps" dimers are measured with incident light polarized along the dimer axis. Representative spectra are shown in (e) and (h) with good reproducibility. The gap size of simulated heterodimers is varied to obtain the best fit between simulated and measured spectra. (f) "15 bps" dimers exhibit a mean peak position of 665±11 nm, and (i) "36 bps" dimers exhibit a less red-shifted mean value of 659±10 nm as obtained from the experimental data.

Individual heterodimers were characterized with incident light polarized along the dimer axis (Figure 5.2d, 5.2g). Representative spectra are shown in Figure 5.2e and Figure 5.2h. The right peak comes from the longitudinal plasmon resonance, whereas the left peak arises from the transverse mode, which arises as the incident light is not perfectly parallel with the dimer axis during measurement. We focus only on the longitudinal plasmon resonance peak in our analysis. Clearly, the longitudinal plasmon resonance is strongly red-shifted compared to the localized surface plasmon resonance of single AuNPs. For "15 bps" dimers, the mean of the experimental distribution of peak positions occurs at 665 nm (Figure 5.2f). For "36 bps" dimers, the DNA linking the two particles is longer and the resulting mean therefore exhibits a smaller red-shift, occurring at 659 nm (Figure 5.2i). We conducted a Welch's t-test in MATLAB to examine if the two distributions of peak positions are significantly different from one another.[34] The test confirms their difference at the 5% significance level. Therefore, the difference in mean peak positions (most likely) arises from a different gap size rather than measurement noise.

In order to estimate the mean gap size—and its likely distribution—from the measured longitudinal plasmon peaks, we calculate the longitudinal resonances of 80-50 nm dimers with various gap sizes using FDTD simulations (Figure 5.3a, 5.3b). Although the fractional plasmon wavelength shift decays exponentially with gap size,[35] the longitudinal plasmon peaks depend approximately linearly on gap size over the narrow distribution of wavelengths measured. Assuming that all variation in the longitudinal plasmon peak positions arises from a variation in gap size, we estimate from the linear fit that the gap size for "15 bps" dimers is 4.2±1.5 nm and that for "36 bps" dimers is 5.0±1.3 nm, which is comparable with previously reported gap size induced by similar length of DNA in a dried state.[4] However, these variations in gap size are necessarily an overestimate as we are ignoring any impact of variation of particle size and shape.

Therefore, for a more accurate estimate, we need to disentangle the impact of particle size and shape from that of gap size. As the impact of particle shape is challenging to simulate, we assume perfectly spherical nanoparticles and examine only the impact of particle size, for which the standard deviation (8%) is provided by the manufacturer.

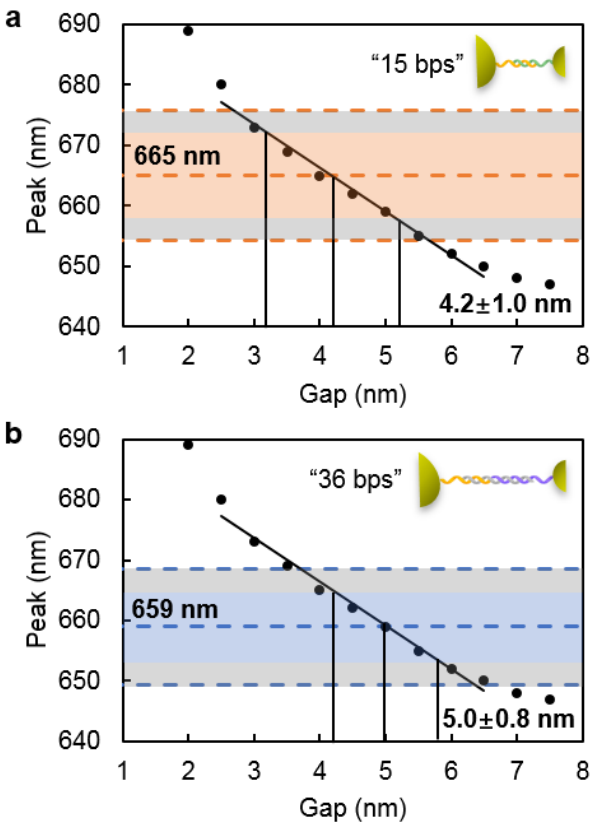

Figure 5.3 Estimation of mean gap size and gap size distribution. Longitudinal plasmon peaks of 80-50 nm dimers with various gap sizes are calculated using FDTD simulations. The dependence of peak position on gap size is approximately linear in the range of measured peak distribution. Experimentally measured mean and standard deviation of the peak distributions are marked by dashed lines. The (a) orange and (b) blue shaded areas indicate the variation in peak distribution attributed to variation in gap size, and the grey shaded areas indicate the variation in peak distribution resulted from variation in particle size. The estimated gap size is 4.2±1.0 nm for "15 bps" dimer and 5.0±0.8 nm for "36 bps" dimer.

We conducted a series of simulations to calculate longitudinal plasmon resonances at various gap size for different dimer radius (sum of individual particle radii), and obtained an

expression for the peak position as a function of gap size and dimer radius. The impact of particle size and gap size on the peak distribution can be disentangled using this function and error propagation rules, and the standard deviation of gap size can be calculated. A detailed calculation procedure is provided in the following.

A series of simulations were conducted to calculate the longitudinal plasmon resonances of the heterodimers at various gap sizes (from 2 nm to 7 nm) for different size of dimers (from 114 nm to 146 nm). The peak position is approximately linear with gap size and dimer size in the range of calculations:

$$P = a_0 + a_1 G + a_2 R, \quad (1)$$

where P is the peak position in nm, G is the gap size in nm, and R is the size (diameter) of the dimer along the major axis. The variables a_0, a_1 and a_2 are fitting parameters. The adjusted R^2 value of the fitted curve is 0.9522, corresponding to $a_0 = 581.3$, $a_1 = -8.074$, and $a_2 = 0.9081$. Based on equation (1) and the error propagation rules[6], the standard deviation of the peak position may be calculated as

$$\sigma^2(P) = {a_1}^2 \sigma^2(G) + {a_2}^2 \sigma^2(R), \quad (2)$$

where $\sigma(G)$ is the standard deviation of the gap size and $\sigma(R)$ is the standard deviation of the dimer diameter.

Since $R = R_1 + R_2$, where $R_1 = 80$ nm, $R_2 = 50$ nm, and the relative standard deviation of particle size is 8% for both 80 nm and 50 nm AuNPs, as provided by manufacturer, $\sigma^2(R)$ is

$$\sigma^2(R) = \sigma^2(R_1) + \sigma^2(R_2) = (80 \times 0.08)^2 + (50 \times 0.08)^2 = 57 \ (\text{nm}^2). \quad (3)$$

Since $\sigma^2(P)$ is measured experimentally, $\sigma(G)$ is the only unknown variable in equation (2). We can therefore estimate the standard deviation of gap size $\sigma(G)$ to be 1.0 nm for "15" bps dimers and 0.8 nm for "36 bps" dimers. Note that the impact of particle shape variation is not

included in this calculation, which would contribute another term to (1) and (2), and lead to an even smaller estimate of deviation of gap size.

Using this procedure, the variation in gap size is found to be significantly smaller than that estimated when ignoring the effect of particle size: the estimated gap size is 4.2±1.0 nm for "15 bps" dimers and 5.0±0.8 nm for "36 bps" dimers, confirming the excellent control over gap distribution using the hierarchical assembly. However, this is again an overestimate of the variation in gap size, as the impact of particle shape has been ignored. Therefore, the true standard deviation of the gap size should lie in the sub-nm regime.

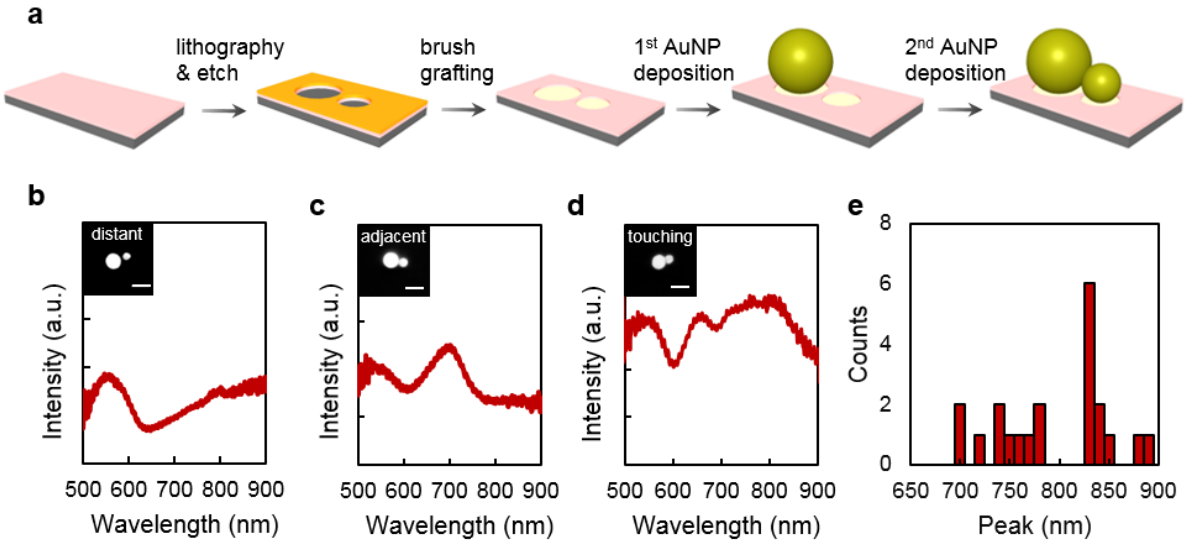

Figure 5.4 Fabrication of 80-50 nm heterodimers without DNA and the corresponding scattering spectra. (a) Schematic of the process for positioning and patterning AuNPs into heterodimers on chemically patterned substrates without DNA. The assembly solely depends on template-particle interactions and the two AuNPs can be (b) distant from, (c) adjacent to or (d) touching each other, giving rise to one, two or three peaks respectively. (e) A broad distribution of rightmost peak positions indicates that the gaps are much less controlled using this approach compared with hierarchical assembly with DNA included.

To further confirm the essential role of particle-particle interaction in controlling the gap size, we compare heterodimers formed with and without DNA. The hierarchical assembly approach, as already demonstrated in this paper, employs both template-particle interaction and

particle-particle interaction (e.g. DNA hybridization). Single nanoparticles are immobilized on a template substrate *via* chemical pattern directed assembly, followed by formation of heterodimers *via* DNA hybridization; the gap size is controlled by the length of the DNA. Alternatively, we can also construct heterodimers based solely on chemical pattern directed assembly without DNA (Figure 5.4a). Two adjacent patterned spots of different sizes are functionalized with the PEG brush, while the unpatterned areas are protected, as before, with xPS. The larger particle is first immobilized on the larger area, as the smaller area cannot provide sufficient adhesion to immobilize the larger particle. The smaller particle is then immobilized on the smaller area, forming a heterodimer. The interparticle spacing of such heterodimers, however, is much less controlled, and the dimers exhibit a far greater variety of far-field scattering spectra than those fabricated with DNA. For example, the two particles can be too distant—and, therefore, behave optically like single AuNPs (Figure 5.4b)—or can be in extremely close proximity such that the coupled longitudinal plasmonic resonance shifts toward the infrared (Figure 5.4d). The long-wavelength longitudinal plasmon scattering peaks of coupled heterodimers span the 700 to 900 nm range (Figure 5.4e), which is much broader distribution of peak positions than that obtained with DNA (Figure 5.2f, 5.2i). The comparison with this control experiment confirms that the interparticle interactions, such as DNA hybridization, are key to controlling the gap size and optical properties of heterodimers.

Following characterization of heterodimers by far-field scattering, we examine their potential as SERS substrates. We first calculate the SERS enhancement factor (EF) of dimers using the gap size previously estimated. The EF is defined as $(E/E_0)^4$ where E is the local maximum electric field within the heterodimer gap and E_0 is the amplitude of the source electric field. For "15 bps" dimers, the estimated gap size is 4.2 nm and the EF is estimated from FDTD simulations

to be 1.4×10^6 (Figure 5.5a). For the "36 bps" dimer with a 5.0 nm gap, the EF is expected to be 6.2×10^5 (Figure 5.5b). Note that the two particles here are not horizontally aligned, such that the incident electric field vector may be decomposed into two orthogonal components, parallel and perpendicular to the dimer center-to-center axis. It is the parallel component which contributes to the SERS enhancement; the perpendicular component has minimal effect. We therefore expect the resulting height difference leads to a slightly lower EF when calculated with respect to the (horizontally aligned) incident electric field as the parallel component of the incident field is necessarily smaller than the total electric field (E_0).

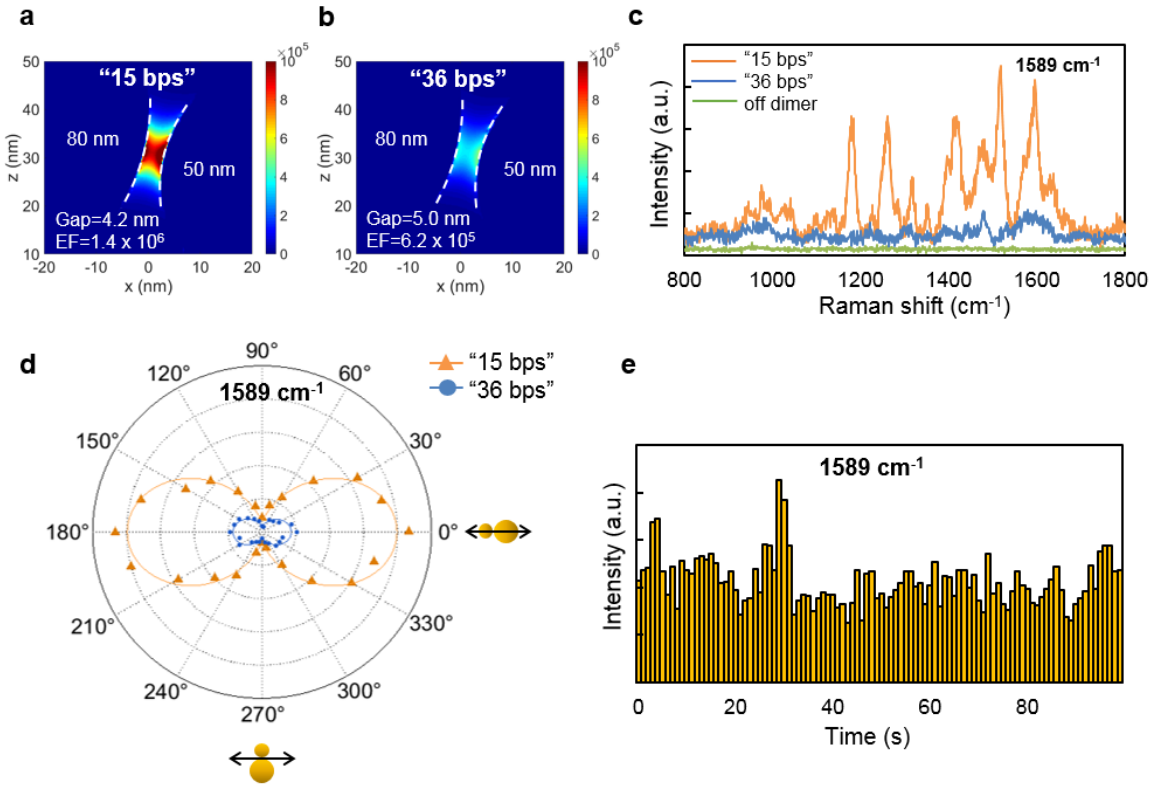

Figure 5.5 SERS measurements of 80-50 nm heterodimers. Simulated SERS enhancement factor of (a) the "15 bps" dimer is approximately 1.4×106 and that of (b) the "36 bps" dimer is 6.2×105. (c) Both heterodimers show enhanced Raman signals of analytes, while no signal is observed from areas away from the dimers ("off dimer"). (d) Polar plots of average SERS intensities taken from five dimers exhibit a strong cos2θ dependence. (e) Time-resolved SERS intensities at 1589 cm-1 (accumulation time 1 s, 100 measurements) remain stable over time.

We conducted SERS measurements on assembled 80-50 nm heterodimers and compared the experimental results with simulations. The ssDNA1 is modified with Cy5 dye to better observe the SERS signals and a 633 nm excitation wavelength is selected as it is resonant with Cy5.[36] A relatively low laser power (77.5 μW) is employed to prevent laser-induced damage to the heterodimers. Repeated acquisition of SERS spectra from the same "15 bps" dimer demonstrates good reproducibility and reveals that there is no significant degradation caused by the laser over time (Figure 5.5e). In order to make a more quantitative comparison, we plotted the averaged Raman intensities of five heterodimers at 1589 cm^{-1} (a characteristic peak of Cy5) for "15 bps" and "36 bps" dimers with the incident laser polarization rotated from 0 to 360° with respect to the dimer axis (Figure 5.5d).[37] When the incident laser is polarized parallel with the dimer axis, the EF of "15 bps" dimers is approximately 4.7 times higher than that of "36 bps" dimers, which is greater than that predicted by simulations. We expect this discrepancy to mainly arise from the different positions the dye molecules adopt in the two types of dimers. Dye molecules are attached to the termini of the ssDNA1 molecules away from the 80 nm AuNPs. For "15 bps" dimers, ssDNA1 directly hybridizes with 50 nm AuNP-ssDNA2 and the dye molecules are close to the surface of the 50 nm AuNPs. For "36 bps" dimers, however, ssDNA1 hybridizes with linker DNA before hybridizing with AuNP-ssDNA3, leaving the dye molecules near the center of the gap. A previous study revealed that the local SERS enhancement at the gap center is smaller than that close to the particle surface[17], an effect that can lead to further exaggerated differences in the EF of the two dimers. The polarization-dependent SERS intensities can be well fitted by $\cos^2\theta$ curves, strongly corroborating the hypothesis that the dominant contribution to the SERS signal is the enhanced electromagnetic field arising from the coupled longitudinal plasmon resonance.[38]

5.5 Conclusions

We have demonstrated a hierarchical assembly approach, combining chemical pattern directed assembly and DNA-directed self-assembly, to fabricate AuNP heterodimer arrays with controlled and tunable sub-5 nm gaps on a macroscopic scale. The precise placement of heterodimers on the functionalized surface enables optical characterization of individual nanostructures, as well as statistical analysis of multiple structures. Far-field scattering of assembled heterodimers reveals strong plasmonic coupling and a distinct red-shift of the longitudinal plasmon resonance compared with single AuNPs. By analyzing scattering spectra and FDTD simulations, we have confirmed that the interparticle spacing is indeed controlled by interparticle interaction, and estimated the gap size to be 4.2 nm and 5.0 nm for the "15 bps" and "36 bps" dimers investigated, respectively. We have also examined the variation of gap size and revealed that the distribution of longitudinal plasmon peaks can be largely attributed to the variation of particle size, while the gap size only has minimal, sub-nm variation. SERS measurements reveals a strongly enhanced electromagnetic field within the heterodimer gap resulting from the coupled plasmon resonance, and the estimated EF is on the order of 10^5-10^6, making the AuNP heterodimer arrays excellent SERS-active nanostructures.

This versatile assembly process has been demonstrated on both silicon wafer and conductive oxide-coated glass, and is expected to be applicable to a wide variety of additional substrates. Furthermore, as this is a post-functionalization approach, where DNA functionalization takes place after the chemical pattern directed assembly, we anticipate that this assembly approach can also be extended to take advantage of other interparticle interactions, such as electrostatic attraction and molecular linkers,[39,40] and could therefore be used to construct even more complex nanostructures, e.g. core-satellite and Au-Ag heterostructures.[41,42] Nanostructure arrays fabricated

from this approach, with nanometer-level structural control and precise addressability, hold great potential for various applications including biosensors,[43,44] photocatalysis,[45–47] and optical information processing.[48]

5.6 References

(1) Li, J.; Deng, T.-S.; Liu, X.; Dolan, J. A.; Scherer, N. F.; Nealey, P. F. *Nano Lett.* **2019**, *19* (7), 4314–4320.

(2) Rogers, W. B.; Shih, W. M.; Manoharan, V. N. *Nat. Rev. Mater.* **2016**, *1* (3), 16008.

(3) Walther, A.; Müller, A. H. E. *Chem. Rev.* **2013**, *113* (7), 5194–5261.

(4) Lim, D.-K. K.; Jeon, K.-S. S.; Kim, H. M.; Nam, J.-M. M.; Suh, Y. D. *Nat. Mater.* **2010**, *9* (1), 60–67.

(5) Lim, D.-K.; Jeon, K.-S.; Hwang, J.-H.; Kim, H.; Kwon, S.; Suh, Y. D.; Nam, J.-M. *Nat. Nanotechnol.* **2011**, *6* (7), 452–460.

(6) Taylor, R. W.; Lee, T. C.; Scherman, O. A.; Esteban, R.; Aizpurua, J.; Huang, F. M.; Baumberg, J. J.; Mahajan, S. *ACS Nano* **2011**, *5* (5), 3878–3887.

(7) Liu, X.; Biswas, S.; Jarrett, J. W.; Poutrina, E.; Urbas, A.; Knappenberger, K. L.; Vaia, R. A.; Nealey, P. F. *Adv. Mater.* **2015**, *27* (45), 7314–7319.

(8) Biswas, S.; Liu, X.; Jarrett, J. W.; Brown, D.; Pustovit, V.; Urbas, A.; Knappenberger, K. L.; Nealey, P. F.; Vaia, R. A. *Nano Lett.* **2015**, *15* (3), 1836–1842.

(9) Lin, Q.-Y.; Mason, J. A.; Li, Z.; Zhou, W.; O'Brien, M. N.; Brown, K. A.; Jones, M. R.; Butun, S.; Lee, B.; Dravid, V. P.; Aydin, K.; Mirkin, C. A. *Science* **2018**, *359* (6376), 669–672.

(10) Hung, A. M.; Micheel, C. M.; Bozano, L. D.; Osterbur, L. W.; Wallraff, G. M.; Cha, J. N. *Nat. Nanotechnol.* **2010**, *5* (2), 121–126.

(11) Flauraud, V.; Mastrangeli, M.; Bernasconi, G. D.; Butet, J.; Alexander, D. T. L. L.; Shahrabi, E.; Martin, O. J. F. F.; Brugger, J. *Nat. Nanotechnol.* **2017**, *12* (1), 73–80.

(12) Hughes, R. A.; Menumerov, E.; Neretina, S. *Nanotechnology* **2017**, *28* (28), 282002.

(13) Nordlander, P.; Oubre, C.; Prodan, E.; Li, K.; Stockman, M. I. *Nano Lett.* **2004**, *4* (5), 899–903.

(14) Deng, T.-S.; Parker, J.; Yifat, Y.; Shepherd, N.; Scherer, N. F. *J. Phys. Chem. C* **2018**, *122* (48), 27662–27672.

(15) Hao, E.; Schatz, G. C. *J. Chem. Phys.* **2004**, *120* (1), 357–366.

(16) Dadosh, T.; Sperling, J.; Bryant, G. W.; Breslow, R.; Shegai, T.; Dyshel, M.; Haran, G.; Bar-Joseph, I. *ACS Nano* **2009**, *3* (7), 1988–1994.

(17) Yin, H. J.; Liu, L.; Shi, C. A.; Zhang, X.; Lv, M. Y.; Zhao, Y. M.; Xu, H. J. *Appl. Phys. Lett.* **2015**, *107* (19), 193106.

(18) Mirin, N. A.; Bao, K.; Nordlander, P. *J. Phys. Chem. A* **2009**, *113* (16), 4028–4034.

(19) Yang, Z.-J.; Zhang, Z.-S.; Zhang, L.-H.; Li, Q.-Q.; Hao, Z.-H.; Wang, Q.-Q. *Opt. Lett.* **2011**, *36* (9), 1542–1544.

(20) Wu, D.; Jiang, S.; Liu, X. *J. Phys. Chem. C* **2012**, *116* (25), 13745–13748.

(21) Pakizeh, T.; Käll, M. *Nano Lett.* **2009**, *9* (6), 2343–2349.

(22) Brown, L. V.; Sobhani, H.; Lassiter, J. B.; Nordlander, P.; Halas, N. J. *ACS Nano* **2010**, *4* (2), 819–832.

(23) Onses, M. S.; Nealey, P. F. *Small* **2013**, *9* (24), 4168–4174.

(24) Zhang, X.; Servos, M. R.; Liu, J. *J. Am. Chem. Soc.* **2012**, *134* (17), 7266–7269.

(25) Hurst, S. J.; Lytton-Jean, A. K. R. R.; Mirkin, C. A. *Anal. Chem.* **2006**, *78* (24), 8313–8318.

(26) Palik, E. In *Handbook of Optical Constants of Solids*; Elsevier, **1997**.

(27) Konig, T. A. F.; Ledin, P. A.; Kerszulis, J.; Mahmoud, M. A.; El-Sayed, M. A.; Reynolds, J. R.; Tsukruk, V. V. *ACS Nano* **2014**, *8* (6), 6182–6192.

(28) Halperin, A.; Buhot, A.; Zhulina, E. B. *Langmuir* **2006**, *22* (26), 11290–11304.

(29) Romero, I.; Aizpurua, J.; Bryant, G. W.; Abajo, F. J. G. De. *Opt. Express* **2006**, *14* (21), 1627–1631.

(30) Timmermans, F. J.; Lenferink, A. T. M.; Van Wolferen, H. A. G. M.; Otto, C. *Analyst* **2016**, *141* (23), 6455–6462.

(31) Rechberger, W.; Hohenau, A.; Leitner, A.; Krenn, J. R.; Lamprecht, B.; Aussenegg, F. R. *Opt. Commun.* **2003**, *220* (1–3), 137–141.

(32) Su, K.-H.; Wei, Q.-H.; Zhang, X.; Mock, J. J.; Smith, D. R.; Schultz, S. *Nano Lett.* **2003**, *3* (8), 1087–1090.

(33) Samoc, A.; Miniewicz, A.; Samoc, M.; Grote, J. G. *J. Appl. Polym. Sci.* **2007**, *105* (1), 236–245.

(34) Welch, B. L. *Biometrika* **1947**, *34* (1–2), 28–35.

(35) Jain, P. K.; Huang, W.; El-Sayed, M. A. *Nano Lett.* **2007**, *7* (7), 2080–2088.

(36) Xie, H.; Lin, Y.; Mazo, M.; Chiappini, C.; Sánchez-Iglesias, A.; Liz-Marzán, L. M.; Stevens, M. M. *Nanoscale* **2014**, *6* (21), 12403–12407.

(37) Novara, C.; Chiadò, A.; Paccotti, N.; Catuogno, S.; Esposito, C. L.; Condorelli, G.; De Franciscis, V.; Geobaldo, F.; Rivolo, P.; Giorgis, F. *Faraday Discuss.* **2017**, *205*, 271–289.

(38) Itoh, T.; Kikkawa, Y.; Yoshida, K.; Hashimoto, K.; Biju, V.; Ishikawa, M.; Ozaki, Y. *J. Photochem. Photobiol. A Chem.* **2006**, *183* (3), 322–328.

(39) Zheng, Y.; Rosa, L.; Thai, T.; Ng, S. H.; Gómez, D. E.; Ohshima, H.; Bach, U. *J. Mater. Chem. A* **2015**, *3* (1), 240–249.

(40) Hofmann, A.; Schmiel, P.; Stein, B.; Graf, C. *Langmuir* **2011**, *27* (24), 15165–15175.

(41) Gandra, N.; Abbas, A.; Tian, L.; Singamaneni, S. *Nano Lett.* **2012**, *12* (5), 2645–2651.

(42) Weller, L.; Thacker, V. V.; Herrmann, L. O.; Hemmig, E. A.; Lombardi, A.; Keyser, U. F.; Baumberg, J. J. *ACS Photonics* **2016**, *3* (9), 1589–1595.

(43) Spackova, B.; Wrobel, P.; Bockova, M.; Homola, J. *Proc. IEEE* **2016**, *104* (12), 2380–2408.

(44) Wang, Y.; MacLachlan, E.; Nguyen, B. K.; Fu, G.; Peng, C.; Chen, J. I. L. *Analyst* **2015**, *140* (4), 1140–1148.

(45) Zhang, X.; Chen, Y. L.; Liu, R.-S.; Tsai, D. P. *Reports Prog. Phys.* **2013**, *76* (4), 046401.

(46) Robatjazi, H.; Bahauddin, S. M.; Doiron, C.; Thomann, I. *Nano Lett.* **2015**, *15* (9), 6155–6161.

(47) Furube, A.; Du, L.; Hara, K.; Katoh, R.; Tachiya, M. *J. Am. Chem. Soc.* **2007**, *129* (48), 14852–14853.

(48) Biswas, S.; Duan, J.; Park, K.; Pachter, R.; Vaia, R. A. *Nano Lett.* **2013**, *13*, 6287–6291.

Chapter 6: Directed Assembly of Nanodiamonds for Microscale-Resolution Thermal Mapping

* Modified with permission from Nano Letters ("Microscale-Resolution Thermal Mapping Using a Flexible Platform of Patterned Quantum Sensors", Andrich, P.;[§] Li, J.;[§] Liu, X.; Heremans, F. J.; Nealey, P. F.; Awschalom, D. D. *Nano Lett.* **2018**, *18* (8), 4684–4690).[1]

[§] These authors contributed equally.

6.1 Abstract

The continuing rapid miniaturization of semiconductor transistors and electronic devices has been tremendously contributing to the technological development. However, the high power density of highly compact devices can result in accumulation of heat, severely impacting the device performance, which calls for accurate sensors to monitor the heat distribution. To address this challenge, we develop a fabrication approach to construct arrays of nanodiamonds embedded in a flexible polymer matrix, which is ideal for temperature measurements on a wide range of systems. The nanodiamonds containing temperature-sensitive fluorescent spin defects are precisely placed on pre-patterned chemical patterns, followed by transfer printing to the polymer stamp, which can be applied on the target for thermal mapping. To demonstrate the thermal mapping potential of this platform, temperature profile of an operating coplanar waveguide has been reconstructed and compared with simulation result.

6.2 Introduction

The performance of semiconductor transistors is fundamentally limited to miniaturization, which has reached to an unprecedented scale in the last few decades. This has led to tremendous success of semiconductor technology, bringing us to the revolutionary digital age. One problem associated with the device miniaturization, however, is the local overheating, which can negatively impact the device performance and reliability. This has created the need for accurate sensors that could measure the hot spots at micro- or nano-scale level.

Current high-resolution temperature mapping techniques include fluorescent microthermography (FMT),[2] liquid crystal thermography (LCT),[3] scanning thermal microscopy (SThM)[4] and thermal reflectance microscopy (TRM).[5] Though these approaches represent considerable advances in the field, they still suffer from serious limitations. FMT and LCT require complicated sample preparations and need sensing coating, which can serve as additional heating source and cause imprecision in the measurements. SThM works relatively well for measurements over small areas, however it is not suitable for thermal mapping of larger areas due to the inherent limitation of scanning techniques. As the only contactless technique among these four approaches, TRM has its unique advantage. However, it requires extensive sample-by-sample calibration and the interpretation of data can be complex for textured samples.

To tackle these limitations, we propose a microscale thermal mapping platform based on arrays of nanodiamonds (NDs) embedded in a flexible polymer matrix. Each ND contains nitrogen-vacancy (NV) center, of which the spin level is sensitive to the change in local temperature. The spin levels of these defects can be optically detected, enabling temperature mapping via remote operation. The NDs first form well-ordered arrays on patterned silicon substrate,[6] followed by transferring to a transparent and flexible polymer stamp. The spatial

resolution of this sensor stamp is determined by the pattern pitch, and can readily reach micro- or even nano-scale. The polymer stamp with low thermal conductivity can be repeatedly used on a wide range of systems and only requires one-time calibration. The use of commercially available NDs also ensures reproducibility and enables large-area detection.

In this chapter, we demonstrate the details of the fabrication process and discuss the parameters that impact the sensor properties. The fabrication process is comprised of two main steps: (1) immobilization of NDs on chemical pattern, and (2) transfer printing to polydimethylsiloxane (PDMS). NDs can be selectively immobilized on the designated spots because the patterned areas have high affinity to the NDs, whereas the unpatterned areas have only minimal adhesion. It is worth noting that this technique can create not only ND patterns optimal for temperature mapping, but also arrays of isolated single NDs that can be interesting for other sensing and quantum applications.[7] These applications rely on the sensitivity of NV center to the magnetic and electric fields, and the implementation can be greatly simplified with single NV center. Finally, we demonstrate the thermal mapping capacity of this sensor by measuring the temperature distribution of a gold coplanar waveguide, which is then confirmed by simulation result.

6.3 Experimental

6.3.1 Materials

Silicon <100> wafers were purchased from WRS Materials, LLC. Cross-linkable polystyrene (PS) was synthesized as described previously[8] and contained 4% glycidyl methacrylate as a crosslinking agent. Hydroxyl-terminated poly(4-vinyl pyridine) (P4VP-OH) was purchased from Polymer Source, Inc. Poly(methyl methacrylate) (PMMA) photoresist (950 kg/mol, 4 wt % in chlorobenzene) was purchased from MicroChem, Inc. ND suspension

(NDNV100nm) was purchased from Adamas Nanotechnologies, Inc. Silicone elastomer kit (Sylgard 184) containing polydimethylsiloxane (PDMS) base and curing agent was purchased from Dow Corning Corp. 2-Propanol (IPA), 4-methyl-2-pentanone (MIBK), N,N-dimethylformamide (DMF), chlorobenzene and 1-methyl-2-pyrrolidinone (NMP) were purchased from Aldrich and used as received.

6.3.2 Fabrication of ordered nanodiamond arrays on PDMS

The ND arrays were first fabricated on a silicon substrate, and then transferred onto a thin PDMS membrane via a transfer printing approach.[7] To fabricate the ND arrays, the silicon substrate was first spin coated with 0.5 wt % cross-linkable PS in toluene and annealed at 190°C under vacuum for 24 h to drive the crosslinking reaction. PMMA photoresist was then spin-coated on top, followed by electron beam (E-beam) lithography to create desired patterns. After photoresist development with a mixture of MIBK/ IPA (1:3), the patterned surface was exposed to 20 W O_2 plasma for 30 s to remove the crosslinked PS (XPS) in the unprotected regions. The exposed silicon patterns were functionalized with P4VP-OH by spin coating from a 4 wt % solution in DMF and annealing at 210°C for 5 min in a nitrogen atmosphere. The remaining photoresist and excess P4VP-OH were then removed by sonication in NMP (3 min, 2 cycles) and chlorobenzene (3 min, 1 cycle). For adsorption of NDs onto patterns with P4VP, 100 μL ND suspension was spotted on the substrate, which was placed on an elevated post inside a sealed glass jar. The jar also contained 1 mL of water at the bottom to maintain a humid atmosphere and prevented the ND solution from evaporating. After 40 min adsorption, the substrate was rinsed thoroughly with water and dried with nitrogen.

In order to transfer ND arrays onto PDMS, PDMS base and curing agent were first mixed in 10:1 mass ratio. The mixture was degassed in a vacuum chamber before being poured on the

substrate surface with ND arrays. The substrate with mixture on top was then cured in a 60°C oven overnight. After the sample cooled down, the thin PDMS layer was peeled off from the silicon substrate and ready for further characterization.

6.4 Results and discussion

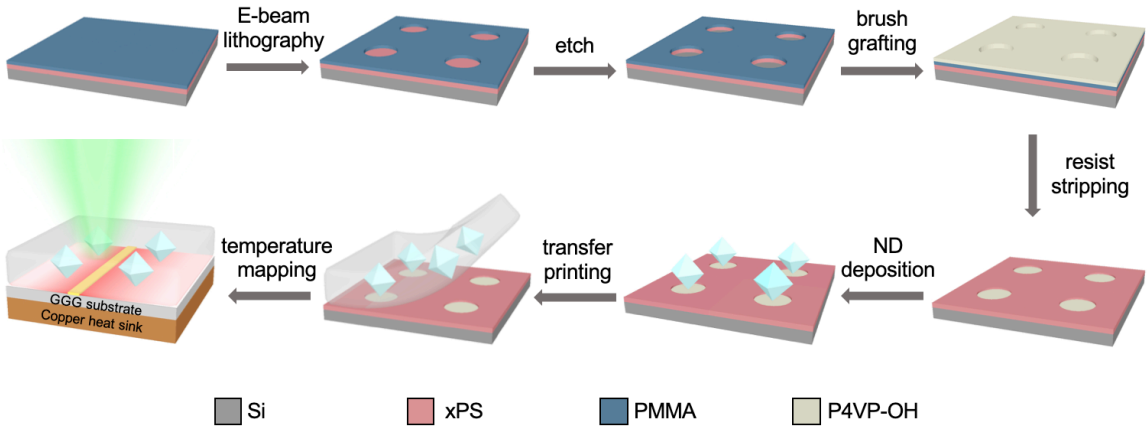

Figure 6.1 Fabrication process for the temperature sensing stamp. Substrate is coated with crosslinked PS mat and PMMA resist, followed by E-beam lithography and oxygen plasma etching to expose the patterned areas. The exposed areas are then functionalized with P4VP brush, which has a high affinity to the NDs, and the excess brush is removed by rinsing. NDs from drop-cast solution are selectively immobilized on the patterned spots, and can be transferred to a PDMS layer. The PDMS layer is placed on top of a GGG substrate with a microwave antenna patterned on top, which acts as a heat source. A confocal microscopy with a 532 nm laser excitation is used to address the NV centers in the diamond nanoparticles for the temperature measurement.

The detailed process for the fabrication of the temperature sensing stamp can be found in the Experimental section, and the scheme is shown in Figure 6.1. The NDs are selectively immobilized on P4VP brush due to electrostatic attraction—P4VP is slightly positively charged in water and carboxylic acid group on ND surface is negatively charged. We characterize the process by investigating the effect of pattern parameters on the ND arrays. We pattern square arrays of circular spots with different diameters and spacings, and study the resulting yield of ND coverage. SEM images reveal a direct relationship between number of NDs per spot and spot diameter (Figure 6.2a). For a more quantitative analysis, we analyze dozens of patterned spots for each size,

and discover a roughly linear dependence of particle number on the spot area (Figure 6.2b). Interestingly, we also find that over 80% patterned spots are occupied by single ND when pattern diameter is 100 nm, showing the potential to arrange solid-states qubits for sensing and quantum information applications using this technique.[9] We also note that pattern pitch, unlike pattern diameter, has hardly any impact on the particle coverage, implying the possibility of further increasing the spatial resolution of the sensor. For spot size larger than 100 nm diameter, this fabrication technique shows nearly 100% yield and excellent selectivity with controllable particle number, which can be comparable or advantageous to other recently developed methods.[10,11] Figure 6.2c also shows a greater variation in the number of NDs per spot as spot size increases, which can be attributed to the wide distribution of ND size (~50 to 300 nm). This variation can be potentially addressed by using a ND suspension with a narrower size distribution.

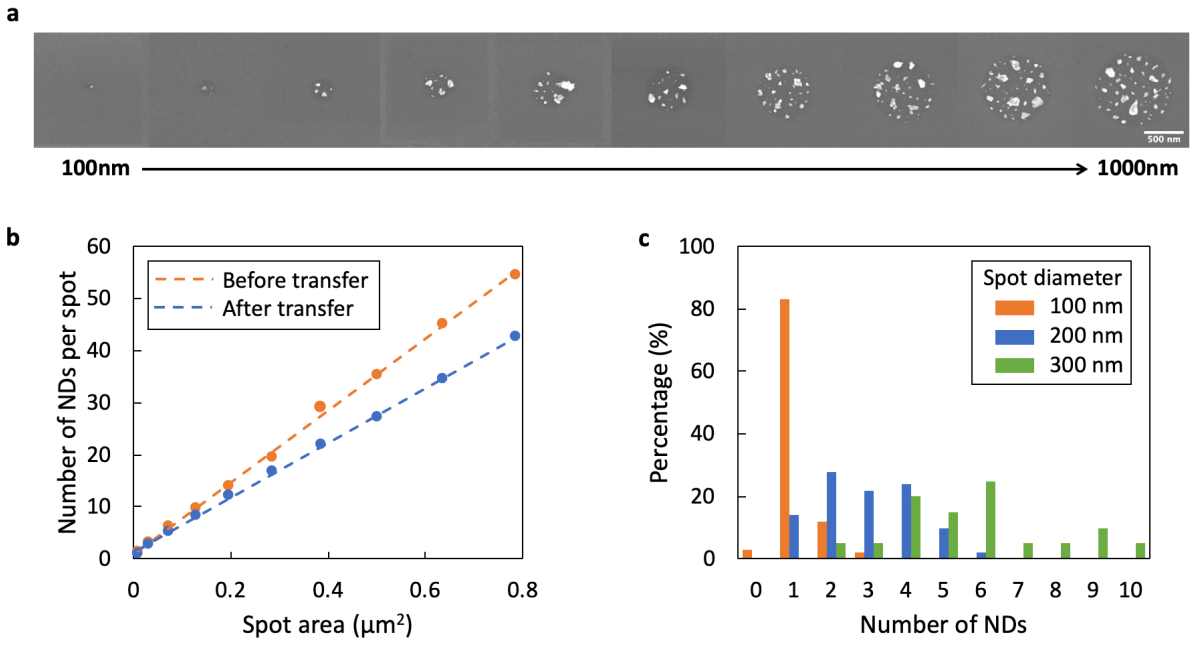

Figure 6.2 (a) SEM images show that the number of NDs increases with spot area. (b) Number of NDs per spot as a function of spot area. The dependence can be well fitted with a power law model. (c) Number of NDs per spot for patterned circles with 100, 200 and 300 nm diameter.

We then characterize the efficiency of transfering NDs to the PDMS stamp. Since it is challenging to directly image the NDs on PDMS, we take an indirect approach by calculating the difference of number of NDs on silicon substrate before and after the transfer printing step. The results are summarized in Figure 6.2b. It is obvious that the number of NDs transferred increases with the area of the patterned spots. We find that the number of NDs transferred y can be best fitted with a power law model $y = cA^{\alpha}$, where A is area of spots and c is a free fitting factor. The value of α is approximately 0.89 compared to 0.94 from the data collected before the transfer process, indicating that the efficiency of transfer moderately increases with spot size.

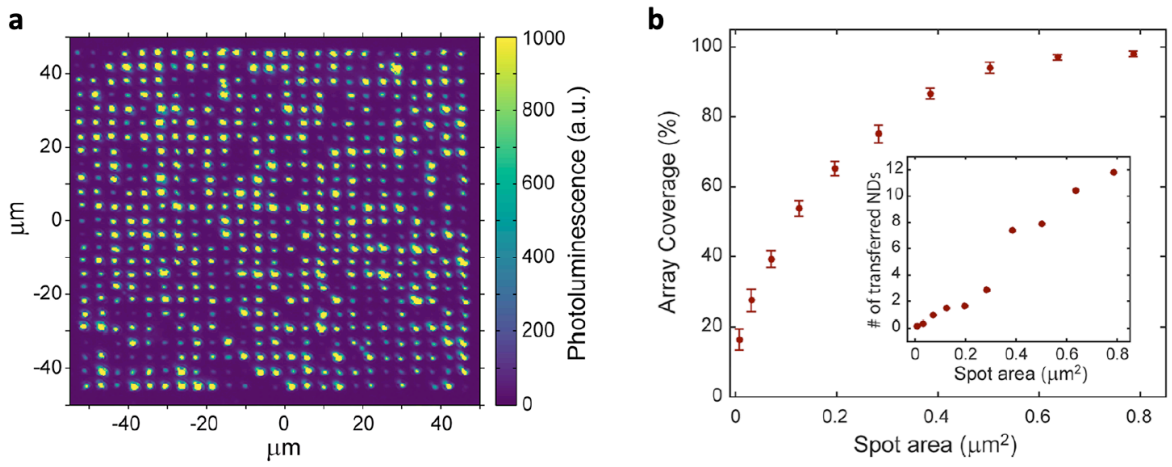

Figure 6.3 (a) PL scan image of arrays of NDs embedded in PDMS layer. The spot diameter is 1000 nm and spacing is 4 μm. (b) Percentage of the array sites with at least one ND with detectable PL signal as a function of the patterned spot area. The inset shows the expected number of NDs per spot on PDMS calculated from the data in Figure 6.2b.

We also characterize the transferred arrays on PDMS by collecting its two-dimensional photoluminescence (PL) map. The PDMS stamp is placed on a bare silicon wafer with NDs in contact with the silicon surface, and the PL signal is collected through the PDMS. Figure 6.3a shows a typical PL map of ND array with 1000 nm diameter and 4 μm spacing, and the signal shows wide variations among different spots. However, almost all spots are occupied by at least

one ND with detectable PL signal, and can be potentially used for temperature measurement. We further quantify the array coverage for each spot size, which increases with spot area and almost saturates at (98±0.8)% for the largest spot measured. It is also worth noting that, for the 0.2 μm^2 spots, ~65% spots are occupied by at least 1 ND and average number of NDs is less than 2, which can be valuable for applications that require the use of single ND. The temperature sensing, however, can take advantage of higher ND density and larger PL signal.

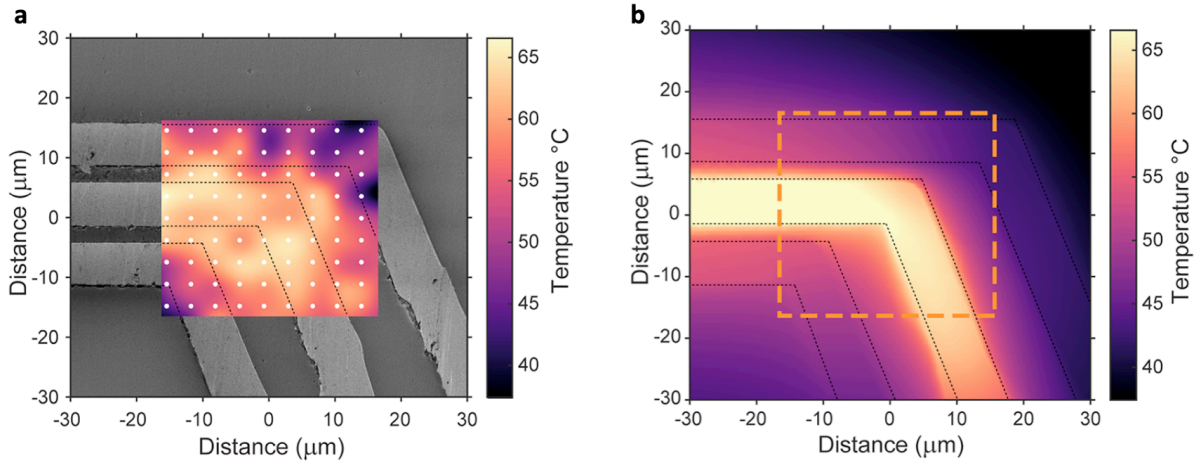

Figure 6.4 (a) Temperature map of a CPW obtained from the interpolated data collected on a 9 × 9 array of NDs (real positions indicated by the white dots). The thermal image is superimposed on the SEM image of the CPW to identify the sample's features. (b) Simulation of the CPW temperature map, showing qualitative agreement with the experimental data. The dashed box highlights the area that was investigated in the measurements shown in panel a.

Finally, we highlight the temperature sensing capability of the PDMS-ND stamp by measuring the temperature profile of a working coplanar waveguide (CPW) antenna. The CPW is patterned on a gadolinium gallium garnet (GGG) insulating substrate, and a 9 × 9 ND array is placed at the sharp bend of the antenna, which is expected to be greatly affected by the heating effect. To conduct the sensing measurement, we use a modified continuous-wave optically detected magnetic resonance (ODMR) technique. The microwave input is alternated between a

100 μs, 0.4 W pulse off-resonant with respect to the NV centers' spin transitions (2.6 GHz) and a weaker 5 μs, 1 mW pulse of varying frequency. The former is used to stimulate the heating in the circuit, whereas the latter probes the NV centers' zero-field resonance as in a conventional ODMR experiment.[12] The PL signal is collected in the presence of the microwave probing pulse, and a 500 ns time buffer separates the heating and the probing stages of the measurements to eliminate any potential spurious frequency components from the strong heating pulse during the photon collection time bin. For each frequency of the microwave probing signal, we repeat the measuring sequence until we average the signal for 475 ms, and the resulting ODMR traces are compared with calibration measurements collected with the heating pulse turned off. In particular, the shift in the zero-field splitting parameter D is calculated for each particle by subtracting the values obtained from a Lorentzian fit of the ODMR spectra collected with and without the heating pulse.[13]

We then estimate the values for the absolute temperature using $\frac{dD(T)}{dT} = 100$ kHz/K,[13] and the results are plotted in Figure 6.4a superimposed on an SEM image of the mapped CPW. The discrete temperature values obtained from the 81 spots are linearly interpolated to create a continuous thermal map. We also confirm that the microwave signal used to probe the NV centers does not introduce spurious heating effects. No detectable shift of the ODMR resonances is observed when the probe power is raised by 4 times.

To better understand the results, we develop a model in COMSOL Multiphysics to construct a simulated temperature map (Figure 6.4b). Comparing Figure 6.4a and 6.4b, we see that the experimentally obtained temperature map qualitatively agrees with the simulation results. In particular, the sensor is able to detect the higher temperature at the position of the CPW, and the shift toward lower temperature with the increasing distance. We also accurately image the presence of a hotter region where the CPW bends, which is associated with a higher current density at the

inside edge of the metal. The wider variation in the experimental data is likely associated with the spatially discrete nature of the measurement and imperfections in the CPW's geometry. Using the 95% confidence interval of the resonance position obtained from the ODMR data, we estimate the uncertainty of temperature measurement is 3.9±2.9 K across the array. This uncertainty, however, depends on the specific properties of NDs used in this work.

Though we collect the full ODMR spectra in this demonstration experiment and each sweep is composed of 71 frequency data, it is possible to perform the measurement at a fixed microwave probing frequency once a calibration of the array is done, which can greatly reduce the acquisition time and improve the accuracy. The calibration would require the measurement of D as a function of a known temperature for all NDs, and only needs to be done once prior to all the measurements. Furthermore, the spatial resolution of this measurement can be readily improved with reduced pattern pitch and spot size, and can potentially reach diffraction-limit resolution to be integrated into super-resolution microscopy. The temperature accuracy, on the other hand, can be enhanced with more advanced dynamical decoupling techniques performed on the NV centers' spin.[14,15]

6.5 Conclusions

In conclusion, we combine chemical pattern technique and transfer printing process to fabricate arrays of NDs embedded in a transparent and flexible PDMS stamp. We are able to control the number of NDs per site by varying the patterning parameters. In particular, we vary from array of single NDs to maximum coverage with up to 10 NDs per spot, which can be ideal for different applications. We showcase the temperature sensing potential by measuring the temperature map of an operating CPW at the micrometer scale, which has been confirmed by the simulation results. When combined with a widefield imaging apparatus that allows for the

simultaneous investigation of large number of NDs, these systems could allow for fast and sensitive mapping of large areas while maintaining microscale resolution. We believe that the approach introduced in this work represents an important step toward the implementation of defect-based quantum sensing in a wide range of applications.

6.6 References

(1) Andrich, P.; Li, J.; Liu, X.; Heremans, F. J.; Nealey, P. F.; Awschalom, D. D. *Nano Lett.* **2018**, *18* (8), 4684–4690.

(2) Herzum, C.; Boit, C.; Kölzer, J.; Otto, J.; Weiland, R. *Microelectronics J.* **1998**, *29* (4–5), 163–170.

(3) Liu, W.; Yang, B. *Sens. Rev.* **2007**, *27* (4), 298–309.

(4) Cahill, D. G.; Goodson, K.; Majumdar, A. *J. Heat Transfer* **2002**, *124* (2), 223–241.

(5) Ryu, S. Y.; Kim, D. U.; Kim, J. K.; Choi, H. Y.; Kim, G. H.; Chang, K. S. *Int. J. Thermophys.* **2015**, *36* (5–6), 1217–1225.

(6) Liu, X.; Biswas, S.; Jarrett, J. W.; Poutrina, E.; Urbas, A.; Knappenberger, K. L.; Vaia, R. A.; Nealey, P. F. *Adv. Mater.* **2015**, *27* (45), 7314–7319.

(7) Andrich, P.; de las Casas, C. F.; Liu, X.; Bretscher, H. L.; Berman, J. R.; Heremans, F. J.; Nealey, P. F.; Awschalom, D. D. *npj Quantum Inf.* **2017**, *3* (1), 28.

(8) Han, E.; Stuen, K. O.; La, Y. H.; Nealey, P. F.; Gopalan, P. *Macromolecules* **2008**, *41* (23), 9090–9097.

(9) Schietinger, S.; Barth, M.; Aichele, T.; Benson, O. *Nano Lett.* **2009**, *9* (4), 1694–1698.

(10) Heffernan, A. H.; Greentree, A. D.; Gibson, B. C. *Sci. Rep.* **2017**, *7* (1), 9252.

(11) Kianinia, M.; Shimoni, O.; Bendavid, A.; Schell, A. W.; Randolph, S. J.; Toth, M.; Aharonovich, I.; Lobo, C. J. *Nanoscale* **2016**, *8* (42), 18032–18037.

(12) Schirhagl, R.; Chang, K.; Loretz, M.; Degen, C. L. *Annu. Rev. Phys. Chem.* **2014**, *65* (1), 83–105.

(13) Toyli, D. M.; Christle, D. J.; Alkauskas, A.; Buckley, B. B.; Van de Walle, C. G.; Awschalom, D. D. *Phys. Rev. X* **2012**, *2* (3), 031001.

(14) Toyli, D. M.; de las Casas, C. F.; Christle, D. J.; Dobrovitski, V. V.; Awschalom, D. D. *Proc. Natl. Acad. Sci.* **2013**, *110* (21), 8417–8421.

(15) Neumann, P.; Jakobi, I.; Dolde, F.; Burk, C.; Reuter, R.; Waldherr, G.; Honert, J.; Wolf, T.; Brunner, A.; Shim, J. H.; Suter, D.; Sumiya, H.; Isoya, J.; Wrachtrup, J. *Nano Lett.* **2013**, *13* (6), 2738–2742.

Chapter 7: Conclusions

The theme of this thesis is to demonstrate the usefulness of controlling the assembly of nanomaterials using chemical patterns, which can realize a wide range of applications otherwise impossible. As the techniques of material synthesis and nanofabrication continue to progress, combining top-down and bottom-up approaches becomes an inevitable trend to achieve more complex structures and advanced applications. Directing the assembly of solution-processed materials using lithographically defined chemical patterns, as shown in this work, is a representative example of this trend.

Chapter 2-4 focuses on DSA of BCPs, which is one of the most interesting and widely studied applications of the chemical pattern technique. Self-assembling BCPs can be guided by the chemical patterns and form registered periodic structures which are useful for lithography applications. The critical dimension of the DSA pattern can easily reach sub-10 nm without any additional pitch shrinking steps, making it promising candidate for the next-generation nanolithography technology. Defectivity remains the main concern of implementing DSA for high volume manufacturing, and our study suggests that it is possible to eliminate all of the defects with optimized annealing and etching conditions. The distribution of defect size and configuration is determined by the chemical pattern, which may need further optimization to minimize the energy barrier along the free energy pathway during annealing.

We further extend the utilization of chemical pattern in other materials systems, such as nanoparticle and nanodiamond, as demonstrated in Chapter 5 and 6. Interparticle spacing and addressability on surface are both critical to exploiting the optical properties of nanoparticles for nanophotonic applications. Conventional approaches generally focus on either one of these two

but hardly realize both. By developing a hierarchical assembly approach combining chemical pattern technique and DNA-directed assembly, we have achieved sub-5m gap size with full addressability on substrate, which can be extended to more complex structures. Similarly, we control the assembly of nanodiamonds using chemical pattern and transfer the patterned arrays to PDMS as a temperature sensing stamp.

Note that the chemical pattern technique is not limited to the materials and applications we have shown above. The key of this technique is to utilizing the chemical contrast between the patterned and unpatterned areas, which has the potential to be applied to practically any material systems. The patterned areas can be functionalized with various chemicals and biomolecules, and benefit any applications that can take advantage of the full addressability on substrate. It would be of great interest to bring the chemical pattern technique into the interdisciplinary fields of chemistry, biology and physics.